# Bose-Einstein Correlations in $e^+e^-$ Events

This thesis was typset with $\LaTeX 2_\varepsilon$.
Cover page: “Matter meets antimatter”, copyright DESY, Hamburg.

# Bose-Einstein Correlations in $e^+e^-$ Events

Een wetenschappelijke proeve op het gebied
van de Natuurwetenschappen, Wiskunde en Informatica.

Proefschrift

ter verkrijging van de graad van doctor
aan de Katholieke Universiteit Nijmegen,
volgens besluit van het College van Decanen
in het openbaar te verdedigen
op woensdag 9 januari 2002,
des namiddags om 3.30 uur precies,

door

Jorn Antoine van Dalen

geboren op 14 mei 1974 te Herwen en Aerdt.

Promotor: Prof. Dr. E.W. Kittel

Co-promotor: Dr. W.J. Metzger

Manuscriptcommissie: Prof. Dr. E.A. De Wolf (University of Antwerpen)
Prof. Dr. K.J.F. Gaemers (University of Amsterdam)
Prof. Dr. T. Csörgő (KFKI, Budapest)
Dr. P. de Jong (NIKHEF, Amsterdam)
Dr. Š. Todorova-Nová (FzU, Prague)

Het werk beschreven in dit proefschrift maakt deel uit van het onderzoeksprogramma van de Stichting voor Fundamenteel Onderzoek der Materie (FOM), die financieel wordt ondersteund door de Nederlandse Organisatie voor Wetenschappelijk Onderzoek (NWO).
The author was financially supported by the “Stichting voor Fundamenteel Onderzoek der Materie (FOM)”, which is part of the “Nederlandse Organisatie voor Wetenschappelijk Onderzoek (NWO)”.

ISBN 90-9015348-9

# Contents

# Introduction

The idea that matter consists of some simple and constant elementary units is deeply ingrained in our way of thinking. We observe that matter appears in an enormous variety of different realizations, qualities, and shapes, transforming from one into another. In these changes, however, we observe many recurring properties: features that remain unchanged, or, if changed, that recur under similar conditions. We suppose that there must be something permanent in nature that causes these repeating phenomena. This is the origin of the idea of elementary particles, as Newton already expressed it so clearly [1]:

> *All these things being considered, it seems probable to me that God in the beginning formed matter in solid, massy, hard, impenetrable, moveable particles, of such sizes and figures, and with other properties, and in such proportion to space, as most conduced to the end for which He formed them; and that these primitive particles are incomparably harder than any porous bodies compounded of them; even so very hard, as never to wear or break in pieces.*

So, it was already Newton who put forward an assumption concerning "elementary" particles: they must have well-defined, specific, invariable properties. In his time, this quality could only result from being "incomparably" hard. Such elementary units were eventually discovered when chemists during the 18th and 19th centuries found that all matter is made of 92 different species of atoms.

Previous generations of high energy particle physics research have revealed the structure of the atom with its nucleus and orbiting electrons. Penetrating still deeper into this structure, nowadays, research focuses on the composition of the individual particles inside the nucleus, studying their properties and the ways in which they interact. Decades of painstaking experiments and theoretical insights have finally led to a theory, *the Standard Model*, that describes all of the known elementary particle interactions (except gravity).

This theory states that all matter is composed of fermionic quarks and leptons interacting via bosonic field quanta. All species are structureless point particles at the current level of experimental resolution. The strong, weak, and electromagnetic interactions among the quarks and leptons are described by renormalizable gauge (quantum field) theories. Quarks bind in sets of two (mesons) and three (baryons) to form nuclear constituents (protons and neutrons) and other hadrons. Leptons include the electron, and other charged (muon, tau) and neutral (neutrino) particles.

The strong interaction is responsible for the stability of protons, neutrons and the atomic nucleus, but also for the creation of further quark-antiquark pairs, and is mediated by the massless gluon. The theory describing strong interactions is known as quantum chromodynamics (QCD). The electromagnetic interaction, which is mediated by the massless photon, is responsible for the stability of electronic orbitals in atoms, and the inter-atomic and inter-molecular behaviour, and thus quantum electrodynamics (QED) governs the properties of chemical reactions and bulk material. The weak interaction causes radioactive decay of nuclear constituents and unstable leptons, and is mediated by the massive W and Z bosons. The theory describing the electromagnetic and weak interactions is sometimes called the GWS-theory, because it is cast into its present form by Glashow, Weinberg and Salam. There is no established quantum field model of the gravitational interaction, but gravitation is thought to be responsible for the large-scale structure of the universe. The gravitational interaction is postulated to be mediated by the (yet unobserved) graviton.

When the relative energy of a quark-antiquark pair is large, further pairs are produced in the gluon force field building up between them. Quarks and antiquarks do not exist as free particles in nature, but recombine into a large variety of particles most of which are bosons (e.g., pions, kaons, $\rho$'s, $\omega$'s), measured in the detectors of high-energy experiments.

The role of Bose-Einstein correlations (BEC) in all this is purely a consequence of the basics of quantum mechanics: symmetrization of the multiparticle wave function of a system consisting of identical bosons, affects the measured $n$-particle coincidence spectra and leads to an enhancement relative to the corresponding product of independent one-particle spectra, if the emitted particles are close in phase space (i.e., they occupy the same elementary phase-space cell). The interest of BEC is threefold.

Firstly, the spatial length of the elementary phase-space cells is limited by the geometric size of the source of particles with the considered momentum. The larger this size, the narrower these cells are in momentum space. By varying the relative momenta and watching the onset of BEC effects, one can thus measure the spatial length of the elementary phase-space cells and thereby the size and shape of the source.

Secondly, BEC may have an influence on the measurement of resonance masses, in particular of the W mass at LEP2. The measurement of the W boson mass is a key issue of LEP2. In W-pair production where both W's decay hadronically, a large systematic error is attributed to the poor understanding of BEC, particularly between bosons coming from decays of different W's in the same event. Existence of these inter-W BEC would induce a non-independent fragmentation of the two W's.

Thirdly, higher-order correlations ($> 2$) are sensitive to details of various dynamical correlations and therefore may serve to distinguish between models for multi-boson production. They also play an important role in the phenomenon of intermittency.

The outline of this work is as follows. In the first chapter a theoretical background on BEC, relevant to this thesis, is given. The second chapter is devoted to the experimental setup. The following three chapters deal with the analyses related to measurements of the geometrical size of the boson source, to the (non-)existence of BEC between bosons coming from different W's in fully hadronic WW decay, and to third-order BEC, respectively. At the end of this thesis a summary of conclusions is given.

Note that in this thesis we will use the *Heaviside-Lorentz* units and set $c = \hbar = 1$.

# Chapter 1

# Theory

In this chapter, a theoretical background, relevant to this work, on Bose-Einstein correlations (BEC) is given. Firstly, a short historical overview is given, then the quantum mechanical basics are explored and several deficiencies in these are shown. In this work, the interest in BEC has three origins and each of these will be considered in some detail. In the last section of this chapter an overview will be given on the building blocks of event generators based on a Monte Carlo technique, and in particular the simulation of BEC in these generators.

## 1.1 History

Interference of identical particles emitted incoherently occurs when the product of their relative momentum and (initial) distance is less than $\hbar$, i.e., they do not interfere when

$$\Delta p \cdot \Delta x \gtrsim 2\pi \quad , \tag{1.1}$$

a condition similar to Heisenberg's uncertainty relation.

Essentially, the interference can be observed from intensity correlations that appear due to Bose-Einstein or Fermi-Dirac symmetrization of the two-particle final-states of identical bosons or fermions, respectively.

The first experiments dealing with BEC as intensity correlations, were done by Hanbury Brown and Twiss [2] and were performed in 1957 at the Narrabri observatory, Australia. Intensities from two telescopes on a circular railroad of diameter $\sim$ 100 m were correlated at equal times and the correlation function was reconstructed for nearby stars. The correlation function varies with distance $d$ between the telescopes as $\sim \cos(2\pi d\theta/\lambda)$, where $\lambda$ is the wavelength of the light and $\theta$ is the angular separation between the two points of emission on the star. For a star of diameter $D$ at a distance $L$ from our solar system $\theta = D/L$. The distance between the telescopes where correlations take place is then $d \sim \frac{\lambda}{\theta} = \frac{L\lambda}{D}$. E.g., for Sirius ($D \simeq 1.8 D_\odot$ and $L \simeq 8.7$ light-years) one finds $d \simeq 20$ m.

This principle of measuring BEC, or intensity correlations, was first applied in high-energy collisions in 1959 by G. and S. Goldhaber, Lee and Pais [3,4]. In proton anti-proton collisions at 1.05 GeV, observations of angular distributions of pions showed a deviation from the predictions of a "classical" statistical model, but could be described satisfactorily by applying Bose-Einstein (BE) statistics.

Although BEC are a well-known phenomenon since decades, there is still a lot of research on this subject, today. The reason for this is mainly that the BEC carry an enormous amount of information on the geometry and dynamics of the production region of bosons (see sections 1.2 and 1.3).

## 1.2 Basic Principle

The usual derivation of the BE effect begins with the observation of an interference between two identical bosons, e.g., pions. This can be explained if one assumes that the amplitude for observing these two identical bosons, produced at space-time points $x_1$ and $x_2$ with four-momenta $p_1$ and $p_2$, in detectors A and B located at $x_\mathrm{A}$ and $x_\mathrm{B}$, respectively (see fig. 1.1), is given by the plane wave superposition

$$\begin{aligned} |p_1 p_2\rangle &= \frac{1}{\sqrt{2}}\left[\mathrm{e}^{ip_1(x_1-x_\mathrm{A})+i\phi_1}\mathrm{e}^{ip_2(x_2-x_\mathrm{B})+i\phi_2} + \mathrm{e}^{ip_1(x_2-x_\mathrm{A})+i\phi_1}\mathrm{e}^{ip_2(x_1-x_\mathrm{B})+i\phi_2}\right] \\ &= \frac{1}{\sqrt{2}}\mathrm{e}^{-i(p_1x_\mathrm{A}+p_2x_\mathrm{B}-\phi_1-\phi_2)}\left[\mathrm{e}^{ip_1x_1}\mathrm{e}^{ip_2x_2} + \mathrm{e}^{ip_1x_2}\mathrm{e}^{ip_2x_1}\right] \quad , \end{aligned} \tag{1.2}$$

where $\phi_1$ and $\phi_2$ are the phases of the pions. The second term between brackets arises from the symmetrization required by BE statistics. The reason for this symmetrization is that the observer cannot say from which point in space-time ($x_1$ or $x_2$) the boson originates, so that he has to take into account both possibilities. Squaring this amplitude gives the following two-pion intensity correlation function

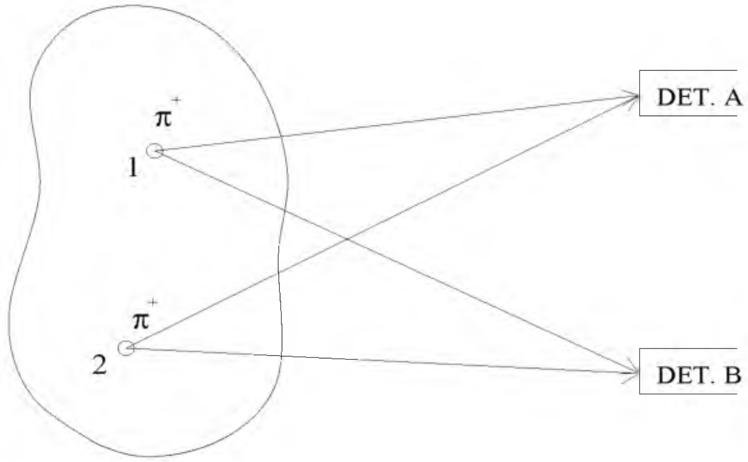

Figure 1.1: Principle of symmetrization of the wave function for two identical pions.

$$R_2(p_1, p_2) = 1 + \cos(Q \cdot \Delta x) \quad , \tag{1.3}$$

where $Q \equiv Q^\mu$ is the vector of the four-momentum difference of the two pions, and $\Delta x$ is the (initial) space-time difference between the two pions. Note that the correlation function is independent of the position of the detectors A and B, and of the phases $\phi_1$ and $\phi_2$. Eqn. (1.3) measures the production of two identical pions, relative to what an uncorrelated production would have led to.

The second step is to go from the binary source to the assumption that the boson source points $x_1$ and $x_2$ are randomly distributed in a region of space-time specified by a normalized density distribution $f(x)$, with no energy-momentum dependence. Then, the two-particle intensity correlation function of observing two identical pions with four-momenta $p_1$ and $p_2$ becomes

$$R_2(p_1,p_2) = \int \mathrm{d}^4x_1\mathrm{d}^4x_2 f(x_1)f(x_2)\left|\left|p_1p_2\right\rangle\right|^2 \simeq 1+|G(Q)|^2 \quad , \tag{1.4}$$

where $G(Q)$ is the Fourier transform of $f(x)$,

$$G(Q) = \int \mathrm{d}x \exp(iQ\cdot x)f(x) \quad , \tag{1.5}$$

which tends to unity when the invariant four-momentum difference, $Q$, goes to zero. In terms of the invariant mass of the two-pion system, $M_{12}$, and the pion mass, $m_\pi$, $Q = \sqrt{M_{12}^2 - 4m_\pi^2}$.

The second term on the right hand side of eqn. (1.4) (a correlation term) is the consequence of the BE interference, or intensity interference, between the two parts of the amplitude in eqn. (1.2). From eqn. (1.4) we, therefore, expect $R_2 - 1$ to measure the absolute square of the Fourier transform of the space-time distribution of the boson source. The energy scales on which we might expect BEC in $\mathrm{e}^+\mathrm{e}^-$ collisions can directly be estimated from Heisenberg's uncertainty principle: typical pion sources in these collisions are of size $\sim 1$ fm, see, e.g., [5–7], so that interference occurs predominantly when $Q \lesssim 1\ \mathrm{fm}^{-1} \simeq 500$ MeV.

Having reviewed the usual derivation of the BE effect, it is important to note its shortcomings. Fortunately, theoretical improvements have been made on several shortcomings.

Firstly, the assumption of a static pion source has been made. A more realistic picture can be obtained when incorporating also the time dependence of the pion source, which is done in [8]. There, the two-pion correlation function is derived using the first quantized Klein-Gordon equation in the presence of several source currents. Assuming that pions are produced on the surface of a sphere with radius $R$, whose time extension is exponentially cut off with a characteristic time $\tau$, one obtains

$$R_2(q_\mathrm{T}, q_0) = 1 + \frac{I^2(q_\mathrm{T}R)}{1+(q_0\tau)^2} \quad , \tag{1.6}$$

where $q_\mathrm{T}$ is the projection of the three-momentum difference onto the plane perpendicular to the sum of the two three-momenta, $q_0$ is the pion energy difference and $I(x) \equiv 2J_1(x)/x$, where $J_1(x)$ is the first Bessel function, so that $I(0) = 1$ and $I(\infty) = 0$. In the limit of

$q_{\mathrm{T}} = q_0 = 0$, we get $R_2 = 2$, in agreement with the result of eqn. (1.4) in the limit of $Q = 0$.

Secondly, in this simple derivation, $R_2$ only depends on the momentum difference between the two pions. In general, $R_2$ is defined in a six-dimensional momentum space: three components coming from the momentum difference between the two pions and three components coming from their momentum sum. Indeed, the general Wigner formalism [9] allows for a dependence on the momentum sum, $K \equiv \frac{1}{2}(p_1+p_2)$, as well. In this formalism, the theoretical approximation of $R_2$ reads [9–12]

$$R_2(Q, K) \simeq 1 + \frac{\left|\int \mathrm{d}^4x\, S(x, K) \exp(iQ \cdot x)\right|^2}{\left|\int \mathrm{d}^4x\, S(x, K)\right|^2} \quad , \tag{1.7}$$

where the emission function $S(x, K)$, which is related to the single-particle number density, is the probability of emission of a boson from space-time point $x$ with momentum $K$. In this thesis, the $K$ dependence is not studied since the statistics for the analyses turn out too poor to do this.

Thirdly, the assumption is made that a particle can be associated with a plane wave, i.e., a particle is assumed to be free and can be described by a wave travelling in the same direction as the particle, with a fixed wave number. However, interaction of particles with the Coulomb and strong interactions is present. In [10, 13] the correlation function is calculated, including the effects of final-state Coulomb and strong interactions.

A fourth criticism is that these derivations do not properly address the multiparticle nature of the final hadronic state. Only two-particle pion wave functions are considered, although in general, a coherent superposition of multipion wave functions (and hence, a non-trivial multiplicity distribution) must describe the final hadronic state. Techniques have been developed to calculate multi-particle BE interference to all orders, see, e.g., [14–17], for incoherent and coherent production mechanisms.

Fifthly, the specific dynamical assumption is made that pions are produced independently at random space-time points. Such a derivation, therefore, cannot reveal the effects of possible coherent pion production dynamics: removing a particle from a coherent state does not change the structure of the final-state and thus the BE effect is absent. Indeed, there are models for hadron production in quark fragmentation, such as the bremsstrahlung model [18] or the Schwinger model [19] that predict such a coherence. Completely incoherent identical boson production means $R_2 \rightarrow 2$ for $Q \rightarrow 0$, whereas $R_2 = 1$ for coherent production. Since, in experiments one often measures a maximum effect smaller than $R_2 = 2$, a correlation strength $\lambda$ [20] is introduced in front of the term which measures the BEC. A deviation of the measured intercept parameter $R_2(0) - 1$ from unity can be due to particles from (long-lived) resonances which contribute at very low $Q_{ij}$, $\mathcal{O}(10)$ MeV [21], not resolvable by the detector, and/or a (partially) coherent particle emitting source.

Sixthly, in actual applications, things are still not general enough, even for incoherent pion production: conservation laws like energy-momentum and quantum number conservation are a source of correlations. Energy-momentum conservation leads to kinematic constraints between the produced particles and leads to strong correlations when one boson is observed with a momentum near the kinematic boundary. There are some theoretical results that characterize the effects of energy-momentum conservation, see, e.g., [22], where the interplay between the multi-pion BE symmetrization and the degree of coherence of the production mechanism is studied and discussed by introducing energy constraints effects. Conservation of internal symmetries and quantum numbers such as isospin and parity lead to correlations between the number of differently charged pions that can be produced in a given reaction.

Next to all these theoretical difficulties, there are also some purely experimental obstacles in measuring BEC, such as misidentification of the particles, track losses, two-particle resolution and momentum resolution.

## 1.3 Fields of Interest

In this thesis, there are three motivations to analyse BEC.

- To determine the space-time development of a boson production region.
- The influence of BEC on the measurement of the W mass at LEP2.
- Higher-order correlation effects and their consequences.

Each of these three fields of interest will be explored in some detail. But firstly, it is necessary to describe the Bose-Einstein correlation function in terms of densities. Basic relations of the density formalism to study correlations are summarized in appendix A.

In general, correlations between two particles with four-momenta $p_1$ and $p_2$ are described by

$$R'_2(p_1,p_2) \equiv \frac{\rho_2(p_1,p_2)}{\rho_1(p_1)\rho_1(p_2)} \quad , \tag{1.8}$$

where $\rho_2$ is the two-particle number density and $\rho_1$ the single-particle number density in phase space.

In a sample of identical particles, let the symbol $y$ represent the kinematic variables needed to specify the position of each particle in this space. Then, the single-particle density is defined as

$$\rho_1(y) \equiv \frac{1}{N_{\mathrm{ev}}}\frac{\mathrm{d}n}{\mathrm{d}y} \quad , \tag{1.9}$$

where $N_{\mathrm{ev}}$ is the total number of events used and $n$ is the number of identical particles. In this way $\rho_1$ is normalized as

$$\int_y \rho_1(y)\,\mathrm{d}y = \langle n\rangle \quad , \tag{1.10}$$

with $\langle n\rangle$ being the average number of these particles per event.

In defining the two-particle density we need to realize that we only consider identical particles with a given mass. Therefore, as already mentioned above, the correlation function is defined in six-dimensional momentum space. However, since BEC are largest at small four-momentum difference $Q$, $\rho_2$ is usually parametrized in terms of this single variable:

$$\rho_2(Q) \equiv \frac{1}{N_{\mathrm{ev}}} \frac{\mathrm{d}n_{\mathrm{pairs}}}{\mathrm{d}Q} \quad , \tag{1.11}$$

where $n_{\mathrm{pairs}}$ is the number of pairs of identical particles. In this way $\rho_2$ is normalized as

$$\int_Q \rho_2(Q)\mathrm{d}Q = \langle n(n-1) \rangle \quad . \tag{1.12}$$

Since we consider two possible combinations of identical particles, positive-positive and negative-negative, both samples are combined. Consequently, the normalization would be a factor 2 larger. However, experimentally we avoid double counting by taking each pair only once, giving an additional factor 1/2, which cancels the factor 2.

Since we are only interested in BEC, the product of the two single-particle number densities in eqn. (1.8) is replaced by $\rho_{0,2}(Q)$, the two-particle density that would occur in the absence of BE interference, resulting in the BE correlation function

$$R_2(Q) \equiv \frac{\rho_2(Q)}{\rho_{0,2}(Q)} \quad . \tag{1.13}$$

Note that $\rho_{0,2}$ is defined and normalized in the same way as $\rho_2$. The reference sample leading to $\rho_{0,2}$ is difficult to construct since it does not occur in nature.

### 1.3.1 BEC Measuring a Space-Time Picture

According to eqn. (1.4), BEC reveal the space-time structure of the pion production region by means of a Fourier transformation of $R_2 - 1$. In this thesis, we will investigate the space-time structure of the pion production region in $\mathrm{e^+e^-} \rightarrow \mathrm{Z} \rightarrow \mathrm{q\bar{q}}$ events. Since we observe BEC only at small values of $Q$, we only consider a certain region of phase space and thus only a certain region of the source in space-time. Therefore, we will from now on speak about the *region of homogeneity*, i.e., the range over which BE interference takes place.

However, there is no reason to expect the region of homogeneity to be spherically symmetric, and therefore in this work we will split the four-momentum difference $Q$ into three components. Two of these components measure the longitudinal (approximately parallel to the $\mathrm{q\bar{q}}$ system) and transverse (approximately perpendicular to the $\mathrm{q\bar{q}}$ system) geometrical size of the region of homogeneity. The third component measures a mixture between the emission time of the pions and the transverse geometrical region of homogeneity. The system that is used to study BEC in three dimensions does not allow us to separate the third component into a time-like and space-like part. The importance of studying BEC in more than one dimension, or rather studying the region of homogeneity in more than one dimension, is twofold. Not only can it give a measure of deviations from a spherically symmetric source, at present the basis of the implementation of BEC in Monte Carlo models (i.e., models using random numbers from probability distributions to generate events), but it can also give us information on the amount of overlap in space-time of two hadronic systems, in particular the hadronic systems when two W's produced together in $e^+e^-$ collisions decay into hadrons. Apart from the quark flavour composition, we expect hadronic Z decay at LEP1 ($\sqrt{s} \simeq 91.2\,\text{GeV}$) to be similar to hadronic W-decay at LEP2 ($\sqrt{s} \sim 200\,\text{GeV}$). When two W's are produced and both decay hadronically, the amount of overlap of the two hadron production regions in space-time depends on the structure of the production region. E.g., for two elongated regions there will be, in general, less overlap than for two spherical regions. The amount of overlap in space-time of these two production regions may influence the amount of BEC between bosons coming from different W's, since particles produced close to each other in space-time are more likely to have a small $Q$ value than particles that are far apart in space-time. There may be a significant overlap since the experimentally observed region of homogeneity is of order 1 fm, about an order of magnitude larger than the distance between the $W^+W^-$ decay vertices at LEP2 energies. So, the BEC of identical pions originating from different W's could be large [23].

### 1.3.2 BEC in WW events

Here, we arrive at the second point of interest of studying BEC. Recent theoretical models are still contradictory when it comes to the existence of BEC between bosons originating from different W's in the process $e^+e^- \to W^+W^- \to$ hadrons and to what extent it influences the measurement of the W mass in this channel [23, 25–31]. If these inter-W BEC exist, this naturally influences the measurement of the W mass. Existence of these correlations means that the observer cannot say from which W a boson is coming. An enhanced production of (soft) pions is measured with respect to a world without BEC, which influences the measured momentum of the W, and thus its measured mass. Since the determination of the mass of the W is a key issue at LEP2, and since BEC are responsible for a large part of its systematic error, the importance of studying the (non-)existence of BEC between particles from different W's is obvious.

To better understand the role of BEC in WW events, let us for the moment assume that there is no stochastic dependence between the W's. Let us further assume that the single-particle number density for fully hadronic WW events (i.e., where both W's decay hadronically) is two times the single-particle density for the hadronically decaying W in semi-hadronic WW events (i.e., where one W decays hadronically and the other W decays into a lepton and a neutrino), for full overlap in the variable(s) used. I.e., the spectrum of a single-particle variable (e.g., momentum, rapidity, azimuthal angle, polar angle) is the same for the hadronically decaying part of semi-hadronic WW events as for fully hadronic WW events. Translated to the two-particle density $\rho_{0,2}$, this means that $4\rho_{0,2}^{\mathrm{W}} = \rho_{0,2}^{\mathrm{WW}}$, where the superscript WW indicates that both W's decay hadronically and the superscript W indicates that only one W decays hadronically. Note that we assume $W^+$ and $W^-$ decays to be similar here. Defining the cumulant correlation function $C \equiv \rho_2 - \rho_{0,2}$, one can write the BE correlation function for the fully hadronic WW events as [24]

$$R_2^{\mathrm{WW}}(p_1,p_2) = 1 + \frac{1}{2}\frac{C^{\mathrm{W}}(p_1,p_2)}{\rho_{0,2}^{\mathrm{W}}(p_1,p_2)} \quad , \tag{1.14}$$

where $C^{\mathrm{W}}(p_1,p_2)$ is the cumulant correlation function for semi-hadronic WW events. From this, one concludes that the strength of the BEC in fully hadronic WW events must be in the range 0.5-1 times that of the BEC in semi-hadronic WW events, with the lower value corresponding to complete absence of BEC between particles of different W's and complete overlap in the variable(s) used.

Since in practice one encounters problems at small relative momenta: shrinking phase space and low statistics, momentum and two-track resolution, uncertainties due to Coulomb repulsion and the effect of long-lived resonances, it is hard to measure the strength of the BEC, i.e., $\lambda$, and thus difficult to draw conclusions on the (non-)existence of inter-W BEC, here.

Therefore, the following method [24] is used to study BEC between particles from different W's, directly. If the two W's decay independently, the two-particle density in fully hadronic WW events, $\rho_2^{\mathrm{WW}}$, is given by

$$\rho_2^{\mathrm{WW}}(p_1,p_2) = \rho_2^{\mathrm{W}^+}(p_1,p_2) + \rho_2^{\mathrm{W}^-}(p_1,p_2) + \rho_1^{\mathrm{W}^+}(p_1)\rho_1^{\mathrm{W}^-}(p_2) + \rho_1^{\mathrm{W}^-}(p_1)\rho_1^{\mathrm{W}^+}(p_2) \quad , \tag{1.15}$$

where we use the superscripts WW to indicate that both W's decay hadronically and $\mathrm{W}^{\pm}$ to indicate that only the $\mathrm{W}^{\pm}$ decays hadronically. A derivation of eqn. (1.15) is given in appendix A. Assuming that the densities for $\mathrm{W}^+$ and $\mathrm{W}^-$ are the same, eqn. (1.15) becomes

$$\rho_2^{\mathrm{WW}}(p_1,p_2) = 2\rho_2^{\mathrm{W}}(p_1,p_2) + 2\rho_1^{\mathrm{W}}(p_1)\rho_1^{\mathrm{W}}(p_2) \quad . \tag{1.16}$$

The terms $\rho_2^{\mathrm{WW}}$ and $\rho_2^{\mathrm{W}}$ of eqn. (1.16) are measured in the fully hadronic WW and semi-hadronic WW events, respectively. To measure the product of the single-particle densities we use the two-particle density $\rho_{\mathrm{mix}}^{\mathrm{WW}}(p_1,p_2)$, obtained by pairing particles originating from two *different* semi-hadronic WW events, to ensure that particles from different W's are not correlated. Since we measure all the terms in eqn. (1.16) we can test the hypothesis that the two W's decay independently and thus study the (non-)existence of inter-W correlations.

### 1.3.3 Three-Particle BEC

So far in this thesis, the only correlations that are considered are of order two. However, a lot of information, not present in two-particle correlations, can be derived from higher-order correlations. Furthermore, higher-order correlations constitute an important theoretical issue for the understanding of BEC [32]. In this work, we will analyse three-particle correlations. Experimentally, it becomes difficult to study even higher-order correlations, since the sensitivity to small $Q$ values increases considerably with the order of the correlations.

Three-particle correlations are sensitive to asymmetries in the particle source shape which cannot be studied by two-particle correlations. E.g., when pions are produced via resonances, or when sources are moving, an asymmetry in $f(x)$, or rather in $S(x,K)$, is introduced [33]. The definition of asymmetry is here that $f(x) \neq f(-x)$ or $S(x,K) \neq S(-x,K)$, when the centre of the source is at $x=0$.

More importantly, by combining two- and three- particle correlation analyses, one gets a better handle on the degree of coherence. From two-particle correlations alone this is very difficult due to resonances which disturb the correlation function, and also due to the poor resolution of the detector to measure particles with almost the same momenta. Furthermore, higher-order correlations are of crucial importance for much of the search for scaling phenomena in multiparticle processes [34]. Studies of (higher-order) correlations at high energies are thus related to the composition of jets and tests of QCD models.

In this thesis, we will study the three-particle BE correlation function $R_3$. Analogously to eqn. (1.8), $R_3'$ is defined in nine-dimensional momentum space as (see also appendix A)

$$R_3'(p_1,p_2,p_3) \equiv \frac{\rho_3(p_1,p_2,p_3)}{\rho_1(p_1)\rho_1(p_2)\rho_1(p_3)} \quad , \tag{1.17}$$

where $\rho_3(p_1,p_2,p_3)$ is the three-particle number density, which can be described in terms of single-particle, two-particle and genuine three-particle densities as (see also appendix A)

$$\rho_3(p_1,p_2,p_3) = \rho_1(p_1)\rho_1(p_2)\rho_1(p_3) + \sum_{(3)} \left[\rho_1(p_1)\left(\rho_2(p_2,p_3) - \rho_1(p_2)\rho_1(p_3)\right)\right] + C_3(p_1,p_2,p_3) \quad , \tag{1.18}$$

where the sum is over the three possible permutations and where $C_3$ is the third-order cumulant measuring the genuine three-particle correlations, i.e., without the contribution coming from two-particle interference. The $\rho_1\rho_2$ terms contain all the two-particle correlations. Since we are only interested in BEC, we replace $\rho_1(p_1)\rho_1(p_2)\rho_1(p_3)$ by $\rho_{0,3}(p_1,p_2,p_3)$, the three-particle density that would occur in a world without BEC. Thus, analogously to the two-particle BE correlation function, eqn. (1.13), the three-particle BE correlation function is defined as

$$R_3(p_1,p_2,p_3) \equiv \frac{\rho_3(p_1,p_2,p_3)}{\rho_{0,3}(p_1,p_2,p_3)} \quad . \tag{1.19}$$

The kinematical variable normally used in three-particle correlations studies is $Q_3 \equiv \sqrt{Q_{12}^2+Q_{13}^2+Q_{23}^2}$ with $Q_{ij} \equiv \sqrt{-(p_i-p_j)^2}$. For a three-pion system, $Q_3 = \sqrt{M_{123}^2 - 9m_\pi^2}$, with $M_{123}$ the invariant mass of the pion triplet and $m_\pi$ the mass of the pion. In this case $\rho_3$ is defined and normalized as

$$\rho_3(Q_3) \equiv \frac{1}{N_{\text{ev}}}\frac{\mathrm{d}n_{\text{triplets}}}{\mathrm{d}Q_3} \quad , \tag{1.20}$$

$$\int_{Q_3} \rho_3(Q_3)\mathrm{d}Q_3 = \langle n(n-1)(n-2)\rangle \quad , \tag{1.21}$$

analogously to eqns. (1.11) and (1.12) for the two-particle density, with $n_{\text{triplets}}$ being the number of triplets consisting of identical particles. Experimentally, the normalization is a factor 3 smaller: to avoid double counting of triplets we need to divide by a factor 6 and since we combine positive particles as well as negative particles to form triplets, we need to multiply by a factor 2.

In particular, using eqn. (1.4), and assuming totally incoherent production of particles with a source density $f(x)$, we are able to write the three-particle BE correlation function as [35]

$$R_3(Q_{12}, Q_{13}, Q_{23}) = 1 + |G(Q_{12})|^2 + |G(Q_{13})|^2 + |G(Q_{23})|^2 + 2\mathrm{Re}\{G(Q_{12})G(Q_{13})G(Q_{23})\} \quad , \tag{1.22}$$

so that the genuine three-particle BE correlation function reads

$$R_3^{\mathrm{genuine}}(Q_{12}, Q_{13}, Q_{23}) = 1 + 2\mathrm{Re}\{G(Q_{12})G(Q_{13})G(Q_{23})\} \quad . \tag{1.23}$$

In general, the production of particles is not completely incoherent and/or $f(x)$ not symmetric, and therefore the Fourier transform $G(Q_{ij})$ is complex, $G \rightarrow G\exp(i\phi_{ij})$. The phase factor, $\exp(i\phi_{ij})$, cancels in the two-particle BE correlation function, see eqn. (1.4), but survives in the three-particle BE correlation function as seen from eqn. (1.22). In fact, from eqn. (1.23), using $\phi \equiv \phi_{12} + \phi_{13} + \phi_{23}$, we find

$$\cos\phi = \frac{R_3^{\mathrm{genuine}}(Q_{12}, Q_{13}, Q_{23}) - 1}{2\sqrt{(R_2(Q_{12}) - 1)(R_2(Q_{13}) - 1)(R_2(Q_{23}) - 1)}} \quad , \tag{1.24}$$

which is a function of $Q_{ij}$. In particular, due to the normalization, $\cos\phi \rightarrow 1$ when all $Q_{ij} \rightarrow 0$.

The phase factor $\cos\phi$ differs from unity, either because the source is asymmetric or because the emission is (partially) coherent. However, asymmetry in the production mechanism will only result in a small (a few percent) reduction of $\cos\phi$ [33,36], and this only in the case where the asymmetry occurs around the point of highest emissivity. It is important to note, that eqn. (1.22) is *not* valid for partially coherent sources, in which case more complicated expressions are needed [36]. We can always define $\cos\phi$ by eqn. (1.24), but $\cos\phi$ has a defined meaning as a phase factor only for incoherent sources. If $\cos\phi$ differs from one, we can infer that partial coherence is present but $\cos\phi$ does not measure directly the fraction of pions produced incoherently.

In the special case where $f(x)$ is Gaussian, and to the extent that phase factors may be neglected, i.e., assuming completely incoherent production of pions and a symmetric source density function, or $\cos\phi = 1$, $R_3^{\mathrm{genuine}}$ is related to $R_2$ via

$$R_3^{\mathrm{genuine}}(Q_3^2) - 1 = 2\sqrt{R_2(Q_3^2) - 1} \quad , \tag{1.25}$$

depending only on $Q_3^2$. A deviation from this equation reveals new information not present in two-particle BE correlations, namely information related to the (in)coherence and/or (a)symmetry of the source.

## 1.4 Monte Carlo Simulation

In this section, an overview is given of the main building blocks of Monte Carlo (MC) generators and the present available algorithms to simulate BE effects in MC models.

### 1.4.1 Monte Carlo Generators of $e^+e^-$ Collisions

Quantum mechanics states that all processes in nature have a random character. Using functions known from experiment or theory which describe physical processes (such as differential cross sections, fragmentation functions, branching ratios and decay rates), the MC generator, at each step, produces a random outcome from a set of possible outcomes. The MC generation of the process $e^+e^- \rightarrow \gamma/Z \rightarrow q\bar{q} \rightarrow$ hadrons can be divided into four stages:

- The electroweak stage.
  In this stage, the process $e^+e^- \rightarrow \gamma/Z$ is described and the subsequent creation of the quark-antiquark pair takes place. The flavour the quarks in the final-state of each event is picked at random, according to the relative couplings.

- The perturbative QCD stage.
  This stage is responsible for the final-state radiation of quarks and gluons. In general, these high-order QCD corrections are modelled in two different ways: fixed-order QCD models or QCD shower (or parton shower) models [37]. The first models consider the processes $\gamma/Z \rightarrow q\bar{q}$, $q\bar{q}g$ (first order in the coupling constant $\alpha_s$), $q\bar{q}gg$ and $q\bar{q}q\bar{q}$ (second order in $\alpha_s$) and use complete QCD matrix elements. The QCD shower models repeatedly apply the basic splitting processes $q \rightarrow qg$, $g \rightarrow gg$ and $g \rightarrow q\bar{q}$ using differential probabilities derived from leading-log and next-to-leading-log approximations (LLA and NLLA). In the LLA only the leading collinear and soft logarithm terms are taken into account in the calculations. The NLLA also takes the next-to-leading-logarithm term into account.

- The hadronic stage.
  In practice, for the description of the transition of quarks into hadrons only phenomenological models are available. Often, the Lund string hadronization scheme [38, 39] is used. Colour strings are stretched between the colour charges of the different partons. When the strings break, they create quark and antiquarks at the endpoints which subsequently combine to form colour singlet hadron states. As an alternative model, the so-called cluster model [40] is used, where all gluons resulting from the perturbative phase are split into $q\bar{q}$ pairs. Subsequently, colourless clusters of $q\bar{q}$ pairs are formed which then decay into hadrons respecting simple phase space and spin conservation rules. On average, this model leads to a less satisfactory agreement with the experimental data than the Lund string model.

- The decay phase of unstable hadrons.
  Also for this stage, no reliable models are available. Therefore, as an input, measurements of the decay properties of the particles are used.

### 1.4.2 Bose-Einstein Algorithms

Presently, BEC are implemented in MC models either via "local" or "global" methods.

In the *local* method [31], the momenta of pairs of particles are shuffled is such a way that the $Q$ distribution is raised by either a Gaussian factor $1+\lambda\exp(-R^2Q^2)$, or an exponential factor $1+\lambda\exp(-RQ)$. This simulation is done in the event generator JETSET [37] by the subroutine LUBOEI and the model is called $\mathrm{BE}_0$. The disadvantage of this model is that it has no quantum mechanical basis, but is an ad hoc way to simulate BE effects. Consequences are that energy-momentum conservation is violated and the assumption is made that nature deals with a spherically symmetric Gaussian or exponential region of homogeneity. The problem of energy-momentum conservation is partially solved by making additional shifts involving other pairs of particles. Several algorithms have been developed to perform this additional shifting in a more refined way than that of the original $\mathrm{BE}_0$ model: $\mathrm{BE}_3$, $\mathrm{BE}_{32}$, $\mathrm{BE}_m$, $\mathrm{BE}_m^L$ and $\mathrm{BE}_\lambda$ [31]. All these models have been tuned to the L3 Z decay data and the $\mathrm{BE}_3$ and $\mathrm{BE}_{32}$ models, which only slightly differ in the extra shifting procedure, give a good description of the data in a variety of variables [41]. In this thesis, results will usually be compared with the $\mathrm{BE}_0$ and $\mathrm{BE}_{32}$ models. The $\mathrm{BE}_0$ algorithm uses the tuned values PARJ(92)=1.5 and PARJ(93)=0.33 GeV and the $\mathrm{BE}_{32}$ algorithm uses the tuned values PARJ(92)=1.68 and PARJ(93)=0.38 GeV.

In the *global* method [27,29,42], particle four-momenta are not changed, but events are given a weight. This weight is the ratio between how often a specific event would take place if there would be BEC and how often it would take place if there were no BEC. In the global method, energy and momentum are conserved, but biases may be introduced, since the weights may fluctuate wildly from event to event, destroying the convergence of the MC method and changing event-shape distributions. Attempts have been made to avoid these biases, e.g., see [27]. No successful tuning has been performed yet on the presently available global methods. So, the global methods will not be used in this thesis.

# Chapter 2

# Experimental Details

In this chapter, a short description is given of the Large Electron Positron collider (LEP) at CERN and of the L3 detector, which collected the data used for the analyses in this thesis.

## 2.1 LEP

The circular LEP collider is located at the French-Swiss border near Geneva and was operational from August 1989 till November 2000. The LEP tunnel, with a circumference of 26.7 kilometres, houses the accelerator and lies some 50 to 150 metres below ground level. It consists of eight curved sections of 2840 metres length each and eight straight sections, see fig. 2.1. LEP accelerates electrons and their anti-particles, positrons, in opposite directions in a vacuum pipe inside a retaining ring of magnets, before inducing them to collide head-on. Normally, electron and positron beams are stored in the LEP ring for several hours at fixed energies. LEP has four intersection regions, each of which is surrounded by a particle detector to measure the properties of the secondary particles coming from the collision. Each of the detectors, ALEPH, OPAL, DELPHI and L3, has been optimized differently to study various physics aspects.

The electrons and positrons that are injected into LEP, have first been pre-accelerated. The injection system of LEP consists of the following interconnected accelerators:

- LIL: The LEP Injector Linacs create the electrons and positrons in pulses of 12 ns and accelerate them to 600 MeV. The first linac accelerates electrons to 200 MeV and shoots them onto a tungsten target (the converter), such that positrons are generated. These positrons are accelerated up to 600 MeV by the second linac. The electrons for LEP are produced by a gun located near the converter.

- EPA: The Electron Positron Accumulator accumulates the electrons and positrons from the LIL into bunches.

- PS: The Proton Synchrotron accelerates the bunches of electrons and positrons to 3.5 GeV.

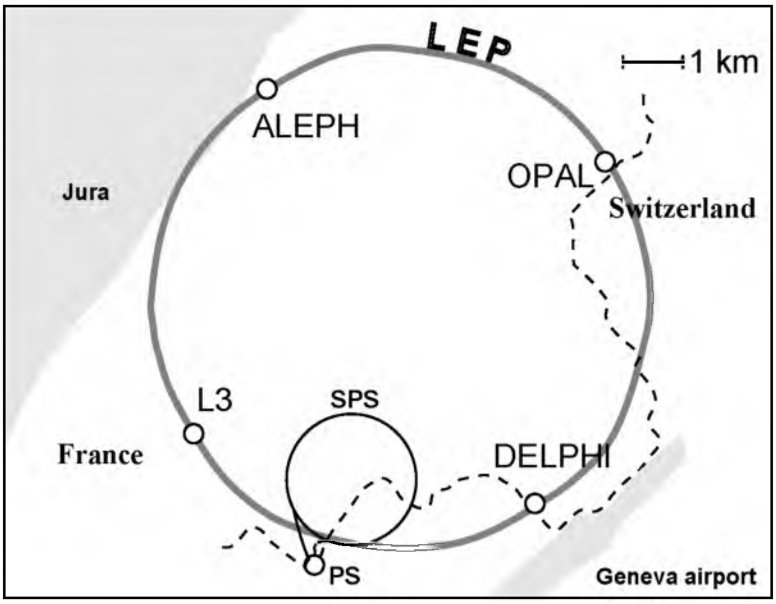

Figure 2.1: The LEP ring under the surface of the French-Swiss border near Geneva. The four experiments ALEPH, OPAL, DELPHI and L3, as well as the PS and SPS rings are indicated.

- SPS: The Super Proton Synchrotron with a circumference of 7 kilometres accelerates the bunches to 20 GeV and injects them into LEP.

After filling LEP, the particles are accelerated to the final beam energy by Radio Frequency (RF) cavities (five-cell copper cavities in the first years of LEP running, superconducting cavities after 1995), which are driven by klystrons with a total power of 16 MW. The RF system also replaces the energy lost by the beam because of synchrotron radiation, which is proportional to the fourth power of the energy, and focuses the particles longitudinally into discrete bunches. The beams are kept in orbit by more than 3000 bending magnets and almost 2000 focusing and correcting magnets.

The LEP collider's initial energy was chosen to be around a centre-of-mass energy of $\sqrt{s} \simeq 91\,\mathrm{GeV}$, so that in these collisions a Z boson would be produced, and the properties of the Z could be studied in detail. Since the end of 1995, LEP has moved on from the Z and entered its second phase (LEP2). Its energy has been doubled to allow the study of the production of ZZ pairs and of $\mathrm{W}^+\mathrm{W}^-$ pairs, the charged counterparts of the Z. Thus a new domain has been opened to test the Standard Model and to search for new particles, particularly the Higgs boson and supersymmetric particles. Table 2.1 shows an overview of the centre-of-mass energy at which LEP operated each year, and the corresponding luminosity integrated over time typically collected per experiment. The luminosity, $\mathcal{L}$, is defined as the collision rate at the interaction point divided by the interaction cross section. It is typically of the order of $10^{31}$ $\mathrm{cm}^{-2}\mathrm{s}^{-1}$ and depends on several LEP parameters such as the beam energy, the current and the size of the beams at the interaction point. The integrated luminosity is usually expressed in units of $\mathrm{pb}^{-1}$ (inverse picobarn), which is equal to $10^{36}$ $\mathrm{cm}^{-2}$. It is determined using small-angle Bhabha scattering ($\mathrm{e}^+\mathrm{e}^- \to \mathrm{e}^+\mathrm{e}^-$) via the definition

$$\int \mathcal{L}\mathrm{d}t = \frac{N_{\mathrm{Bhabha}}}{\sigma_{\mathrm{Bhabha}}} \quad . \tag{2.1}$$

Here, $N_{\mathrm{Bhabha}}$ is the collected number of small-angle Bhabha events in a period of time, and $\sigma_{\mathrm{Bhabha}}$ the accepted Bhabha cross section. Since the latter is theoretically well known for small scattering angles, the integrated luminosity can be determined with high precision.

More about the LEP machine can be found in [43].

Table 2.1: Centre-of-mass energy at which LEP operated each year, and the corresponding integrated luminosity typically collected by each experiment.

| year | $\sqrt{s}$, GeV | $\int \mathcal{L}$, $\mathrm{pb}^{-1}$ |
|---|---|---|
| 1989-1995 | 89-93 | 155 |
| 1995 | 130-136 | 5 |
| 1996 | 161-172 | 20 |
| 1997 | 183 | 55 |
| | 130-136 | 7 |
| 1998 | 189 | 176 |
| 1999 | 192-202 | 230 |
| 2000 | 200-209 | 215 |

## 2.2 The L3 Experiment

This section gives insight into the setup of the detector from which the data are extracted, and in particular the central tracker which is the most important part of the detector for this work.

### 2.2.1 The Setup

The L3 experiment [44] at LEP is based on a large magnetic detector optimized for the precision measurement of photons, electrons, muons, and hadron jets. A perspective view is shown in fig. 2.2. The various subdetectors, as well as the directions of the positron and electron beams are indicated.

The coordinate system we will use from now on is the following: the right-handed L3 Cartesian coordinate system has its origin at the interaction point. The positive $z$-axis is defined as the direction of flight of the electron beam; the positive $x$-axis points to the centre of the LEP ring and the positive $y$-axis points upward. Furthermore, $r$ is defined as the distance from the interaction point, and $\vec{s}$ as the projection of the $\vec{r}$ vector onto the $x-y$ plane. The polar angle $\theta \in [0, \pi]$ is the angle with respect to the positive $z$-axis and the azimuthal angle $\phi \in [0, 2\pi]$ is the angle in the $x-y$ plane with respect to the positive $x$-axis.

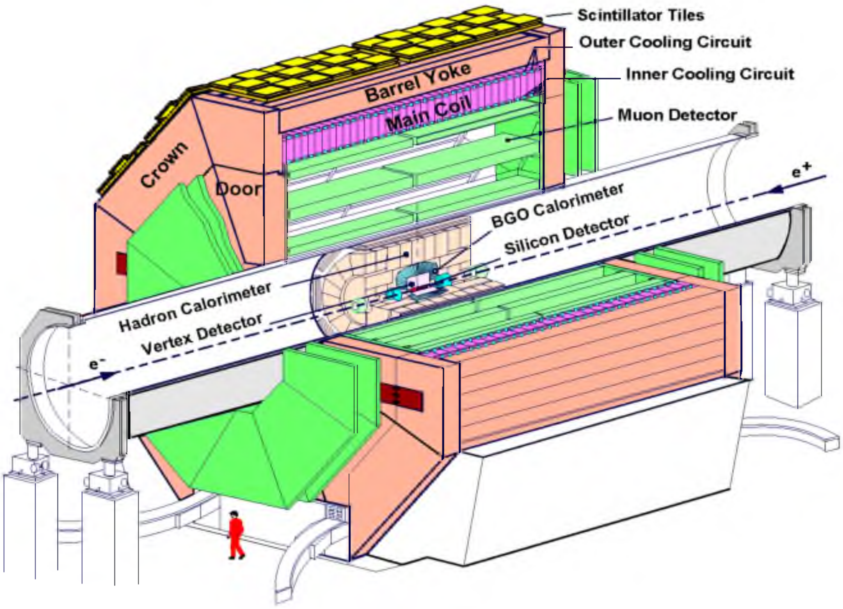

Figure 2.2: Perspective view of the L3 detector.

The particles that are produced at the interaction point and their possible decay products successively may encounter the following subdetectors, while traversing the detector.

- A silicon microvertex detector (SMD) to measure accurately the position of charged tracks immediately outside the beam pipe.

- A central tracking detector, specifically a time expansion wire chamber (TEC) to measure the curvature and direction of charged tracks. On the outside of the TEC the Z-chamber is situated for the main measurement of the $z$-coordinate.

- An electromagnetic calorimeter (ECAL), made of Bismuth Germanate Oxide (BGO) crystals, to measure photon and electron energies and directions.

- Scintillation counters to supply trigger information and distinguish particles originating from an $e^+e^-$ interaction from particles which find their origin outside the detector, e.g., particles from cosmic rays.

- A hadron calorimeter (HCAL), consisting of alternating layers of proportional wire chambers and slabs of depleted uranium, to measure hadron energies.

- Muon chambers (MUCH) to measure high momentum muons.

- Scintillator tiles which are used to trigger particles originating from cosmic rays, in dedicated cosmic ray studies. These tiles are not used in LEP physics runs.

All of these subdetectors (except the TEC, the SMD and the scintillator tiles) consist of a barrel part and a forward and backward part (the endcaps). In addition, there is a very small angle tagger (VSAT) to detect scattered beam particles in two-photon collisions. Furthermore, there are active lead rings (ALR), situated near the beam pipe at $z = \pm 1.04$ m, to protect the TEC from beam backgrounds, and a luminosity monitor at $z = \pm 2.65$ m to monitor and measure the luminosity. All subdetectors used for LEP physics, except the MUCH, are supported by a 32 m long steel tube of 4.45 m diameter and mounted (together with MUCH) inside a solenoid coil producing a magnetic field of 0.5 T along the beam axis.

### 2.2.2 Tracking of Particles

Since the analyses in this thesis mainly make use of charged particles, the tracking of these particles will be described in some detail now. For a description of other parts of the detector and even more details on the central tracker, I refer to [45] where the L3 detector is extensively described.

The trajectory of a charged particle moving from the interaction point outwards can be detected in the SMD, the TEC and the Z-chamber. An $xy$-view of a slice of these three subdetectors is given in fig. 2.3. The main purpose of the central tracker is to detect charged particles and to measure their location, direction and transverse momentum, as

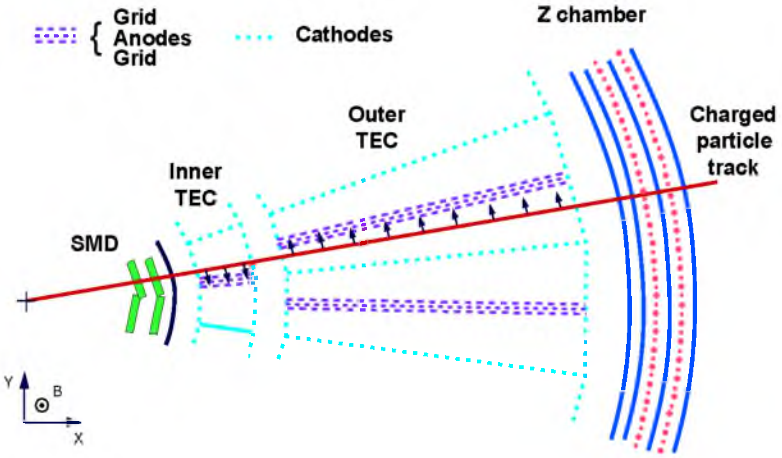

Figure 2.3: $xy$-view of a slice of the central tracker of L3.

well as the sign of their charge. From this information, the position of the interaction point and of secondary decay vertices of particles with lifetime greater than some $10^{-13}$ s can be reconstructed.

The main component of the central tracker is the TEC, which consists of two concentric high precision drift chambers mounted around the beam line: the inner TEC, radially extending from 8.5 cm to 14.3 cm, and the outer TEC, radially extending to 46.9 cm. The inner TEC is subdivided into 12 sectors, each with a 30° coverage in $\phi$ and containing 8 anode wires running parallel to the $z$-axis. The outer TEC is divided into 24 sectors, each with a 15° coverage and containing 54 anode wires, resulting in 62 wires in total. This configuration is chosen to achieve the largest possible ratio of drift volume over detection volume, a factor which maximizes the spatial precision. The gas mixture in the TEC is 80% $CO_2$ and 20% isobutane. The 62 wires are kept at high voltage, so that the positively ionized gas atoms and the electrons resulting from a charged particle passing this gas mixture, drift to the cathode and anode wires, respectively. The electrons cause a cascade of secondary electrons which gives a detectable signal (a "hit"). The geometry of the TEC is such that only a track with $44° < \theta < 136°$ can reach all 62 wires, while a track with $\theta < 10°$ or $\theta > 170°$ misses the TEC completely.

The main $z$-measurement is provided by the Z-chamber, situated on the outside of the TEC and consisting of two cylindrical proportional wire chambers with cathode strip readout. The Z-chamber covers $45° < \theta < 135°$. In 1991, Forward Tracking Chambers (FTCs) were installed behind the TEC end flange. These two layers of cylindrical multi-wire drift chambers measure the position and direction of tracks in the forward direction: $12° < \theta < 34°$ and $146° < \theta < 168°$.

The SMD installed in 1993, gives two additional high-precision space points. The SMD is made of 300 $\mu$m thin silicon wafers with microstrips of doped silicon on both the top and bottom surfaces. Electron-hole pairs created in the wafer by a traversing charged particle are collected on these strips. The strips on the top and bottom surfaces are orthogonal: one side measures the coordinate in the $r-\phi$ plane and the other the coordinate in the $r-z$ plane. The SMD consists of two rings each made of 12 ladders, see fig. 2.4, at radial distances of 6 and 8 cm from the interaction point, respectively. Each layer consists of 12 ladders in $\phi$ and each ladder of four wafers.

An important step in the inner tracking system reconstruction is an extensive calibration of the SMD and the TEC. For these calibrations, pairs of $e^+e^-$ or $\mu^+\mu^-$ tracks produced in $e^+e^-$ collisions without hard photon radiation are used. These tracks are sharply peaked back-to-back and assumed to form a single trajectory. The concept of the internal SMD alignment is to find a prediction for the intersection point of a track with a wafer and to compare this prediction with the measured hit position. Therefore, the trajectory of two electrons or two muons is approximated by one straight line over the whole SMD volume (this introduces an uncertainty of approximately 2 $\mu$m). The intersection points of this line with the SMD wafers are used as the prediction of the hits. The measured hit position is obtained by transforming the local measured hit in wafer coordinates to the global coordinate frame. In the calibration procedure it is important to determine the relative position of the SMD with respect to the TEC coordinate frame. Therefore,

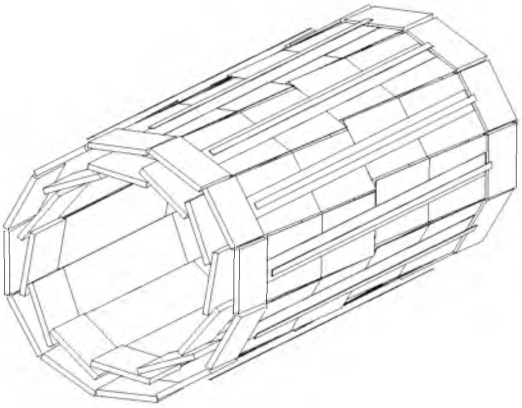

Figure 2.4: View of the SMD ladders.

an additional rotation and translation are applied to the internal alignment parameters. The TEC is calibrated with the tracks extrapolated from the SMD, so that an iterative procedure of SMD global alignment and TEC calibration is performed. The pairs of $e^+e^-$ or $\mu^+\mu^-$ tracks are assumed to form a single trajectory with a fixed curvature in the TEC. The predicted hit positions in the TEC are then compared to the measured drift times for each wire, which yields the TEC calibration.

The position resolution for detecting a charged particle in the central tracker changes from 10 $\mu$m in the SMD and 50 $\mu$m in the TEC to 300 $\mu$m in the Z-chamber or 200 $\mu$m in the FTC [47]. The high resolution of the SMD makes good track extrapolation to its origin possible. This is particularly important for the b quark tagging capability.

The transverse momentum resolution in the TEC is

$$\frac{\Delta p_t}{p_t} = 0.018 p_t \ [\text{GeV}^{-1}] \quad , \tag{2.2}$$

neglecting multiple scattering, which becomes dominant when $p_t < 400$ MeV [46]. If the SMD is used in the track fit, the resolution improves by approximately a factor $\frac{2}{3}$ [47].

Prior to a track fit, is to select the right hits in the TEC. This is done by a Minimum Spanning Tree method (MST) [48]. The MST algorithm pairs hits on adjacent TEC wires into doublets. A pair of doublets with a hit in common is taken together, and more doublets are added to form a chain, or tree, of hits. If more than one doublet can be added to a tree of hits, only the doublet which gives the minimum increase to the tree length is added. If there are no more possible doublets to add to the trees, or if the tree spans the maximal track length, the collection of hits stops. Then a circle is fitted to trees that have a minimum of 4 (5) hits in the inner (outer) TEC. Track segments which have a good fit are merged, such that the longest possible tracks are formed. Along the segments it is checked whether there are left-over hits that actually belong to the segment.

Due to the magnetic field, a charged particle describes a circle in the $x-y$ plane and therefore a circle fit is performed when a pattern of hits has been found in the TEC. Subsequently, the fit is extrapolated to the Z-chamber and, for data taken in 1994 (when the SMD became fully operational) or later, to the inner and outer SMD. If hits are found in these subdetectors, the track is refitted.

## 2.3 Data Acquisition and Processing

The typical beam crossing rate at the interaction point of L3 is 45 kHz. A trigger system selects crossings producing $e^+e^-$ interactions with high efficiency (almost 100%) [49], so that the corresponding data recording rate is just a few Hz. The trigger system consists of three levels and is designed such that physics events are well separated from background as beam-gas and beam-wall interactions and noise in electronic channels. Information of different subdetectors is used in the triggering. In the last level of the trigger system, information of the whole data acquisition system is used to reconstruct the event completely, even before the trigger decision is made. Once the event has passed the last trigger level, the digitized data from all the subdetectors are stored on tape and later processed by an offline reconstruction program. In this processing, the digitized data are converted to, e.g., energy deposits in the ECAL and hits in the TEC. Then, the pattern recognition for each subdetector is performed, e.g., energy deposits in individual calorimeter crystals are converted to energy "bumps" (group of crystals containing energy deposits) and hits to tracks, and finally the ECAL and HCAL bumps are matched to the TEC tracks, under certain conditions as $|\phi_{\mathrm{TEC}} - \phi_{\mathrm{ECAL}}| < 10^\circ$. The data are stored in several formats, of which the so-called DVN format is the one used for physics analyses.

## 2.4 Detector Simulation

Since detectors are not perfect – there is always some noise present, there may be parts which are not functioning well, there is less than 100% acceptance and there are also measurement fluctuations, since the detector has finite resolution (see section 2.2.2) – its efficiencies and accuracies are studied by making use of a Monte Carlo (MC) simulation program. The program is built around the GEANT [50] package, which contains a detailed description of the interactions of the generated particles with any detector material. Based on GEANT, a software package called SIL3 simulates the response of the L3 detector, including its finite resolution, to the particles as they would traverse the detector. Inefficiencies present in the subdetectors are dealt with by using a database which keeps track of the subdetector performances during actual data-taking runs.

As input for the detector simulation program, MC models are used to describe final-state particles of $e^+e^-$ events according to QCD inspired physics models. A well known generator for these events is JETSET [37]. After the detector simulation one distinguishes two levels: "ideal" detector MC simulation, in which the time independent detector response, as acceptance and intrinsic resolution, is simulated, and "real" detector MC simulation, where time dependent detector effects are included, as inefficiencies, malfunctioning of the different subdetectors and beam-gas and beam-wall interactions.

The detector level MC is written in the same formats (e.g., DVN) as the data. One is thus able to compare measurable quantities at the generator level of the MC to those at the detector level (ideal or real). In this way, it is possible to study the effects of the detector on these quantities.

# Chapter 3

# Measurement of the Region of Homogeneity in Hadronic Z decays

In this chapter, Bose-Einstein correlations (BEC) are investigated in hadronic Z decays in two and three components of the four-momentum difference $Q$ in the longitudinal centre-of-mass system (LCMS). As explained in chapter 1, these correlations serve as a measure of the region of homogeneity of pion emission, via eqn. (1.4). By investigating BEC in different directions, the possibly non-spherical shape and size of the region of homogeneity can be measured.

The outline of the chapter is as follows. Firstly, the relevance of this analysis is shown and the LCMS is defined. Secondly, the event- and charged-particle selection will be given, followed by a study of experimental resolution of the different variables used in the analysis. Then, it is explained how the analysis is done. Special attention will be paid to the mixing procedure applied to build the reference sample needed for the construction of the correlation function and also to the unfolding of the data for detector related effects, such as acceptance, resolution, and particle misidentification. In the sections following that, the parametrization of the correlation function will be discussed, the results including the systematic uncertainties will be given and a comparison will be made with the prediction of the JETSET Monte Carlo (MC). Finally, the conclusions will be summarized and a comparison will be made with the results of other LEP experiments.

This chapter is a more detailed description of the analysis published in [51].

## 3.1 Relevance of the Analysis

So far, no appropriate theory exists which can describe the process of hadron production (or parton fragmentation) in general and BE effects in particular. To help in arriving at an understanding of these phenomena, studies have been made of identical-boson correlations in $e^+e^-$ collisions at LEP energies in terms of the four-momentum difference $Q$, and using two- and three-dimensional distributions in components of $Q$ [51–53]. The shape of the correlation function in more than one dimension has been a subject of theoretical study in recent years [10,38,54–58]. In MC generators, spherical symmetry is assumed [23,42,59], even though elongation can be expected when a string-like shape is maintained [38,54,60].

Besides the extraction of important information on QCD in a sector where perturbative methods are not applicable, there is another need for a multi-dimensional BE analysis. BEC can, in principle, have an impact on the measurements of the W mass [23,25–31] in the four-jet channel $W^+W^- \rightarrow q_1\bar{q}_2q_3\bar{q}_4$. The experimentally observed radius of hadron emission is of order 1 fm, ten times the distance between the $W^+W^-$ decay vertices at LEP2. The actual $W^+W^-$ overlap is of course determined by the precise (non-spherical) shape and size in space-time, and these can be extracted from a multi-dimensional BE analysis. Because of the limited statistics of only a few thousand WW events such a multi-dimensional analysis cannot be carried out on the W, itself. Apart from the quark flavour composition, we, however, expect hadronic Z decay to be similar to hadronic W decay. Therefore, by studying the shape and size of the region of homogeneity (in more than one dimension) in a sample of one million events of hadronic Z decay, we get a handle on the amount of overlap between the two hadronically decaying systems of two W's.

### 3.1.1 The Longitudinal Centre-of-Mass System

In extracting the region of homogeneity in more than one dimension, it is important to decouple the energy difference (and therefore the difference in emission time in Fourier transformed space) of the particles from the difference in momentum components (and therefore the difference in purely spatial components in Fourier transformed space).

Therefore, in this analysis the longitudinal centre-of-mass system (LCMS) is used [56]. This system is defined for each pair of particles as that system in which the sum of their momenta is perpendicular to the thrust axis $\vec{n}$. This axis is defined so as to maximize

$$T \equiv \frac{\sum_i |\vec{p}_i \cdot \vec{n}|}{\sum_i |\vec{p}_i|} \quad , \tag{3.1}$$

where the sums run over all the particles in an event and $\vec{p}_i$ is the momentum vector of particle $i$. For events with a two- or three-jet topology, this axis approximates the direction of the two initial quarks. From here on, the direction of the thrust axis is referred to as the longitudinal direction. Since each pair of particles has longitudinal momentum component zero, also its rapidity is zero in the LCMS.

To see the advantage of the LCMS, the three-momentum difference of the pair of particles is resolved into a component $Q_\mathrm{L}$ parallel to the thrust axis, $Q_\mathrm{out}$ along the sum of the particles' momenta (see fig. 3.1) and $Q_\mathrm{side}$ perpendicular to both $Q_\mathrm{L}$ and $Q_\mathrm{out}$. Then, one can write the invariant four-momentum difference as

$$Q^2 = Q_\mathrm{L}^2 + Q_\mathrm{side}^2 + Q_\mathrm{out}^2(1-\beta^2) \quad , \tag{3.2}$$

where

$$\beta \equiv \frac{p_{\mathrm{out}\,1} + p_{\mathrm{out}\,2}}{E_1 + E_2} \quad , \tag{3.3}$$

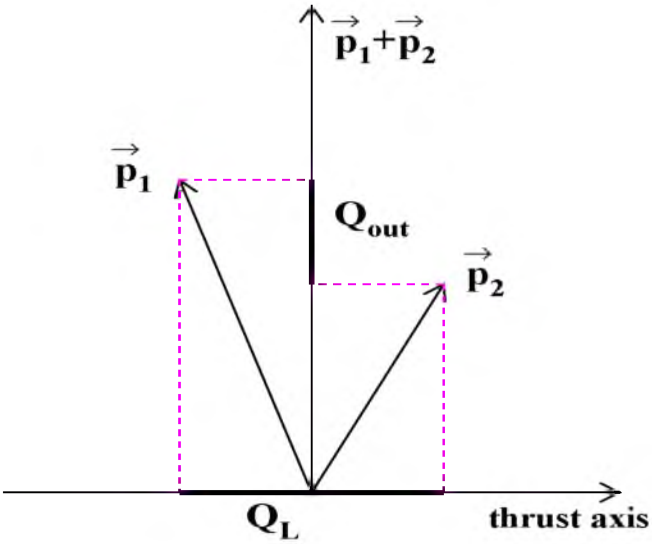

Figure 3.1: LCMS projection onto the $(Q_\mathrm{L}, Q_\mathrm{out})$ plane.

with $p_{\mathrm{out}\,i}$ and $E_i$ ($i$=1,2) the momenta in the out-direction and energies of the particles in the LCMS, respectively. The advantage of the LCMS now becomes apparent: the energy difference and, therefore, the difference in emission time of the particles couples only to the component $Q_\mathrm{out}$. So, the longitudinal and side components are pure momentum components and, therefore, in Fourier transformed space, a measure of the length of homogeneity in longitudinal and (assuming $R_2$ to be invariant under the transformation $Q_\mathrm{side} \rightarrow -Q_\mathrm{side}$) transverse direction, respectively.

For a two-dimensional analysis, $Q_\mathrm{L}$ and the transverse component $Q_\mathrm{T}$ defined as $(Q^2_\mathrm{out} + Q^2_\mathrm{side})^{1/2}$ are used. When performing a three-dimensional analysis, the components $Q_\mathrm{L}$, $Q_\mathrm{out}$ and $Q_\mathrm{side}$ are used. The two-dimensional analysis, which, with the given statistics, can be performed in smaller bins, serves as a cross-check.

## 3.2 Charged Hadron Selection

The data used in this analysis are from a sample of hadronic events collected in 1994 at the centre-of-mass energy of $\sqrt{s} \simeq 91.2$ GeV. To obtain a pure sample of $\mathrm{e^+e^-} \rightarrow \mathrm{Z} \rightarrow \mathrm{q\bar{q}}$ events, a hadronic event selection is applied.

To study BEC in the kinematic variable $Q$, and even in different components of this variable, demands a high degree of accuracy on the determination of the particle momentum as well as a good precision of reconstructing two (nearby) particles and two-particle resolution. Therefore, the data selection uses information on charged particles from the TEC and the SMD. In principle, also information from the calorimeter can be used. However, since the granularity of the calorimeter is not fine enough and the width of the showers produced by the particles is not very narrow, two nearby particles may result in a single energy deposit. Thus, there is no good one-to-one correspondence between the energy deposits and the particles. Furthermore, particles with low momentum cannot be measured as accurately in the calorimeter as charged particles can be measured in the central tracker, even when the particles are isolated.

In the following, two sets of cuts are described: cuts to select good quality tracks, corresponding to fitted paths of charged particles, and cuts to reject events which are background or which contain too many poorly measured tracks. Both sets of cuts are based on the information of the TEC and the SMD. The event selection results in a pure sample of $\mathrm{Z} \rightarrow \mathrm{q\bar{q}}$ events and it has been verified that the difference to the results obtained with a calorimeter based event selection, turns out to be negligible.

### 3.2.1 Track Selection

Firstly, criteria have to be defined to select tracks which are well reconstructed in the central tracker. There are a number of parameters on the basis of which one can decide if a track is good or not. A good track must have a high probability of coming from the interaction point and not being a misidentified track segment, a cosmic ray crossing the tracker, or a stray beam particle. The quantities used to determine the goodness of tracks are listed and described below. Figures in this subsection show the cuts (indicated by arrows) applied to reject badly reconstructed tracks. In all these figures, all other cuts described in this subsection and in subsection 3.2.2 have already been applied. The data are shown by dots and the MC generated events, which have been passed through the L3 detector simulation program [61], reconstructed and subjected to the same selection criteria as the data (detector level MC), by the histograms. For the MC generation, JETSET with BE effects according to the $\mathrm{BE}_0$ algorithm, is used. Since this is the only model (with BE simulation) according to which hadronic Z decay events have been generated and fully simulated and reconstructed within L3, and which is tuned to the L3 Z decay data, this is the only one we are able to use to compare with raw data distributions. Both data and MC are normalized to unity, so that they represent probability densities $P$ defined as $P(X) \equiv \frac{\mathrm{d}N}{\mathrm{d}X}$ for variable $X$, where $\mathrm{d}N$ is the number of entries in bin $\mathrm{d}X$, normalized such that $\int_X \frac{\mathrm{d}N}{\mathrm{d}X}\,\mathrm{d}X = 1$.

**Distance of Closest Approach**

To check if the track originates from the interaction point, the track is extrapolated back to the vertex. The distance of closest approach (DCA) of the track is defined as the smallest distance of the extrapolated track to the interaction point in the plane perpendicular to the beam direction, i.e., the bending plane of the magnetic field. Tracks are required to have a DCA less than 5 mm. Fig. 3.2 shows the corresponding distribution for tracks from the data and those from MC.

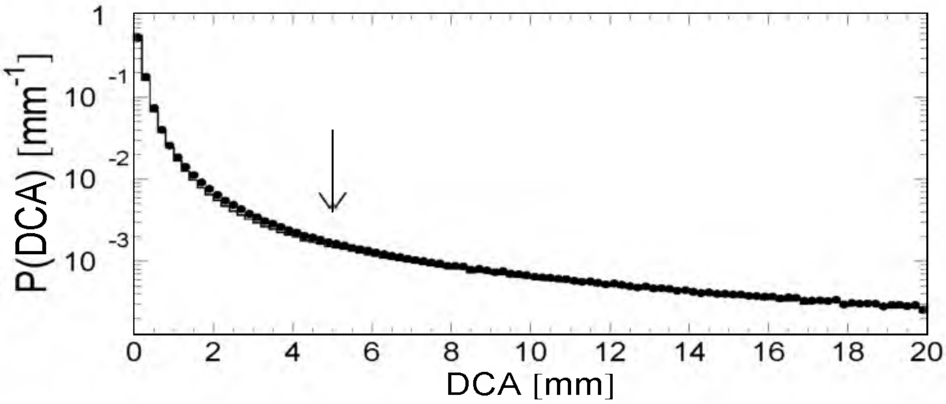

Figure 3.2: DCA of a track in mm. Data are presented by dots and MC by the histogram. The arrow indicates the position of the cut.

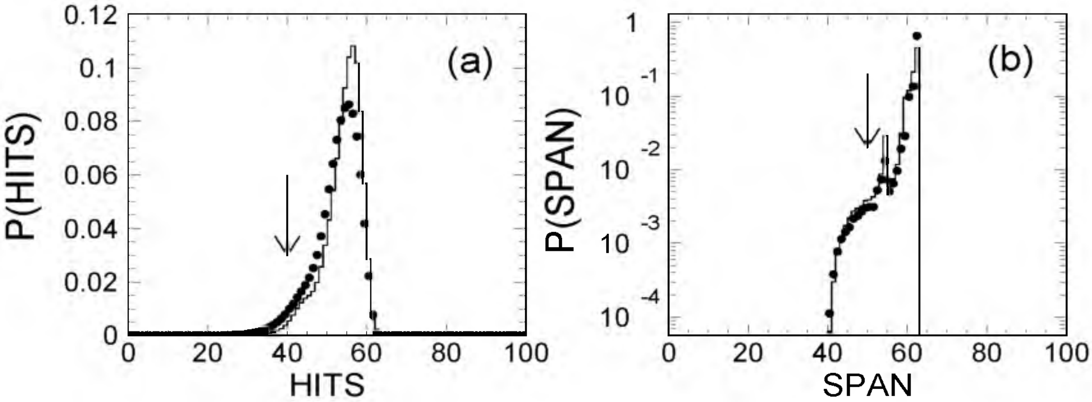

Figure 3.3: (a) Number of hits caused by a track, (b) Span of the track. Data are presented by dots, MC by the histogram.

**Number of Hits**

A track originating from the interaction point and passing through TEC can cause a signal ("hit") on a maximum of 62 wires. Misidentified track segments and poorly reconstructed tracks would usually have a much smaller number of hits. A good track is therefore required to have at least 40 hits. Fig. 3.3a shows the distribution of the number of hits caused by data and MC tracks. There is a clear discrepancy between data and MC, which is mainly due to an underestimation of the number of hits missing in the inner sector of TEC in the MC simulation.

**Span of the Track**
A track is reconstructed by combining hits. Sometimes, track segments are reconstructed from hits belonging to different tracks. In general, these misreconstructed tracks have a smaller length than that expected for tracks originating from the interaction point and crossing through the entire TEC. The difference between the number of wires between the first and last hit, called span, is used as a measure for the track length. Fig. 3.3b shows the comparison of the span coming from data and MC tracks. All tracks are required to have a span of at least 50, implying that only tracks with $39° < \theta < 131°$ can be accepted. The small peak around 54 is due to tracks for which the hits in the inner TEC were not used in the reconstruction.

The three cuts presented so far are applied to select well reconstructed tracks and to reduce the fraction of tracks that are not associated with particles originating from the $e^+e^-$ interaction (secondaries). Secondaries are characterized by a high DCA and a low number of hits and span. After applying these cuts, the contamination of secondaries in an event is reduced to approximately 3%.

**Transverse Momentum**
The TEC measures the momentum of a track from its curvature in the plane transverse to the beam axis, which is the bending plane of the magnetic field. The momentum component of a track in this plane is required to be greater than 100 MeV. Tracks which have a smaller transverse momentum cannot cross the TEC and cannot be measured accurately.

### 3.2.2 Event Selection

The sample of events used in the previous subsection contains some background events as well as events in which the track quality is not good. Since we are interested in a pure sample of events with good tracks, the sample is passed through a selection procedure.

**Theta of Thrust Axis**
Since information is used from TEC and SMD, the first requirement is that the thrust axis is within the full acceptance of the central tracking chamber ($44° < \theta < 136°$). The following cut is made:

$$|\cos\theta_{\text{thr}}| < 0.7 \quad , \tag{3.4}$$

where $\theta_{\text{thr}}$ is the polar angle of the thrust axis as determined from tracks only.

**Total Energy**
Fig. 3.4 shows the distribution of the total energy sum, $E_{\text{tot}}$, of the tracks, normalized to the centre-of-mass energy, $\sqrt{s}$. Note that each track is considered to be a pion. The $e^+e^- \to Z \to q\bar{q}$ events are characterized by a relatively large fraction $E_{\text{tot}}/\sqrt{s}$. Mainly to remove two-photon events where a $q\bar{q}$ pair is formed after the interaction of the two photons, i.e., $e^+e^- \to e^+e^-q\bar{q}$ events, the following cut is applied on the total energy of

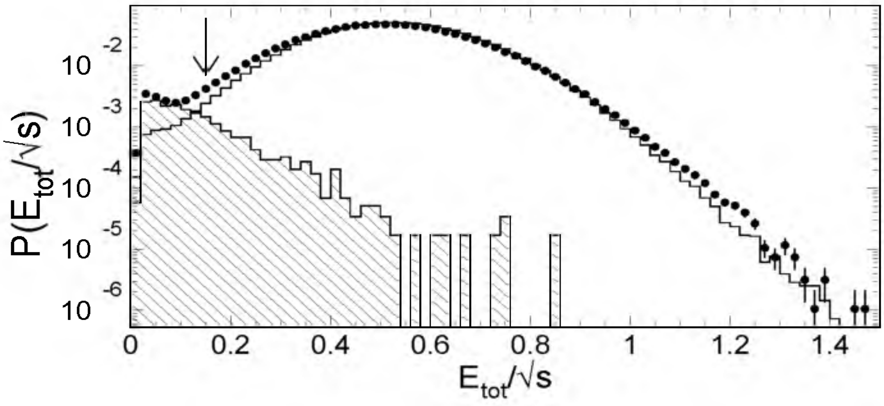

Figure 3.4: Total energy of the tracks normalized to the centre-of-mass energy. Data are presented by dots, MC by the open histogram. The dashed histogram is the background expectation for the two-photon events $e^+e^- \to e^+e^-q\bar{q}$.

the tracks:

$$\frac{E_{\rm tot}}{\sqrt{s}} \equiv \frac{\sum_i E_i}{\sqrt{s}} > 0.15 \quad , \tag{3.5}$$

where $E_i$ is the energy of track $i$ and where the sum runs over all tracks of an event. The prediction of the two-photon events by MC is shown as the dashed histogram in fig. 3.4. Also some beam-gas and beam-wall interaction events are removed by this cut, but the fraction is much smaller than for the two-photon events.

**Parallel and Transverse Momentum Imbalance**

Both the sum of momentum components along the beam direction, $P_{\|}$, and in the plane perpendicular to the beam direction, $P_{\perp}$, should ideally be zero for hadronic Z decay events. This is because at LEP the laboratory frame is also the centre-of-mass frame. The limited acceptance, beam-gas and beam-wall interaction events, two-photon events and poor track measurements all give rise to parallel and perpendicular momentum imbalances.

The following cuts are applied:

$$\frac{P_{\|}}{E_{\rm tot}} \equiv \frac{|\sum_i p_{\| i}|}{\sum_i E_i} < 0.75 \quad \text{and} \quad \frac{P_{\perp}}{E_{\rm tot}} \equiv \frac{|\sum_i \vec{p}_{\perp i}|}{\sum_i E_i} < 0.75 \quad , \tag{3.6}$$

where $E_i$ is the energy of track $i$ with momentum components $p_{\| i}$ parallel to the beam direction and $\vec{p}_{\perp i}$ in the plane perpendicular to the beam direction, and where the sum runs over all tracks of an event. Fig. 3.5 shows the distributions of $P_{\|}/E_{\rm tot}$ and $P_{\perp}/E_{\rm tot}$.

**Charged-Particle Multiplicity**

Fig. 3.6 shows the charged-particle (or track) multiplicity distribution for data and MC. Only events with a charged-particle multiplicity, $N_{\rm ch}$, larger than 4 are accepted.

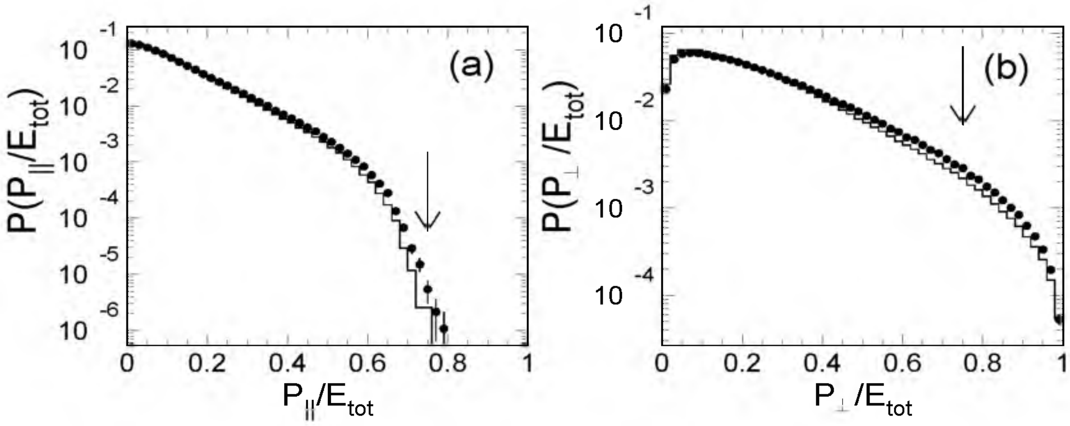

Figure 3.5: (a) Momentum imbalance along the beam direction, (b) momentum imbalance in the plane perpendicular to the beam direction. Both imbalances are normalized to the total energy of the tracks. Data are presented by dots, MC by the histogram.

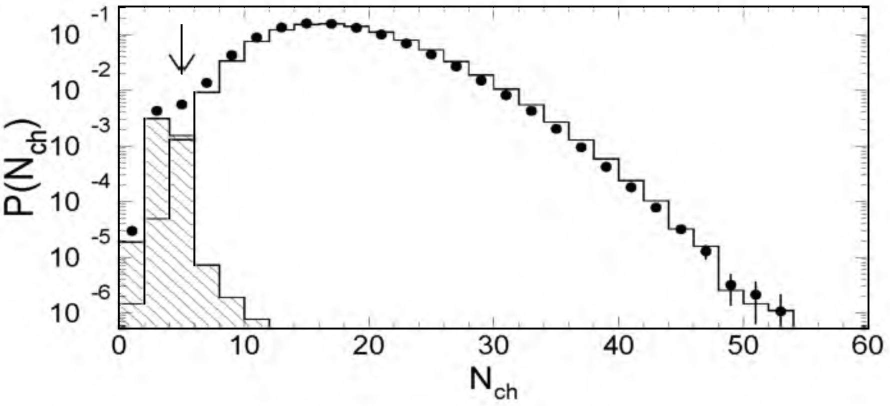

Figure 3.6: Charged-particle multiplicity distribution. Data are presented by dots, MC by the open histogram. The dashed histogram is the background expectation for $e^+e^- \rightarrow \ell^+\ell^-$ events, where $\ell$ = e, $\mu$ or $\tau$.

This cut is mainly to reduce the leptonic events, $e^+e^- \rightarrow Z \rightarrow \ell^+\ell^-$, where $\ell$ is a charged lepton (e, $\mu$, $\tau$), see the dashed histogram in fig. 3.6, but also some beam-gas and beam-wall interaction events and two-photon events are removed by this cut.

**Second Largest Angle, $\phi_2$**

$e^+e^- \rightarrow Z \rightarrow \tau^+\tau^-$ events in which both $\tau$ particles decay into charged particles are a background to the hadronic events. Fig. 3.7 shows the distribution of the second largest angle, $\phi_2$, in the $r-\phi$ plane between any two neighbouring tracks in an event. The prediction of MC for $e^+e^- \rightarrow Z \rightarrow \tau^+\tau^-$ events is indicated by the dashed histogram. By

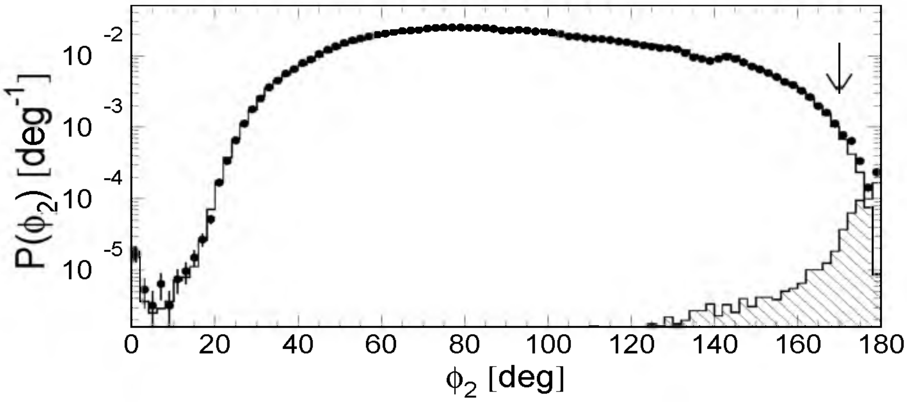

Figure 3.7: Distribution of the second largest angle, $\phi_2$, between any two neighbouring tracks in an event. Data are presented by dots, MC by the histogram. The dashed histogram is the background expectation for $\tau^+\tau^-$ events.

excluding events with $\phi_2$ more than 170°, most of the $\tau^+\tau^-$ events are removed.

A total of about one million events satisfy all the selection criteria. After the selection the $\tau^+\tau^-$ contamination is approximately $10^{-4}$ and the two-photon contamination approximately $2 \cdot 10^{-5}$. Note that the background events are peaked at low multiplicity $n$, while the contribution of the background events to the $Q$ distribution is approximately proportional to $\frac{n}{2}(\frac{n}{2} - 1)$. Consequently, this contribution is even much smaller than the numbers quoted above.

### 3.2.3 Two-track Reconstruction

In the previous two subsections, we selected hadronic Z decay events and good quality tracks. However, no attention has yet been paid to the precision of the two-track reconstruction, which is crucial when we want to study BEC. For the computation of $Q$, a good reconstruction of the angle between the tracks is important, especially for low values of $Q$. For this reason, additional cuts on tracks are imposed to ensure good precision of the reconstruction of variables, such as $Q$ and the difference in polar and azimuthal angles between two tracks, $\delta\theta$ and $\delta\phi$. Note that these additional cuts are not applied in the figures of the previous two subsections. The additional cuts require that when no hit in the Z-chamber (or in the FTCs) is found and an energy deposit in the ECAL is used to recover for this missing hit, the track is removed. This is necessary because in the MC simulation of the detector, this was not done correctly. When the opening angle between two like-sign tracks is less than 3°, the detector efficiency to resolve the two tracks drops drastically. Only after the additional cuts does the MC simulate the difference in polar and azimuthal angle between two nearby tracks, and consequently the efficiency of resolving two nearby tracks, reasonably well (see below).

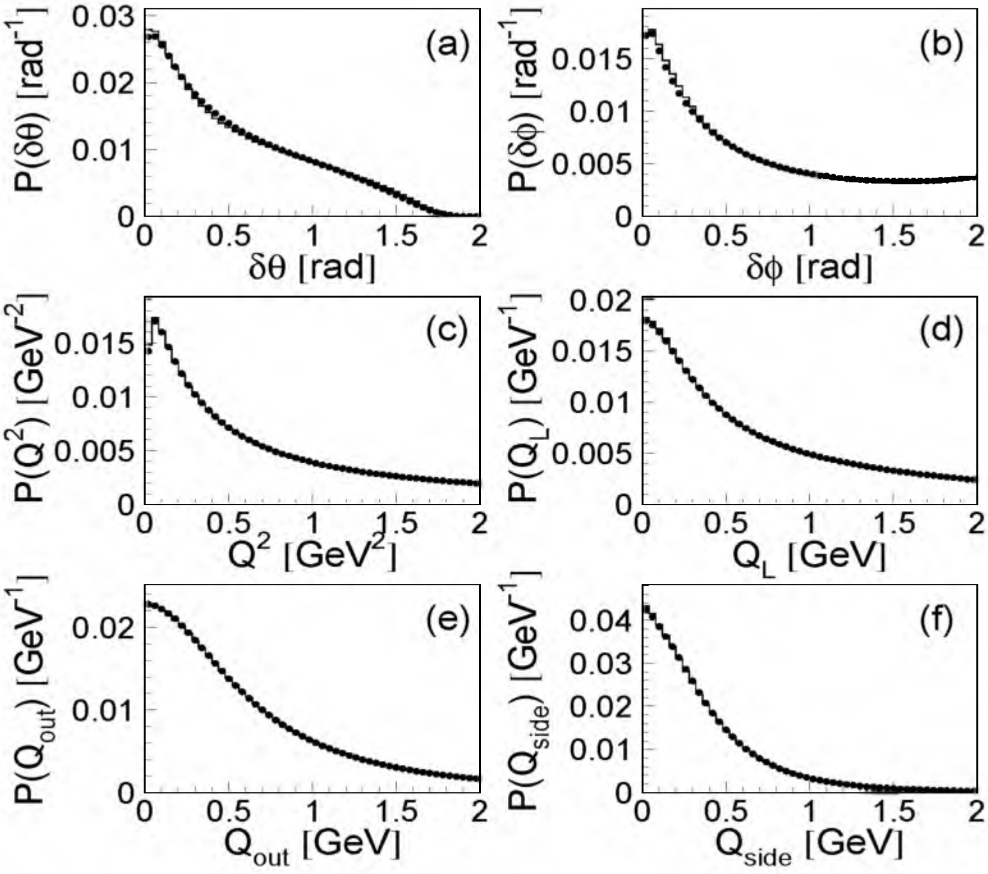

Figure 3.8: Distributions of (a) the difference in polar angle of pairs of tracks, $\delta\theta$, (b) the difference in azimuthal angle of pairs of tracks, $\delta\phi$, (c) the inclusive four-momentum difference squared, $Q^2$, and the (d) longitudinal, (e) out, and (f) side components of the inclusive four-momentum difference $Q$, for the data (dots) compared to the predictions of JETSET with BE after detector simulation (histogram).

Together with all the previous cuts on tracks, about 40% of the tracks are rejected (30% of the tracks are rejected by the last cut), which results in a residual average charged-particle multiplicity of approximately 12 and a total of about 36 million like-sign track pairs in the one million selected events. With this selection, good agreement is obtained between data and MC simulation for the distributions of the differences between pairs of tracks of the azimuthal and polar angles with respect to the beam direction, as well as for the distributions of $Q^2$ and the different components $Q_{\mathrm{L}}$, $Q_{\mathrm{out}}$ and $Q_{\mathrm{side}}$ used in this analysis. This is shown in fig. 3.8, where the data are compared to JETSET (including BE effects) generated events which have been passed through the L3 detector simulation program, reconstructed and subjected to the same selection criteria as the data. Similar comparisons using events generated with JETSET without BEC or by HERWIG [40] also show good agreement, except for small values of the variables.

## 3.3 Resolution

Measurements of BEC involve counting pairs of like-sign particles in small bins of the different components $Q_{\rm L}$, $Q_{\rm T}$, $Q_{\rm out}$ and $Q_{\rm side}$. To avoid systematic bias arising from the limited detector performance to measure the different components of $Q$ accurately, the bin size for these different components should be larger than this resolution.

The resolution in the different variables used in the analysis is estimated using MC generated events. After generation, these events are passed through the L3 detector simulation program, reconstructed and subjected to track and event selection in the same way as the data. Let $X$ be the value of a variable computed from a MC event at the generator level and let $X'$ be the value of this same variable computed from the event at the detector level. Then, a distribution is obtained for the resolution from the difference $\delta X = X' - X$ for a sufficiently large sample of MC events.

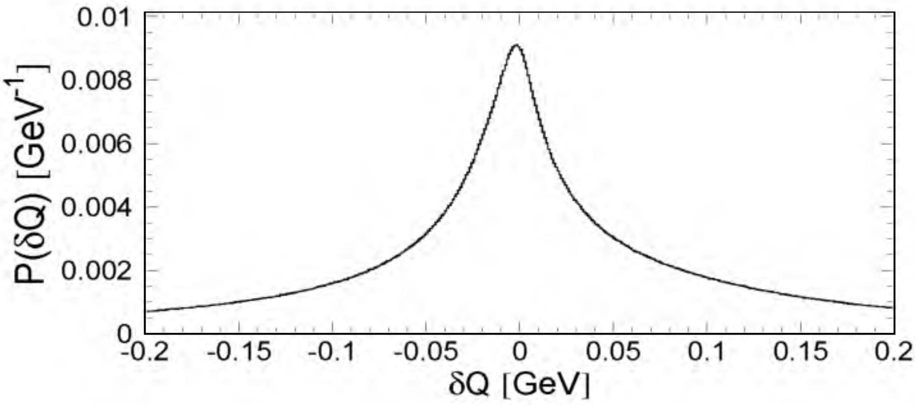

Figure 3.9: Resolution $\delta Q$, in GeV, of the four-momentum difference, $Q$, between like-sign tracks according to JETSET.

As an illustration, the resolution for the four-momentum difference between two like-sign tracks found using 500k events generated by JETSET (with BE), is presented in fig. 3.9, see also [62]. Since this histogram is normalized to unity, it represents the probability density $P(\delta X)$ of a deviation $\delta X$ from $X$ after the L3 detector simulation, reconstruction and selection. It is clear that the histogram has non-Gaussian tails. The value of half-width at half-maximum (HWHM), $H$, will be used as a characteristic of the resolution.

However, $H$ obtained in this way is only an average of the resolution for $Q$. In fact, the resolution strongly depends on the value of $Q$ itself. The dependence of $\delta Q$ on the value of $Q$, found using 500k JETSET generated events is shown in fig. 3.10. It is clear that the best resolution is obtained for small values of $Q$. This is a pleasant feature since BEC are strongest at small values of $Q$.

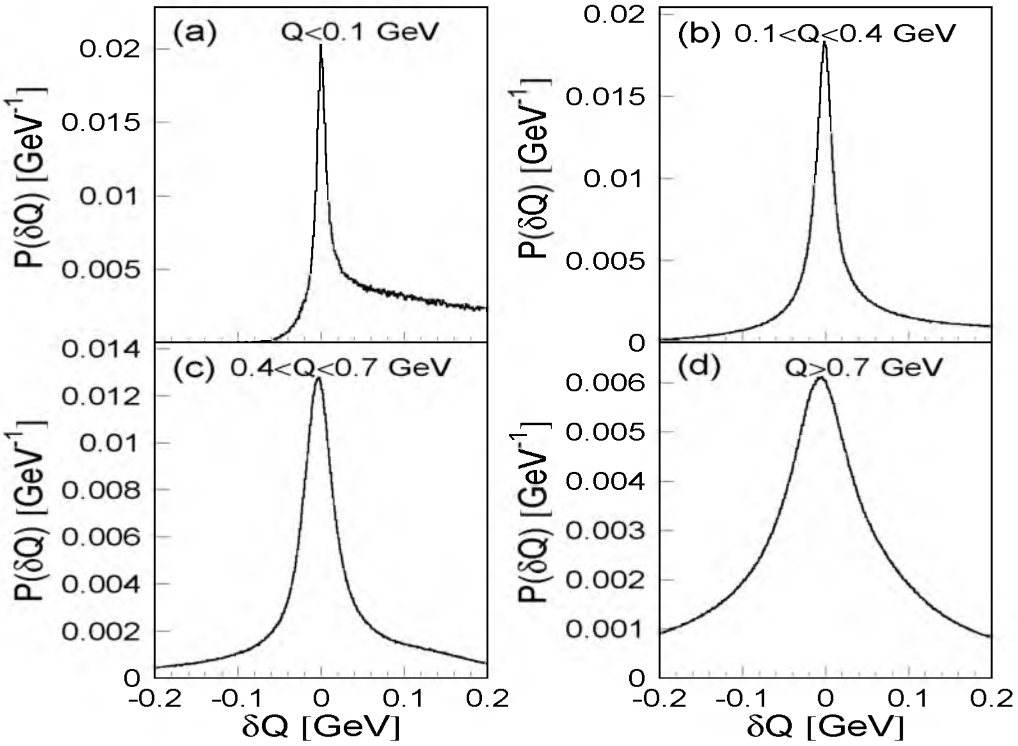

Figure 3.10: Resolution $\delta Q$, in GeV, of the variable $Q$ between like-sign tracks according to JETSET, for different cuts on $Q$ computed at the generator level of JETSET: (a) $Q < 0.1$, (b) $0.1 < Q < 0.4$, (c) $0.4 < Q < 0.7$, (d) $Q > 0.7$ (in GeV).

For the analysis, we need the resolution of the variables $Q_{\mathrm{L}}$, $Q_{\mathrm{T}}$, $Q_{\mathrm{out}}$ and $Q_{\mathrm{side}}$, separately. Table 3.1 shows $H$ for these different variables. The errors were determined using three different MC samples: JETSET with and without BE effects and HERWIG, each based on approximately 500k events. The maximum deviation that is found with respect to the average value of $H$, is taken as the error.

Knowing the resolution of the variables, we choose a bin size of 40 MeV for the two-dimensional analysis and 80 MeV for the three-dimensional analysis. This way the statistics are also sufficient to perform the analyses.

## 3.4 Determination of $R_2$

In both the two- and three-dimensional analyses, the BE correlation function

$$R_2(p_1, p_2) = \frac{\rho_2(p_1, p_2)}{\rho_{0,2}(p_1, p_2)} \tag{3.7}$$

Table 3.1: $H$ (in MeV) for the different variables $Q_i$ (i=L, T, out, side) as a function of $Q$ computed at generator level MC (in MeV).

| range (MeV) | $H$ ($i = \mathrm{L}$) | $H$ ($i = \mathrm{T}$) | $H$ ($i = \mathrm{out}$) | $H$ ($i = \mathrm{side}$) |
|---|---|---|---|---|
| $Q \leqslant 100$ | $11 \pm 2$ | $18 \pm 3$ | $25 \pm 2$ | $11 \pm 2$ |
| $100 \leqslant Q \leqslant 400$ | $17 \pm 1$ | $23 \pm 1$ | $34 \pm 2$ | $15 \pm 1$ |
| $400 \leqslant Q \leqslant 700$ | $26 \pm 2$ | $32 \pm 2$ | $47 \pm 2$ | $26 \pm 2$ |
| $Q \geqslant 700$ | $57 \pm 3$ | $62 \pm 3$ | $81 \pm 3$ | $42 \pm 3$ |
| all $Q$ | $38 \pm 2$ | $42 \pm 2$ | $62 \pm 3$ | $29 \pm 2$ |

is measured as a function of $Q_\mathrm{L}$, and $Q_\mathrm{T}$ or $Q_\mathrm{out}$ and $Q_\mathrm{side}$ by counting the number of like-sign pairs in bins of these variables for the data and a "reference sample".

### 3.4.1 The Reference Sample

There is much controversy, see, e.g., [5–7, 51–53], on the determination of the reference sample from which $\rho_{0,2}$ is determined. This is due to the fact that $\rho_{0,2}$ should include all correlations, such as energy-momentum conservation and correlations due to resonance decays, except those of BE. Since such a sample does not exist in nature, we are obliged to construct it ourselves.

There are three commonly used methods to determine the reference sample:

- The reference sample is formed by means of event mixing. This is based on the idea that computing the four-momentum difference between any two tracks, each one selected randomly from a different event, removes the correlations while retaining other characteristics of the data sample. A certain minimum number of events is needed to do the event mixing, so the data sample needs to be large enough to apply this mixing technique.

- The reference sample is formed by computing $Q$ for *unlike-sign* particle pairs. Since BEC only occur between identical bosons, this would be a good reference sample. However, a bias is introduced due to the presence of resonances like $\rho$ and $\omega$, which occur between unlike-sign particles but not between like-sign particles.

- The reference sample is formed by using a MC without BEC. This is the easiest way to make the reference sample, but one has to "believe" that the MC describes the data in all aspects except for the BE effect.

In this analysis, the reference sample is formed by mixing particles from different data events in the following way. Firstly, events are rotated to a system with the $z$-axis along the thrust axis and are stored in a "pool". Then, tracks of each new event outside the pool are exchanged by tracks of the same charge from events in the pool of the same multiplicity class (i.e., the same within $\sim 20\%$) under the condition that no track originates from the same event. Thus, after this procedure the new event consists of tracks originating from different events in the pool, and its original tracks have entered the pool. This updating process prevents any regularities in the reference sample. Finally, $Q_L$, $Q_T$, $Q_{\mathrm{out}}$ and $Q_{\mathrm{side}}$ are calculated for each pair of tracks in the mixed event.

However, this mixing procedure removes more correlations than just those of BE. This effect is estimated by MC using a generator with no BE effects (JETSET or HERWIG). Thus, in the absence of BEC the corrected two-particle density is given by:

$$\rho_{0,2}(\vec{Q}) = \rho_{\mathrm{mix}}(\vec{Q}) \cdot C_{\mathrm{mix}}(\vec{Q}) \quad \text{, where } C_{\mathrm{mix}}(\vec{Q}) \equiv \left[\frac{\rho_2(\vec{Q})}{\rho_{\mathrm{mix}}(\vec{Q})}\right]_{\mathrm{MC,\,noBE}} \quad . \tag{3.8}$$

The vector $\vec{Q}$ is defined as $\vec{Q} \equiv (Q_L, Q_T)$ for the two-dimensional analysis, and as $\vec{Q} \equiv (Q_L, Q_{\mathrm{out}}, Q_{\mathrm{side}})$ for the three-dimensional analysis.

### 3.4.2 Unfolding of Detector Effects

The two-particle correlation function $\rho_2/\rho_{\mathrm{mix}}$ of the data must further be corrected for detector resolution, acceptance, efficiency and particle misidentification. This is done bin by bin by multiplying the raw-data values by a correction factor obtained from MC studies. Since the L3 detector does not identify hadrons, this factor, $C_{\mathrm{det}}$, is given by the ratio of the two-*pion* correlation function found from MC events at generator level to the two-*particle* correlation function found using all particles after full detector simulation, reconstruction and selection:

$$C_{\mathrm{det}}(\vec{Q}) = \left(\frac{\rho_2(\vec{Q})}{\rho_{\mathrm{mix}}(\vec{Q})}\right)_{\mathrm{gen,\,pions}} \Bigg/ \left(\frac{\rho_2(\vec{Q})}{\rho_{\mathrm{mix}}(\vec{Q})}\right)_{\mathrm{det,\,all}} \quad . \tag{3.9}$$

Note, that about 80% of all generated charged particles are pions, so that about 64% of the charged-particle pairs are pion pairs. There is no large $Q$ dependence on this percentage. As an illustration, fig. 3.11 shows the dependence of the correction factor, $C_{\mathrm{det}}$, on $Q$. The full histogram shows the distribution when JETSET with BE effects is used, the dashed histogram is for JETSET without BE. From the figure it is clear that only for low $Q$ does the correction factor deviate from a constant value (around one), but there it depends on whether BE effects are included, or not. The difference between the two MCs can be understood as follows. Since $Q$ depends both on the energy of the particles as well as on the angle between them, small $Q$ can be due to either small angles or low energies (or both). In a MC with BE effects, the fraction of pairs at small $Q$ with small angle is larger than in a MC without BE effects. Because of the limited ability of the detector to distinguish tracks that are close to each other, this leads to lower detection efficiency and hence to larger corrections. It may already be noted that the large difference between the MC with and without BEC, will lead to the largest contribution of the systematic uncertainty.

Combining eqn. (3.9) with eqns. (3.8) and (3.7) results in

$$R_2(\vec{Q}) = \frac{\rho_2(\vec{Q})}{\rho_{\mathrm{mix}}(\vec{Q})} \cdot \frac{1}{C_{\mathrm{mix}}(\vec{Q})} \cdot C_{\mathrm{det}}(\vec{Q}) \quad . \tag{3.10}$$

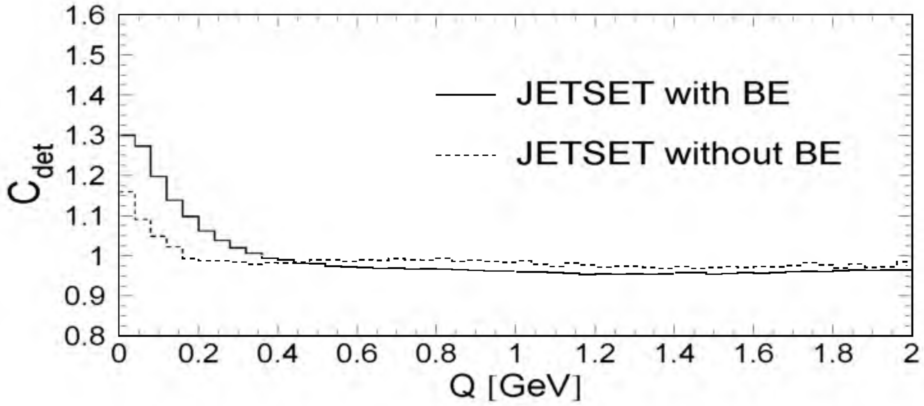

Figure 3.11: Correction factor, $C_{\text{det}}$, for JETSET with BE (full histogram) and JETSET without BE (dashed histogram).

The analysis is done in two- and three-dimensional bins of $Q$. In terms of numbers $N_{klm}$ of like-sign particle pairs in the three-dimensional bin $k$, $l$, $m$ of $Q_{\text{L}}$, $Q_{\text{out}}$ and $Q_{\text{side}}$, eqn. (3.10) becomes

$$R_{2\,klm} = \left[\frac{N_{klm}}{N^{\text{mix}}_{klm}}\right]_{\text{data}} \cdot \left[\frac{N^{\text{mix}}_{klm}}{N_{klm}}\right]_{\text{MC, noBE}} \cdot \left[\frac{N^{\text{gen}}_{klm}}{N^{\text{mix, gen}}_{klm}} \cdot \frac{N^{\text{mix, det}}_{klm}}{N^{\text{det}}_{klm}}\right]_{\text{MC}} \quad . \tag{3.11}$$

In this analysis, each $N_{klm}$ is normalized to the total number of pairs in the corresponding sample. For the two-dimensional analysis the $N_{klm}$ are replaced by $N_{kl}$, where the two-dimensional bin $k$, $l$ represents a bin of $Q_{\text{L}}$ and $Q_{\text{T}}$.

In the analysis, JETSET without BE and HERWIG (not having a BE option) are used to determine the mixing correction factor, $C_{\text{mix}}$, and JETSET (with and without BE) as well as HERWIG to determine the detector correction factor, $C_{\text{det}}$. Together with a variation on the mixing technique, the selection criteria and the fit range, these six MC combinations will serve to estimate systematic errors.

### 3.4.3 Effect of Coulomb Repulsion

No attention has yet been paid to the effect of two-particle Coulomb final-state interactions on the two-particle BE correlation function. A way to correct the data for Coulomb interactions is to weight each pair of pions by the inverse Gamow factor [9]

$$G^{-1}(\eta) = \frac{\exp(2\pi\eta) - 1}{2\pi\eta}, \quad \text{where } \eta = \pm\frac{m_\pi \alpha}{Q} \ , \tag{3.12}$$

where $m_\pi$ is the mass of the pion and $\alpha$ is the fine-structure constant. The sign is positive for like-sign pion pairs (as in this analysis) and negative for unlike-sign pairs. It is shown in [63] that this Gamow correction is in principle suitable for our purposes. Only when higher-order correlations ($\gtrsim 4$) or large source sizes ($\gtrsim 1$ fm) are considered, is the Gamow correction not applicable. From eqn. (3.12) we see, however, that only for $Q \lesssim 80\,\mathrm{MeV}$ (first bin in the three-dimensional analysis) the correction becomes sizeable ($> 4\%$). As a check, the analysis is also performed excluding this region, and no significant difference is observed. Therefore, Coulomb effects are neglected in this analysis.

## 3.5 Parametrization of $R_2$

To extract quantities related to the shape and width of the Bose-Einstein correlation function, $R_2$, the function is fitted by two kinds of parametrizations: a Gaussian parametrization and an extension of the Gaussian in terms of Hermite polynomials.

### 3.5.1 Gaussian

Assuming a Gaussian (azimuthally, but not necessarily spherically symmetric) shape of the source, the following three-dimensional parametrization has been proposed [10, 55, 64]:

$$\begin{aligned} R_2(Q_\mathrm{L}, Q_\mathrm{out}, Q_\mathrm{side}) = \gamma\,(1 + \delta Q_\mathrm{L} + \varepsilon Q_\mathrm{out} + \xi Q_\mathrm{side}) \times \\ \left[1 + \lambda \exp\left(-R_\mathrm{L}^2 Q_\mathrm{L}^2 - R_\mathrm{out}^2 Q_\mathrm{out}^2 - R_\mathrm{side}^2 Q_\mathrm{side}^2 + 2 Q_\mathrm{L} Q_\mathrm{out} R_\mathrm{L,out}^2\right)\right], \end{aligned} \quad (3.13)$$

where the factor $(1+\delta Q_\mathrm{L}+\varepsilon Q_\mathrm{out}+\xi Q_\mathrm{side})$ takes into account possible long-range momentum correlations in the form of a slow rise, $\gamma$ is a normalization factor close to unity and the term between brackets is the two-particle BE correlation function associated with the Gaussian shape of the source.

The two-dimensional analog is obviously (neglecting the $Q_\mathrm{L} Q_\mathrm{out}$ term)

$$R_2(Q_\mathrm{L}, Q_\mathrm{T}) = \gamma\,(1 + \delta Q_\mathrm{L} + \psi Q_\mathrm{T}) \left[1 + \lambda \exp\left(-R_\mathrm{L}^2 Q_\mathrm{L}^2 - R_\mathrm{T}^2 Q_\mathrm{T}^2\right)\right] \quad . \quad (3.14)$$

By fitting the correlation function with this parametrization, one can extract the incoherence factor $\lambda$, which measures the strength of the correlation, and the "radii" $R_\mathrm{L}, R_\mathrm{out}, R_\mathrm{side}$ (or $R_\mathrm{L}$, $R_\mathrm{T}$ for the two-dimensional analysis), all defined as $1/\sqrt{2}\sigma$, with $\sigma^2$ the corresponding diagonal term of the covariance matrix of the multi-dimensional Gaussian distribution of the source in space-time. In the LCMS, the duration of particle emission only couples to the out-direction and only enters in the parameters $R_\mathrm{out}$ (and thus $R_\mathrm{T}$) and $R_\mathrm{L,out}$. Hence, $R_\mathrm{side}$ can be interpreted as the transverse component of the length of homogeneity. The parametrization (3.13) assumes azimuthal symmetry of the source, which means that the Gaussian shape of the source is invariant under the transformation $Q_\mathrm{side} \to -Q_\mathrm{side}$. Consequently, the only possible off-diagonal term in the covariance matrix is the $Q_\mathrm{L} Q_\mathrm{out}$ term. $R_\mathrm{L,out}^2$ is a parameter which can be either positive or negative and the $R^2$ notation is used here just to indicate that it has the dimension of an area.

### 3.5.2 Edgeworth Expansion

There is, however, no good reason why the shape of $R_2$ should be Gaussian. An approach [65] to study possible deviations from the Gaussian, is to expand in terms of Hermite polynomials. Taking only the lowest-order non-Gaussian term into account, this so-called Edgeworth expansion [66] replaces the Gaussian in eqn. (3.13), neglecting the $Q_{\mathrm{L}}Q_{\mathrm{out}}$ term, by

$$\exp\left(-R_{\mathrm{L}}^2Q_{\mathrm{L}}^2 - R_{\mathrm{out}}^2Q_{\mathrm{out}}^2 - R_{\mathrm{side}}^2Q_{\mathrm{side}}^2\right) \\ \cdot \left[1+\frac{\kappa_{\mathrm{L}}}{3!}H_3(R_{\mathrm{L}}Q_{\mathrm{L}})\right]\cdot\left[1+\frac{\kappa_{\mathrm{out}}}{3!}H_3(R_{\mathrm{out}}Q_{\mathrm{out}})\right]\cdot\left[1+\frac{\kappa_{\mathrm{side}}}{3!}H_3(R_{\mathrm{side}}Q_{\mathrm{side}})\right] \quad ,(3.15)$$

where $\kappa_i$ $(i = \mathrm{L}, \mathrm{out}, \mathrm{side})$ measures the deviation from the Gaussian in the corresponding direction and $H_3(R_iQ_i) \equiv (\sqrt{2}R_iQ_i)^3 - 3\sqrt{2}R_iQ_i$ is the third Hermite polynomial.

It is important to note that the Hermite polynomials form a complete orthogonal set of functions in the space of square integrable functions with measure $\mathrm{d}\mu(x) = \sqrt{2}\exp(-x^2)\mathrm{d}x$, where $x$ is short for $R_iQ_i$. The BE correlation function can be represented by the Edgeworth expansion, if and only if [65]

$$\int_{-\infty}^{\infty} \sqrt{2}(R_2(x) - 1)^2\exp(x^2)\,\mathrm{d}x < \infty \quad . \tag{3.16}$$

Experimentally, this condition turns out to be satisfied.

## 3.6 Results

In this section, the method of the analysis is tested with MC and afterwards the results of the analysis are given.

### 3.6.1 Monte Carlo Test of the Method

The method is checked by using events generated by JETSET without BEC at detector level instead of the experimental data. Fits give results consistent with $\lambda = 0$ ($\chi^2/\mathrm{NDF} \simeq 1$ for $\lambda = 0$), as expected in the absence of BEC. Since JETSET with BEC describes the data best, this MC is used to determine the detector correction factor, $C_{\mathrm{det}}$. JETSET without BEC is used to determine $C_{\mathrm{mix}}$. As an illustration, fig. 3.12a shows a two-dimensional histogram of $R_2$ as a function of $Q_{\mathrm{L}}$ and $Q_{\mathrm{T}}$, as well as slices in different intervals of $Q_{\mathrm{L}}$ and $Q_{\mathrm{T}}$, when JETSET without the BE effect is used. From the figure it is clear that $R_2$ is indeed around unity. The curves in the different slices correspond to the Gaussian fit (3.14). The curves, however, show a slight enhancement at low values of $Q_{\mathrm{L}}$ and $Q_{\mathrm{T}}$, which is due to the fact that at low $Q$ the correction factor $C_{\mathrm{det}}$ depends on whether BE is included or not (see subsection 3.4.2).

The same checks were performed with similar results, i.e., $\chi^2/\mathrm{NDF} \simeq 1$ for $\lambda = 0$, (a) using HERWIG to determine the correction factor, $C_{\mathrm{det}}$, and (b) using HERWIG to determine the mixing correction factor, $C_{\mathrm{mix}}$, and JETSET (with or without BE) to determine $C_{\mathrm{det}}$.

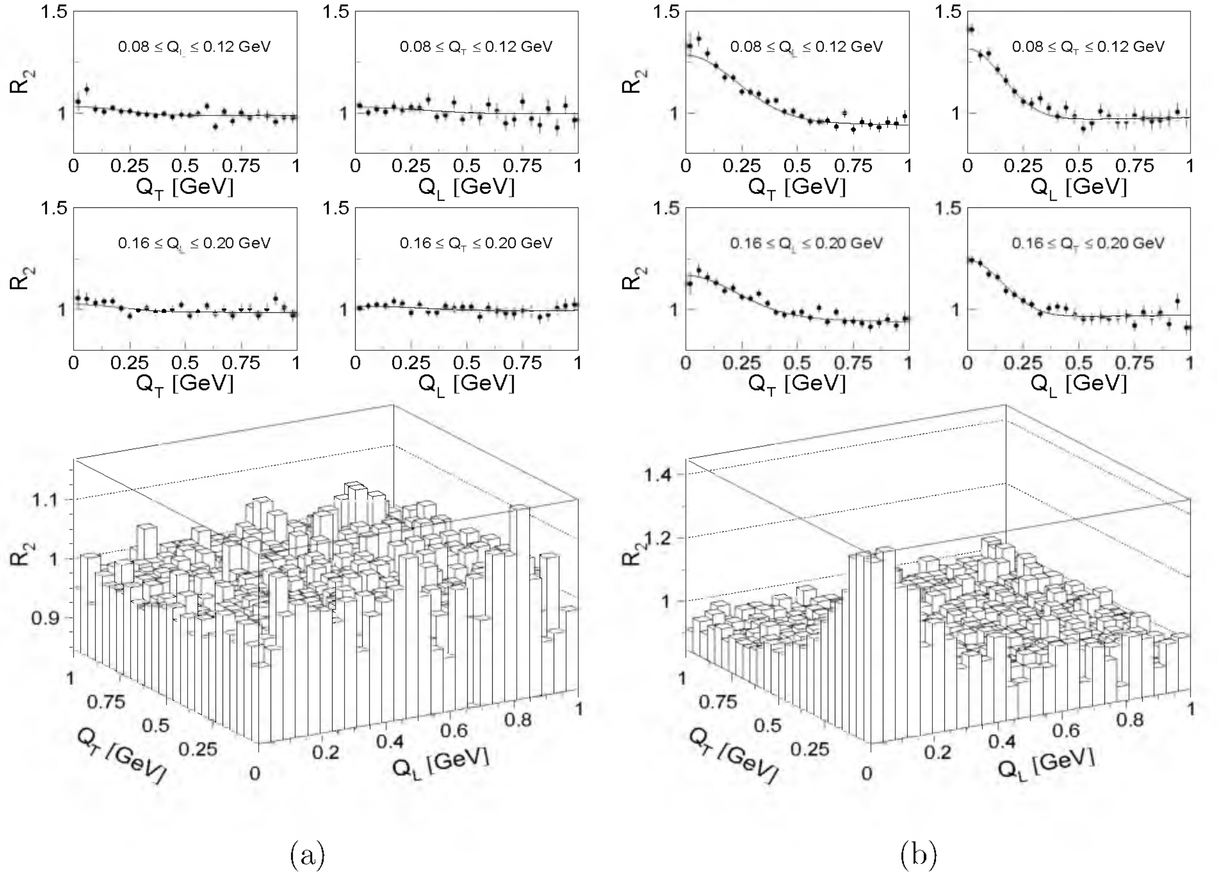

Figure 3.12: $R_2$ as a function of $Q_\mathrm{L}$ and $Q_\mathrm{T}$ for JETSET generated events at detector level when no BE effects are included, (a), for the data, (b). Also slices in different intervals of $Q_\mathrm{L}$ and $Q_\mathrm{T}$ are shown where the curves correspond to the Gaussian fit (3.14).

### 3.6.2 Results of the Analysis

Similarly to fig. 3.12a, the BE correlation function for the data is shown in fig. 3.12b. A clear enhancement is observed at low $Q$ values ($\lambda > 0$), corresponding to the BE effect.

The experimental results of the two- and three-dimensional fits of the BE correlation function $R_2$, using (3.13–3.15), are presented in table 3.2, where the first error is statistical and the second error systematic. In all fits, the region $0 < Q_i < 1.04\,\mathrm{GeV}$ (for all $Q_i$) was taken as the fit range.

To estimate the systematic errors on the fit parameters, four different sources are examined.

- Firstly, we looked at the fit results obtained with the 6 possible MC mixing-correction combinations.

- Secondly, the influence of a different mixing sample was studied by not imposing the conditions that tracks are replaced by tracks with the same charge and coming from

Table 3.2: Values of the fit parameters for the two- and three-dimensional analyses. The first errors are statistical, the second errors systematic.

| parameter | 2 dim. Gaussian | 3 dim. Gaussian | 2 dim. Edgeworth | 3 dim. Edgeworth |
|---|---|---|---|---|
| $\lambda$ | $0.41 \pm 0.01^{+0.03}_{-0.18}$ | $0.41 \pm 0.01^{+0.02}_{-0.19}$ | $0.57 \pm 0.02^{+0.05}_{-0.26}$ | $0.54 \pm 0.02^{+0.04}_{-0.26}$ |
| $R_{\mathrm{L}}$ (fm) | $0.79 \pm 0.02^{+0.04}_{-0.05}$ | $0.74 \pm 0.02^{+0.04}_{-0.03}$ | $0.73 \pm 0.02 \pm 0.03$ | $0.69 \pm 0.02^{+0.04}_{-0.03}$ |
| $R_{\mathrm{out}}$ (fm) | - | $0.53 \pm 0.02^{+0.05}_{-0.06}$ | - | $0.44 \pm 0.02^{+0.05}_{-0.06}$ |
| $R_{\mathrm{side}}$ (fm) | - | $0.59 \pm 0.01^{+0.03}_{-0.13}$ | - | $0.56 \pm 0.02^{+0.03}_{-0.12}$ |
| $R_{\mathrm{T}}$ (fm) | $0.58 \pm 0.01^{+0.04}_{-0.09}$ | - | $0.56 \pm 0.02^{+0.04}_{-0.09}$ | - |
| $R_{\mathrm{out}}/R_{\mathrm{L}}$ | - | $0.71 \pm 0.02^{+0.05}_{-0.08}$ | - | $0.65 \pm 0.03^{+0.06}_{-0.09}$ |
| $R_{\mathrm{side}}/R_{\mathrm{L}}$ | - | $0.80 \pm 0.02^{+0.03}_{-0.18}$ | - | $0.81 \pm 0.02^{+0.03}_{-0.19}$ |
| $R_{\mathrm{T}}/R_{\mathrm{L}}$ | $0.73 \pm 0.02^{+0.03}_{-0.10}$ | - | $0.77 \pm 0.02^{+0.04}_{-0.12}$ | - |
| $\kappa_{\mathrm{L}}$ | - | - | $0.4 \pm 0.1^{+0.1}_{-0.2}$ | $0.5 \pm 0.1^{+0.1}_{-0.2}$ |
| $\kappa_{\mathrm{out}}$ | - | - | - | $0.8 \pm 0.1 \pm 0.3$ |
| $\kappa_{\mathrm{side}}$ | - | - | - | $0.1 \pm 0.1 \pm 0.3$ |
| $\kappa_{\mathrm{T}}$ | - | - | $0.6 \pm 0.1^{+0.3}_{-0.2}$ | - |
| $\chi^2$/NDF | 761/670 | 2314/2189 | 675/668 | 2220/2186 |
| CL (%) | 0.8 | 3.1 | 41 | 30 |

events with approximately the same multiplicity.

- Thirdly, the systematic effects related to track and event selection were estimated by repeating the analysis with stronger and weaker selection criteria, resulting in approximately 11% fewer/more events or 6% fewer/more tracks. Each cut presented in section 3.2 was varied within "reasonable" values keeping the other cuts on their standard values. The maximum deviation of the measurement obtained within this range is taken as the contribution to the systematic error of the measurement due to this cut.

- As a fourth systematic effect the influence of changing the fit range by ±160 MeV in all $Q_i$ is studied.

Tables 3.3 and 3.4 show the systematic uncertainties of the different sources for $\lambda$, $R_{\mathrm{L}}$, $R_{\mathrm{out}}$ and $R_{\mathrm{side}}$, for the Gaussian parametrization and the lowest-order Edgeworth expansion of the Gaussian, respectively. To obtain a total systematic error, the errors from the four sources are added in quadrature. The dominant contribution to the systematic error on $\lambda$ and the transverse radii is from the 6 possible MC combinations to determine the correction factors. For $\lambda$ this contribution is approximately 90%, for the radii $R_{\mathrm{out}}$ and $R_{\mathrm{side}}$ approximately 60% and 80%, respectively. This part of the error is also responsible for the asymmetry in the errors since our best choice of reference-correction combination does not coincide with the average. In particular, all other combinations result in smaller values of $R_{\mathrm{side}}/R_{\mathrm{L}}$. For $R_{\mathrm{L}}$ the errors from all the sources are approximately equal.

The cross term in (3.13) turns out to be zero within errors ($R^2_{\mathrm{L,out}} = -0.1 \pm 0.6$ GeV$^{-2}$) and the results given in table 3.2 correspond to a fit with the cross term fixed to zero. The values are obtained using JETSET without BE for the mixing correction and JETSET with BE for the detector correction, since the latter model is found to be the most successful in reproducing the L3 data in the relevant variables (see fig. 3.8) and this choice gives the lowest $\chi^2$ in the fits. In particular, the $Q$ distribution is underestimated by the MC without BEC (JETSET or HERWIG) up to 20% at low $Q$. Taking a specific component $Q_i$ and integrating over the other components, gives an underestimation up to 5% at low $Q_i$. Furthermore, when other MC combinations are used for the mixing and detector correction, the $\chi^2$ value typically increases by 1–3%, leading to a reduction of the confidence level (CL) of typically a factor two.

From table 3.2 it is clear that BEC exist ($\lambda > 0$). Furthermore, since $R_{\text{side}}/R_{\text{L}} < 1$ (an effect of more than 5 standard deviations) an elongation of the region of homogeneity of pion emission along the thrust axis is established. Since the difference between the two transverse radii is small compared to that between the longitudinal component and either of the transverse components, the two-dimensional analysis, where we can use 40 instead of 80 MeV intervals, serves as a good cross-check. As expected, the two- and three-dimensional analyses give the same values for $\lambda$ and $R_{\text{L}}$ (within errors), and the value of $R_{\text{T}}$ lies between those of $R_{\text{out}}$ and $R_{\text{side}}$.

To study the behaviour of each of the components of $Q$, projections of the three-dimensional BE correlation function $R_2$, eqn. (3.11), onto the three axes are shown in fig. 3.13, using regions $Q_i < 240$ MeV (i.e., the first three bins) of the non-projected components. The dashed curves correspond to the Gaussian fit results described above. Similarly,

Table 3.3: Contribution to the systematic error of $\lambda$, $R_{\text{L}}$, $R_{\text{out}}$ and $R_{\text{side}}$, according to the Gaussian parametrization. Explanation of the sources are in the text.

| source | $\lambda$ | $R_{\text{L}}$ (fm) | $R_{\text{out}}$ (fm) | $R_{\text{side}}$ (fm) |
|---|---|---|---|---|
| MC corrections | $^{+0.011}_{-0.182}$ | $^{+0.020}_{-0.014}$ | $^{+0.027}_{-0.042}$ | $^{+0.017}_{-0.122}$ |
| different mixing | 0.018 | 0.018 | 0.017 | 0.016 |
| track and event selection | 0.013 | 0.020 | 0.022 | 0.024 |
| fit range | 0.005 | 0.015 | 0.016 | 0.011 |
| total | $^{+0.02}_{-0.19}$ | $^{+0.04}_{-0.03}$ | $^{+0.05}_{-0.06}$ | $^{+0.03}_{-0.13}$ |

Table 3.4: Contribution to the systematic error of $\lambda$, $R_{\text{L}}$, $R_{\text{out}}$ and $R_{\text{side}}$, according to the lowest-order Edgeworth expansion of the Gaussian parametrization. Explanation of the sources are in the text.

| source | $\lambda$ | $R_{\text{L}}$ (fm) | $R_{\text{out}}$ (fm) | $R_{\text{side}}$ (fm) |
|---|---|---|---|---|
| MC corrections | $^{+0.017}_{-0.252}$ | $^{+0.023}_{-0.017}$ | $^{+0.037}_{-0.048}$ | $^{+0.018}_{-0.112}$ |
| different mixing | 0.020 | 0.014 | 0.012 | 0.015 |
| track and event selection | 0.034 | 0.019 | 0.021 | 0.022 |
| fit range | 0.014 | 0.015 | 0.022 | 0.014 |
| total | $^{+0.04}_{-0.26}$ | $^{+0.04}_{-0.03}$ | $^{+0.05}_{-0.06}$ | $^{+0.03}_{-0.12}$ |

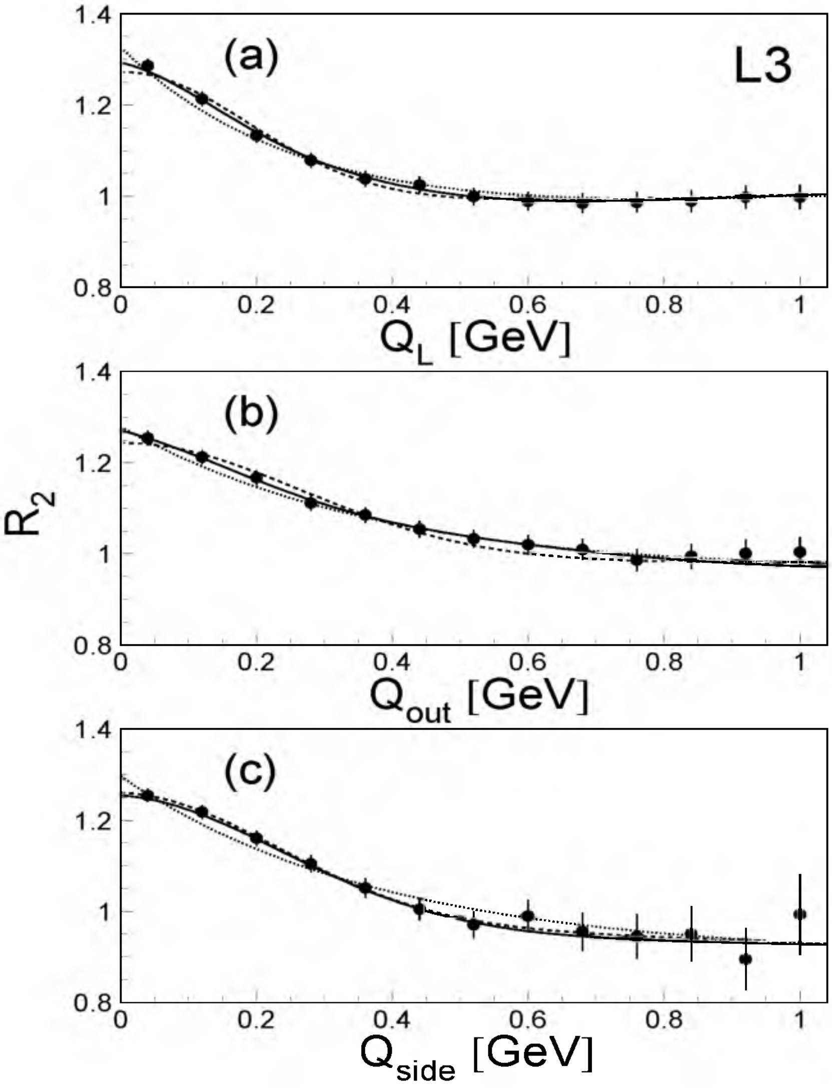

Figure 3.13: Projections of $R_2$ onto the three axes $Q_{\mathrm{L}}$, $Q_{\mathrm{out}}$ and $Q_{\mathrm{side}}$ using regions up to 240 MeV of the non-projected components. The mixing correction is determined using JETSET without BE and the detector correction using JETSET with BE. The full lines correspond to projections of the fit with the lowest-order Edgeworth expansion, the dashed lines correspond to those of the Gaussian fit and the dotted lines to the exponential fit.

a projection of $R_2$ onto the $Q_{\mathrm{L}} - Q_{\mathrm{side}}$ plane is shown in fig. 3.14.

From the value of $\chi^2$ (see table 3.2) it appears that the shape of the correlation function deviates from a Gaussian. An exponential function has often been suggested as an alternative to the Gaussian. The fits were, therefore, repeated with an exponential, $\exp(-\sum_i R_i Q_i)$, replacing the Gaussian in eqn. (3.13) with $R^2_{\mathrm{L,out}} = 0$ (dotted lines).

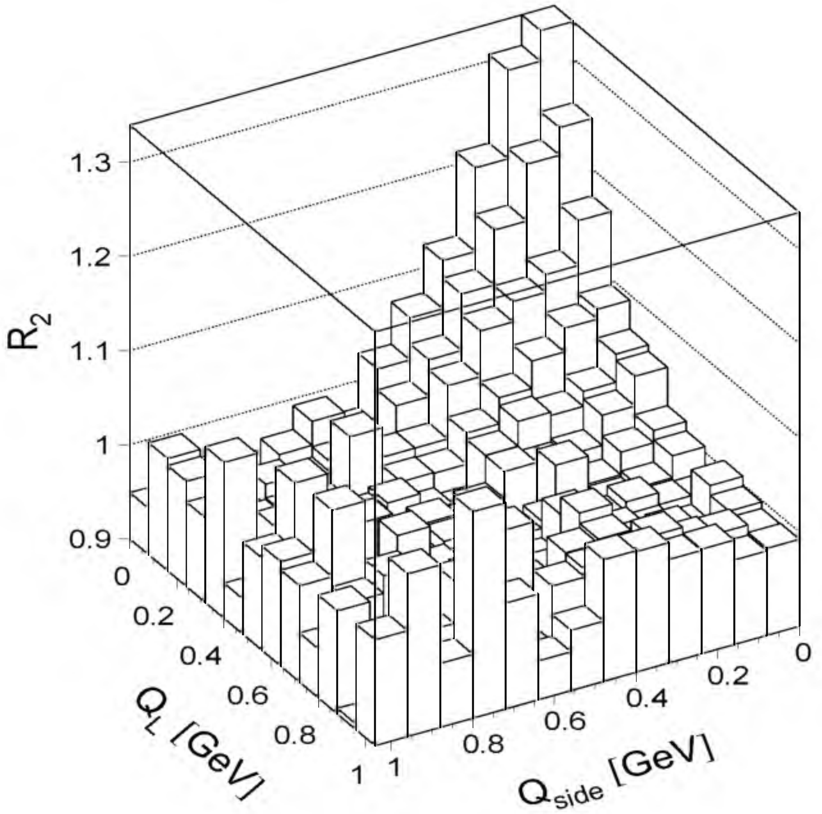

Figure 3.14: Projection of $R_2$ onto the $Q_{\mathrm{L}} - Q_{\mathrm{side}}$ plane using the region up to 240 MeV of $Q_{\mathrm{out}}$. The mixing correction is determined using JETSET without BE and the detector correction using JETSET with BE.

However, the overall $\chi^2$ increases by typically 2-4%, depending on the reference-correction combination used, while confirming the elongation observed from the Gaussian fit.

The fits were, furthermore, repeated with the lowest-order Edgeworth expansion of the Gaussian (see eqn. (3.15)), in order to study possible deviations from the Gaussian. The results of the fit are shown in the last two columns of table 3.2. The non-zero values of the $\kappa$ parameters indicate the deviation from a Gaussian. The value of $\lambda$ is larger than that of the corresponding Gaussian $\lambda$ and the values of the radii confirm the elongation observed from the Gaussian fit. The value of $\chi^2$/NDF and the CL indicate a better fit than the Gaussian one. In fig. 3.13 the fits corresponding to the lowest-order Edgeworth expansion are shown as full lines.

## 3.7 Comparison with Monte Carlo Generators

In this section, the results of the L3 data are compared with JETSET (with BE effects according to the $\mathrm{BE}_0$ and $\mathrm{BE}_{32}$ algorithms) generated samples and with predictions of other MC generators.

For comparison with the results of the L3 data, fits were performed on a JETSET generated sample taking $R_2$ as

$$R_{2,\,\mathrm{JETSET}} = (N/N_{\mathrm{mix}})_{\mathrm{JETSET,\,with\,BE}} \,/\, (N/N_{\mathrm{mix}})_{\mathrm{JETSET,\,noBE}} \quad . \tag{3.17}$$

Table 3.5: Values of the fit parameters for the two- and three-dimensional analyses obtained from JETSET where the BE effects are simulated according to the $\mathrm{BE}_0$ model. The errors are statistical only.

| parameter | 2 dim. Gaussian | 3 dim. Gaussian | 2 dim. Edgeworth | 3 dim. Edgeworth |
|---|---|---|---|---|
| $\lambda$ | $0.45 \pm 0.01$ | $0.46 \pm 0.01$ | $0.59 \pm 0.02$ | $0.59 \pm 0.02$ |
| $R_{\mathrm{L}}$ (fm) | $0.74 \pm 0.01$ | $0.71 \pm 0.01$ | $0.70 \pm 0.02$ | $0.66 \pm 0.02$ |
| $R_{\mathrm{out}}$ (fm) | - | $0.58 \pm 0.01$ | - | $0.52 \pm 0.02$ |
| $R_{\mathrm{side}}$ (fm) | - | $0.75 \pm 0.01$ | - | $0.72 \pm 0.02$ |
| $R_{\mathrm{T}}$ (fm) | $0.68 \pm 0.01$ | - | $0.68 \pm 0.01$ | - |
| $R_{\mathrm{out}}/R_{\mathrm{L}}$ | - | $0.82 \pm 0.02$ | - | $0.79 \pm 0.02$ |
| $R_{\mathrm{side}}/R_{\mathrm{L}}$ | - | $1.06 \pm 0.02$ | - | $1.08 \pm 0.03$ |
| $R_{\mathrm{T}}/R_{\mathrm{L}}$ | $0.92 \pm 0.02$ | - | $0.97 \pm 0.02$ | - |
| $\kappa_{\mathrm{L}}$ | - | - | $0.4 \pm 0.1$ | $0.5 \pm 0.1$ |
| $\kappa_{\mathrm{out}}$ | - | - | - | $0.6 \pm 0.1$ |
| $\kappa_{\mathrm{side}}$ | - | - | - | $0.2 \pm 0.1$ |
| $\kappa_{\mathrm{T}}$ | - | - | $0.5 \pm 0.1$ | - |
| $\chi^2$/NDF | 846/670 | 2435/2189 | 736/668 | 2290/2186 |
| CL (%) | $4.1 \cdot 10^{-4}$ | $1.6 \cdot 10^{-2}$ | 3.4 | 6.0 |

Using $\mathrm{BE}_0$, results in a value of $R_{\mathrm{side}}$ that is larger than in the data (see table 3.5). In particular, $R_{\mathrm{side}}/R_{\mathrm{L}} = 1.06 \pm 0.02(\mathrm{stat})$ for the Gaussian fit and $1.08 \pm 0.03(\mathrm{stat})$ for the Edgeworth expansion. So, JETSET fails to reproduce the data, which can be expected since it treats the region of homogeneity as spherical. When the $\mathrm{BE}_{32}$ scenario is used, similar results are obtained. In particular, $R_{\mathrm{side}}/R_{\mathrm{L}} = 1.04 \pm 0.02(\mathrm{stat})$ (CL$=8.1 \cdot 10^{-3}$%) for the Gaussian fit and $1.01 \pm 0.03(\mathrm{stat})$ (CL=5.1%) for the Edgeworth expansion. The reason for the low CLs for any of the JETSET samples is due to the high statistics with respect to the data. Note that the input BE parameters in JETSET are not the same as the output: $\lambda$ and $R$ have changed and the Edgeworth expansion fits better than the Gaussian. This is a known feature, as shown in [67].

Another MC generator with BE simulation is VNI [68], a cluster hadronization model, based on a space-time description of the perturbative development of parton showers, combined with a non-perturbative model for cluster formation and hadronization. In its present form this model predicts $R_{\mathrm{side}} \approx R_{\mathrm{L}}$ [68], again in contradiction to the L3 results.

The measurement also implies that the spherical weighting function of [42, 69] is too simple an assumption.

The observation of an elongation is theoretically expected in string models [38, 54, 60], however, as a consequence of a longitudinal stretching of the string field.

## 3.8 Comparison with other LEP experiments

The main conclusion of the multi-dimensional BE analyses is that the longitudinal radius is found to be significantly larger than the transverse radius. Using the Gaussian parametrization (3.13) leads to $R_{\mathrm{side}}/R_{\mathrm{L}} = 0.80 \pm 0.02^{+0.03}_{-0.18}$. The Edgeworth expansion of the Gaussian (3.15) gives $R_{\mathrm{side}}/R_{\mathrm{L}} = 0.81 \pm 0.02^{+0.03}_{-0.19}$.

The LEP collaborations OPAL and DELPHI have also done a multi-dimensional BE analysis. The results are in qualitative agreement with the result of L3. The result of the OPAL analysis, which uses unlike-sign particle pairs to compute the reference sample and which restricts the analysis to two-jet events, is $R_{\mathrm{side}}/R_{\mathrm{L}} = 0.82 \pm 0.02^{+0.01}_{-0.05}$ [52] (based on a Gaussian parametrization). The DELPHI collaboration has performed a two-dimensional analysis. Taking only events with a two-jet topology, this experiment obtained $R_{\mathrm{T}}/R_{\mathrm{L}} = 0.62 \pm 0.02 \pm 0.05$ [53], in fair agreement with the L3 result of $R_{\mathrm{T}}/R_{\mathrm{L}} = 0.73 \pm 0.02^{+0.03}_{-0.10}$.

Thus, analogous measurements done by other LEP experiments have in the mean time confirmed the elongation of the region of homogeneity of pion emission along the thrust axis.

# Chapter 4

# Bose-Einstein Correlations in WW Events

This chapter deals with a study concerning Bose-Einstein correlations (BEC) between bosons coming from W-pair production. In particular, attention is paid to the possible existence of these correlations between bosons originating from different W's in the process $e^+e^- \rightarrow W^+W^- \rightarrow$ hadrons. Existence of these inter-W BEC would imply a non-independent fragmentation of the two W's and influence the W mass measurement in this process. That fact indicates the relevance of this study, since a precise measurement of the W mass is one of the main goals of LEP.

The following subjects are treated in this chapter. Firstly, the relevance of the analysis is explored in more detail. Then, attention is paid to W-pair production at LEP and its decay channels. The mathematical tools to study BEC and in particular inter-W BEC, are given in section 3 and the data that are used, including their selection, in section 4. This is followed by the results of the measurement of the BE correlation function for WW events. Since the measurements in this chapter are delicate, special attention is paid to bin-to-bin correlations, which give a non-negligible contribution to the statistical errors. Also the systematic uncertainties are treated. A comparison of the BE correlation function is made with that observed in hadronic Z decay events with and without the contribution of $Z \rightarrow b\bar{b}$ decays. Therefore, a b-tagging procedure is explained in a separate subsection. In the section following that, results are shown of a direct measurement of inter-W BEC, in which special attention is paid to a mixing procedure to construct a reference sample free from inter-W BEC, and to bin-to-bin correlations which considerably influence the significance of the result. Also the systematic uncertainties are given and comparisons are made with MC predictions. A special section is devoted to analyses that may result in higher sensitivity when it comes to the measurement of inter-W BEC. The chapter ends with a summary of the conclusions, a comparison with the results of the other LEP experiments and a discussion about the interpretation of the results.

This chapter is a more detailed description and an extension of [70–72].

## 4.1 Relevance of the Analysis

From the previous chapter we conclude that Bose-Einstein interference is observed in hadronic Z decay as an enhanced production of identical bosons at small four-momentum difference. There is no reason why such an interference should not be present within hadronic W-decay (intra-W BE interference), as well. Furthermore, since in fully hadronic WW events ($W^+W^- \to q_1\bar{q}_2q_3\bar{q}_4$) the W-decay products overlap in space-time at LEP2 energies, it may be natural to expect [23,25–29] interference also between identical bosons originating from different W's (inter-W BE interference). The overlap may be large, since the experimentally observed radius of the pion emission region is of order 1 fm (see previous chapter), about an order of magnitude larger than the distance between the $W^+W^-$ decay vertices at LEP2 energies. The distance $d_{WW}$ between the $W^+W^-$ decay vertices can be estimated by

$$d_{WW} = 2\gamma\beta\tau_W \quad , \tag{4.1}$$

where $\gamma$ is the Lorentz factor, $\beta$ the velocity of the W and $\tau_W$ the lifetime of the W. E.g., taking $\sqrt{s} = 189\,\mathrm{GeV}$, the energy of each W equal to $\frac{1}{2}\sqrt{s}$, the W mass $M_W = 80.5\,\mathrm{GeV}$ and $\tau_W = 0.5\,\mathrm{GeV}^{-1}$, results in $d_{WW} = 0.12$ fm.

Together with colour reconnection [30,73–77], inter-W BE interference forms a potential bias in the determination of the W mass. Due to the poor understanding of BEC, in particular inter-W BEC, a large systematic error is attributed to the W mass measurement in the fully hadronic channel. E.g., the preliminary result of the systematic error from BEC on the W mass measurement in the fully hadronic channel, quoted by LEP at the International Europhysics Conference on High Energy Physics in Budapest, Hungary, in 2001, is 25 MeV [78]. Furthermore, the four LEP experiments give different estimates for this error, ranging from 20 to 67 MeV [78]. Realizing that the total systematic error quoted by LEP in the fully hadronic channel is 54 MeV, almost twice the statistical error, the necessity of studying (inter-W) BEC is obvious.

One of the main reasons for LEP to measure the W mass with great accuracy is that it sets limits on the mass of the yet unobserved Higgs boson, which accounts for the mass generation in the Standard Model [79]. In particular, the Fermi constant, $G_\mu$, can be expressed as

$$G_\mu = \frac{\alpha\pi}{\sqrt{2}M_W^2\left(1-\frac{M_W^2}{M_Z^2}\right)} \cdot \frac{1}{1-\Delta r} \quad , \tag{4.2}$$

where $\alpha$ is the fine-structure constant, $M_Z$ is the mass of the Z boson and $\Delta r$ includes the radiative corrections, which depend on the mass of the top quark and the mass of the Higgs boson. Since $G_\mu$, $M_Z$ and $\alpha$ are known to a high precision, a better knowledge of $M_W$ tightens the limits on the Higgs boson mass.

Besides the impact that inter-W BEC may have on the measurement of the W mass, they also provide a laboratory to measure the space-time development of the overlap between the two pion-emission regions in hadronic $W^+W^-$ decays, as we understand from chapters 1 and 3. Therefore, they play an important role in understanding the physics of QCD interference phenomena in a sector where perturbative methods are not applicable.

Recent model predictions [23, 25–31] are still contradictory when it comes to the existence of inter-W BEC and to what extent they influence the W mass measurement.

## 4.2 W-Pair Production at LEP

Since the end of 1995, LEP has moved on from the Z ($\sqrt{s} \simeq 91.2\,\text{GeV}$) and entered its second phase. This second phase consisted in doubling its energy, one of the main purposes being the production of W-pairs. Apart from the Higgs, this allows the completion of the study of electroweak interactions, and in particular of the massive gauge bosons which, together with the photon, mediate such forces.

The process $e^+e^- \to W^+W^-$ gets contributions from three tree-level Feynman diagrams (see fig. 4.1): the Z or $\gamma$ $s$-channel diagrams and the $t$-channel neutrino exchange diagram.

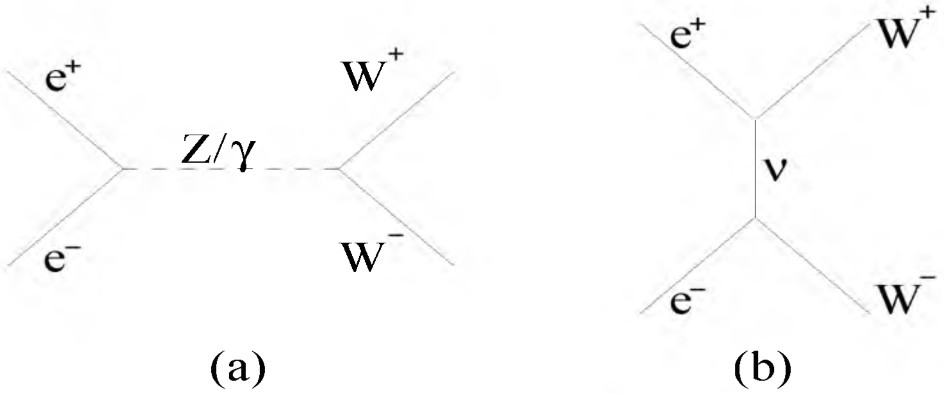

Figure 4.1: Lowest-order Feynman diagrams for $e^+e^- \to W^+W^-$: via mediation of a Z boson or a photon, (a), or via electron-neutrino exchange, (b).

The experimental signature of the production of a W-pair is a four-fermion final-state. The W can decay into either a charged lepton (e, $\mu$ or $\tau$) and its corresponding antineutrino (or their anti-matter equivalents), or a quark and an antiquark. For convenience, a leptonically decaying W is expressed as $W \to \ell\bar{\nu}_\ell$, i.e., the decay channels $W^+ \to \bar{\ell}\nu_\ell$ and $W^- \to \ell\bar{\nu}_\ell$ are combined in this notation. The Standard Model predicts the branching ratios to be 67.51% for the hadronic channel and 10.83% for each of the leptonic channels, in the approximation of massless final-state fermions. The W-pair final-states are usually classified into the following three categories:

- **fully hadronic**: both W's decay into a quark and an antiquark ($W^+W^- \to q_1\bar{q}_2q_3\bar{q}_4$),
- **semi-hadronic**: one W decays hadronically and one W decays into a lepton and its corresponding (anti-)neutrino ($W^+W^- \to q_1\bar{q}_2\ell\bar{\nu}_\ell$),

- **fully leptonic**: both W's decay into a (anti-)lepton and a (anti-)neutrino ($W^+W^- \to \ell\nu_\ell\ell'\bar{\nu}_{\ell'}$).

Since in this work we concentrate on BEC, we are only interested in the fully hadronic WW events and in the hadronically decaying part of the semi-hadronic WW events.

Experimentally, measuring a W-pair at LEP2 is a much more difficult task than measuring a Z at its resonance (LEP1): the cross section at the Z resonance is about 2000 times larger than the cross section for the production of W-pairs at its maximum. This means that the statistics are much smaller and the background higher than in the case of the Z. Extra difficulties occur by the existence of several sources of irreducible background events, as $e^+e^- \to Z/\gamma \to q\bar{q}(\gamma)$ events for the fully- and semi-hadronic WW channels. More about the WW selection efficiency and purity can be found in section 4.4.

To obtain WW event samples, fully hadronic or semi-hadronic, the final-state fermions, i.e., electrons, muons, $\tau$-jets (corresponding to the visible $\tau$-decay products) and the hadronic jets, corresponding to quarks, are reconstructed and subjected to selection criteria (see section 4.4). Two reconstructed and selected WW event candidates, as seen by the L3 detector at $\sqrt{s} \simeq 189\,\text{GeV}$, are shown in fig. 4.2. Fig. 4.2a shows an event with a four-jet topology, characteristic for fully hadronic WW events, projected onto the plane transverse to the beam axis ($x-y$ plane). In fig. 4.2b a $W^+W^- \to q_1\bar{q}_2e^-\bar{\nu}_e$ candidate is shown, in a plane containing the beam axis ($y-z$ plane). The two jets, associated with

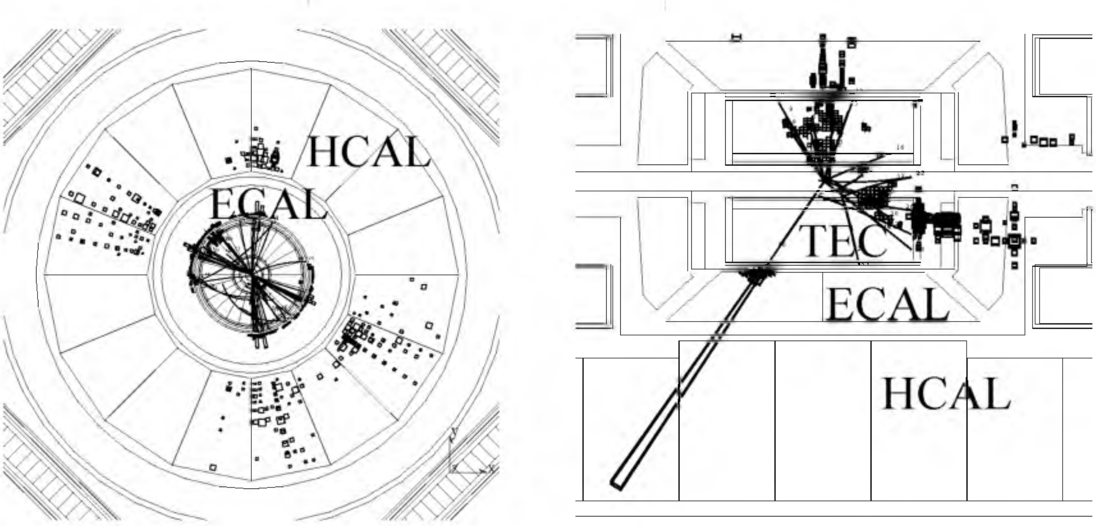

(a) (b)

Figure 4.2: Two WW event candidates as seen in the L3 detector. A $W^+W^- \to q_1\bar{q}_2q_3\bar{q}_4$ candidate as seen in the $x-y$ plane, (a); a $W^+W^- \to q_1\bar{q}_2e^-\bar{\nu}_e$ candidate as seen in the $y-z$ plane, (b). Several subdetectors are also indicated. Lines correspond to tracks in the TEC, squares or rectangles outside the TEC to energy deposits in the ECAL or HCAL. The size of the squares or rectangles is proportional to the energy deposited.

the hadronically decaying W, can be observed, and also a high-energetic electron can be identified by the large energy deposit in the ECAL matching a charged track, indicated in the lower left of the figure. The neutrino cannot be seen, since it does not interact with any detector material. Indirectly, the neutrino is observed by missing momentum. Lines in fig. 4.2 correspond to tracks in the TEC, and the squares or rectangles outside the TEC correspond to the energy deposited in the ECAL or HCAL.

## 4.3 Method of Analysis

Bose-Einstein correlations between two particles with four-momenta $p_1$ and $p_2$ are described by the ratio of the two-particle number densities, $\rho_2(p_1, p_2)$ and $\rho_{0,2}(p_1, p_2)$, the latter being the density that would occur in a world without BEC, resulting in the BE correlation function

$$R_2(p_1, p_2) = \frac{\rho_2(p_1, p_2)}{\rho_{0,2}(p_1, p_2)} \quad . \tag{4.3}$$

Since BEC are largest at small four-momentum difference, $Q$, $R_2$ is parametrized in this one-dimensional distance measure. While this is an oversimplification, as we have seen in the previous chapter, lack of statistics prevents a multi-dimensional analysis here. Therefore, the two-particle density is defined here as (see also eqn. (1.11)):

$$\rho_2(Q) = \frac{1}{N_{\text{ev}}} \frac{\mathrm{d}n_{\text{pairs}}}{\mathrm{d}Q} \quad , \tag{4.4}$$

where $N_{\text{ev}}$ is the number of selected events and $n_{\text{pairs}}$ the number of like-sign charged particle pairs in the $N_{\text{ev}}$ events.

The BE correlation function for WW events is determined for like-sign charged pion pairs using two choices of reference sample, i.e., the sample from which $\rho_{0,2}$ is determined. In the following, $(\pm, \pm)$ will indicate like-sign pairs and $(+, -)$ unlike-sign pairs. Lack of statistics prevents us from constructing a reference sample by mixing particles from different events according to the procedure given in subsection 3.4.1. Replacing tracks in an event by tracks with the same charge from other events with approximately the same multiplicity, such that none of the tracks is coming from the same event, demands a sample of events larger than is available in this analysis. Therefore, the first choice uses a MC model without BEC:

$$\rho_{0,2}(\pm, \pm) = \rho_2(\pm, \pm)_{\text{MC, noBE}} \quad . \tag{4.5}$$

The second choice uses unlike-sign particle pairs from the experimental events. A major drawback of this method is that the correlation function is affected by the presence of dynamical correlations, such as the decay of resonances. To compensate for this, the density for unlike-sign pairs is multiplied by the ratio of the densities for like- and unlike-sign pairs determined from a MC model without BEC:

$$\rho_{0,2}(\pm, \pm) = \rho_2(+, -) \cdot \left[\frac{\rho_2(\pm, \pm)}{\rho_2(+, -)}\right]_{\text{MC, noBE}} \quad . \tag{4.6}$$

In both cases, the correlation function, $R_2$, needs to be corrected for detector resolution, acceptance, efficiency and for particle misidentification. For this purpose, a multiplicative factor derived from MC studies is used, as in subsection 3.4.2. Since no explicit hadron identification is performed, this factor is given by the ratio of $\rho_2(\pm,\pm)$ and $\rho_2(\pm,\pm)/\rho_2(+,-)$, respectively, found from MC, for *pions* at generator level to that found using *all particles* after full detector simulation, reconstruction and selection. Thus, using (4.5) and (4.6) leads, respectively, to

$$R_2 = \left[\frac{\rho_2(\pm,\pm)_{\mathrm{data}}}{\rho_2(\pm,\pm)_{\mathrm{MC,\,noBE}}}\right] \cdot \left[\frac{\rho_2(\pm,\pm)_{\mathrm{gen}}}{\rho_2(\pm,\pm)_{\mathrm{det}}}\right]_{\mathrm{MC}} \tag{4.7}$$

and

$$R_2 = \left[\frac{\rho_2(\pm,\pm)}{\rho_2(+,-)}\right]_{\mathrm{data}} \cdot \left[\frac{\rho_2(+,-)}{\rho_2(\pm,\pm)}\right]_{\mathrm{MC,\,noBE}} \cdot \left[\frac{\rho_2(\pm,\pm)_{\mathrm{gen}}}{\rho_2(\pm,\pm)_{\mathrm{det}}} \cdot \frac{\rho_2(+,-)_{\mathrm{det}}}{\rho_2(+,-)_{\mathrm{gen}}}\right]_{\mathrm{MC}} \quad . \tag{4.8}$$

A dilution of the BE effect in the fully hadronic channel with respect to the semi-hadronic channel can be expected when inter-W BEC are absent. In particular, assuming that there is no stochastic dependence between the W's, one can write [24]

$$C_2^{\mathrm{WW}}(p_1,p_2) = C_2^{\mathrm{W}^+}(p_1,p_2) + C_2^{\mathrm{W}^-}(p_1,p_2) \quad , \tag{4.9}$$

and

$$\rho_2^{\mathrm{WW}}(p_1,p_2) = \rho_2^{\mathrm{W}^+}(p_1,p_2) + \rho_2^{\mathrm{W}^-}(p_1,p_2) + \rho_1^{\mathrm{W}^+}(p_1)\rho_1^{\mathrm{W}^-}(p_2) + \rho_1^{\mathrm{W}^+}(p_2)\rho_1^{\mathrm{W}^-}(p_1) \quad , \tag{4.10}$$

where the superscript WW indicates that both W's decay hadronically and the superscript $\mathrm{W}^\pm$ indicates that only $\mathrm{W}^\pm$ decays hadronically. The cumulant correlation function $C_2$ is defined as $C_2(p_1,p_2) \equiv \rho_2(p_1,p_2) - \rho_1(p_1)\rho_1(p_2)$. Since we are only interested in BEC, the product of the two single-particle densities is replaced by $\rho_{0,2}$, the two-particle density that would occur in the absence of BE interference. A derivation of eqns. (4.9) and (4.10) by means of generating functionals is given in appendix A. Assuming that the densities for $\mathrm{W}^+$ and $\mathrm{W}^-$ are the same, (4.10) becomes

$$\rho_2^{\mathrm{WW}}(p_1,p_2) = 2\rho_2^{\mathrm{W}}(p_1,p_2) + 2\rho_1^{\mathrm{W}}(p_1)\rho_1^{\mathrm{W}}(p_2) \quad . \tag{4.11}$$

The terms $\rho_2^{\mathrm{WW}}$ and $\rho_2^{\mathrm{W}}$ of (4.11) are measured in the fully hadronic and the semi-hadronic WW events, respectively. To measure the product of the single particle densities, a two-particle density $\rho_{\mathrm{mix}}^{\mathrm{W}^+\mathrm{W}^-}(p_1,p_2)$ is used, obtained by pairing particles originating from two *different* semi-hadronic WW events, since by construction particles in these pairs are uncorrelated. The mixing procedure is explained in detail in subsection 4.7.1.

Since the two-particle densities are measured as a function of $Q$, one can write the BE correlation function for fully hadronic WW events, assuming that there is no stochastic dependence between the two W's, as

$$R_2^{\mathrm{WW}}(Q) = \frac{\rho_2^{\mathrm{WW}}(Q)}{\rho_{0,2}^{\mathrm{WW}}(Q)} = \frac{2\rho_2^{\mathrm{W}}(Q) + 2\rho_{\mathrm{mix}}^{\mathrm{W}^+\mathrm{W}^-}(Q)}{2\rho_{0,2}^{\mathrm{W}}(Q) + 2\rho_{\mathrm{mix}}^{\mathrm{W}^+\mathrm{W}^-}(Q)} = 1 + (1 - F(Q))(R_2^{\mathrm{W}}(Q) - 1) \quad , \tag{4.12}$$

where

$$F(Q) \equiv \frac{2\rho_{\mathrm{mix}}^{\mathrm{W^+W^-}}(Q)}{\rho_{0,2}^{\mathrm{WW}}(Q)} \quad , \tag{4.13}$$

is the fraction of pairs with one particle coming from $\mathrm{W}^+$ and the other from $\mathrm{W}^-$ in fully hadronic WW events that would occur in a world without BEC. In eqn. (4.12) the assumption is made that $\rho_{\mathrm{mix}}^{\mathrm{W^+W^-}}$ is the same for a sample with intra-W BEC (but no inter-W BEC) and a sample without BEC. From a MC point of view, this assumption is found to be valid. $R_2^{\mathrm{W}}$ is the BE correlation function for the hadronically decaying part of semi-hadronic WW events. $F(Q)$ will be estimated in subsection 4.6.2. To get some insight into eqn. (4.12), let us consider two special cases:

- **Fully overlapping *Q*-spectra**: When the $Q$-spectrum for fully hadronic WW events is the same as for the hadronically decaying part of semi-hadronic WW events, one would have $F(Q) = \frac{1}{2}$ (since $\rho_{0,2}^{\mathrm{W}}(Q) = \rho_{\mathrm{mix}}^{\mathrm{W^+W^-}}(Q)$), and thus

  $$R_2^{\mathrm{WW}}(Q) = 1 + \frac{1}{2}(R_2^{\mathrm{W}}(Q) - 1) \quad . \tag{4.14}$$

  In this case, the normalized cumulant correlation function, $R_2 - 1$, for fully hadronic WW events is only half as strong as that within one hadronically decaying W. In general, for fully overlapping and independent sources, the dilution factor $F$, for genuine $q$-particle correlations is equal to $1/S^{q-1}$, where $S$ is the number of sources, which is 2 in this analysis when one assumes no cross-talk between the two W's, under the assumption that $S$ is much smaller than the multiplicity of the event.

- **Decreasingly overlapping *Q*-spectra**: when we are above the threshold of producing two W's, and increase $\sqrt{s}$, $F(Q)$ will decrease at low $Q$. No matter whether we deal with inter-W BEC or not, when $F(Q)$ tends to zero at low $Q$, we will observe:

  $$R_2^{\mathrm{WW}}(Q) = R_2^{\mathrm{W}}(Q) \quad . \tag{4.15}$$

From this, one concludes that the strength of the BEC in fully hadronic WW events must be in the range 0.5–1 times that of the BEC in semi-hadronic WW events, with the lower value corresponding to complete absence of BEC between particles of different W's and complete overlap.

For comparison to the actual WW data, the BE correlation function for fully hadronic WW events, $R_2^{\mathrm{WW}}$, is estimated for the case that inter-W BEC are absent. This is done by constructing the BE correlation function for light-quark Z decays, i.e., without the $\mathrm{Z} \rightarrow \mathrm{b\bar{b}}$ decays, since b quarks are greatly suppressed in W decays (at LEP2). Apart from this, one expects the hadronic W and Z decays to be similar. The BE effect is expected to be different in $\mathrm{Z} \rightarrow \mathrm{b\bar{b}}$ and light-quark Z decay events. Less correlations are expected between pions in $\mathrm{Z} \rightarrow \mathrm{b\bar{b}}$ events since B mesons (that mainly decay into pions) that are produced in these events travel some distance before they decay. Consequently, the distance between two pions produced in $\mathrm{b\bar{b}}$ events will on average be larger than in light-quark Z decay events, leading to less correlations. Therefore, a high statistics light-quark Z decay sample (i.e., without $\mathrm{b\bar{b}}$ decay) is analysed and compared with the correlation function of the semi-hadronic WW events. Under the assumption that both correlation functions are the same and that BEC exist only between bosons from the same W (BES), the BE correlation function in the fully hadronic channel can be estimated by

$$R_2^{\mathrm{WW}}(Q)_{\mathrm{BES}} = 1 + (1 - F(Q)) \cdot \left( R_2^{\mathrm{Z\to light\,quarks}}(Q) - 1 \right) \quad . \tag{4.16}$$

A comparison with the measured BE correlation function in this channel, will give insight into the presence or absence of inter-W BEC.

The hypothesis that the two W's decay independently can be tested using (4.11), directly [24]. In particular, the following test statistics are used in terms of $Q$

$$\Delta\rho(Q) = \rho_2^{\mathrm{WW}}(Q) - 2\rho_2^{\mathrm{W}}(Q) - 2\rho_{\mathrm{mix}}^{\mathrm{W^+W^-}}(Q) \tag{4.17}$$

and

$$D(Q) = \frac{\rho_2^{\mathrm{WW}}(Q)}{2\rho_2^{\mathrm{W}}(Q) + 2\rho_{\mathrm{mix}}^{\mathrm{W^+W^-}}(Q)} \quad . \tag{4.18}$$

The advantage of this method is that it gives access to the inter-W correlations directly from the experimental data. There is no need for normalization by a MC model at this stage.

It is, however, possible that the event mixing procedure introduces artificial distortions and that it does not fully account for some non-BE correlations or some detector effects. Such distortions would show up as a deviation of $\Delta\rho$ from zero or $D$ from unity for a MC model without inter-W BEC. To diminish the effect of such inadequacies, if present, the following double ratio can be used

$$D'(Q) = \frac{D(Q)_{\mathrm{data}}}{D(Q)_{\mathrm{MC,\,noBE}}} \quad , \tag{4.19}$$

where $D(Q)_{\mathrm{MC,\,noBE}}$ is derived from a MC sample with no BEC, or at least without inter-W BEC.

In the absence of inter-W correlations, $\Delta\rho = 0$ and $D = D' = 1$. To study BEC, these relations are examined for small values of $Q$, for like-sign particles. To judge the influence of other correlations on these quantities, they are also examined for unlike-sign pairs and in MC models.

## 4.4 The WW Data

The data used in this analysis were collected by the L3 detector from 1998 to 2000 and correspond to a total integrated luminosity of 627.3 $\mathrm{pb}^{-1}$ (which is 89% of the integrated luminosity collected by L3 at LEP2) at a centre-of-mass energy ranging from 189 GeV to 209 GeV, well beyond the threshold of producing W-pairs.

In this section, firstly, the event selection is shown. After the event selection, the track selection is given. Special attention is paid to the background processes in the selection of WW events.

### 4.4.1 Event Selection

To obtain the two $W^+W^-$ event samples, one fully hadronic ($q\bar{q}q\bar{q}$) and the other semi-hadronic ($q\bar{q}\ell\bar{\nu}$), the visible final-state fermions, i.e., electrons, muons, $\tau$ jets corresponding to the visible $\tau$-decay products and the hadronic jets corresponding to quarks, are reconstructed and the selection criteria as described in [80–82] are applied, with the additional requirement for the fully hadronic channel that the neural network output must be greater than 0.6 for the 1998 and 1999 data, or 0.8 for the 2000 data.

In short, the selection is as follows. For selecting $q\bar{q}q\bar{q}$ events, firstly, high multiplicity four-jet events with low missing energy are required. The main background processes in this pre-selection are $e^+e^- \rightarrow Z/\gamma \rightarrow q\bar{q}(\gamma)$ and $e^+e^- \rightarrow ZZ$. To reduce these background events, a neural network is trained, such that its output peaks at one for the signal and at zero for the background. The input to the network consists of ten event variables: minimal and maximal jet energy, the energy difference between the two remaining jets, the minimal number of particles in a jet identified with the calorimeter, the logarithm of the Durham jet-resolution parameter $y_{34}$ [83] at which the event changes from a four-jet to a three-jet topology, the spherocity [84], the sum of the cosines of the jet-jet angles, the probability of the kinematic fit and the jet broadening of the most and least energetic jets. The jet broadening is defined as $\sum \sqrt{p_t} / \sum \sqrt{p}$, where the sum is over the particles belonging to the jet, $p_t$ is the transverse momentum relative to the reconstructed jet axis and $p$ is the momentum of the particle. By requiring the output of the network to be greater than 0.6, the purity of the selection is enhanced from roughly 50% to 80%, whereas the efficiency only decreases from roughly 94% to 86%. The numbers that are quoted here change a bit with the centre-of-mass energy. For selecting a $q\bar{q}\ell\bar{\nu}$ event, an identified isolated high energy lepton, two hadronic jets with high multiplicity and missing momentum due to one or more neutrinos, is required. The direction of the missing momentum has to be outside the beam pipe. The $\tau$ jet corresponding to the visible $\tau$-decay products, is identified as a low energy electron or muon, or a low multiplicity narrow jet, isolated from the rest of the event. In order to separate $q\bar{q}\mu\bar{\nu}$ and $q\bar{q}e\bar{\nu}$ events from $q\bar{q}\tau\bar{\nu}$ events for the case that the $\tau$ decays leptonically, the effective mass of the lepton-neutrino system is used. The background contamination in the $q\bar{q}\ell\bar{\nu}$ event selection is dominated by $e^+e^- \rightarrow Z/\gamma \rightarrow q\bar{q}(\gamma)$ events.

Since the centre-of-mass energy of LEP changed over the last three years, and even within each of those years, the analysis in this chapter is performed in different energy bins. In table 4.1, the energy bin (the quoted value is the rounded value of the average centre-of-mass energy in this bin), the average centre-of-mass energy in each energy bin, the integrated luminosity and the number of WW events selected in each channel, are given.

Table 4.1: The energy bin, the average centre-of-mass energy in each energy bin, on which LEP was operating from 1998 to 2000, its corresponding integrated luminosity and the number of selected WW events per channel.

| year | 1998 | 1999 | | | | 2000 | | |
|---|---|---|---|---|---|---|---|---|
| energy bin, GeV | 189 | 192 | 196 | 200 | 202 | 205 | 207 | 208 |
| $\langle\sqrt{s}\rangle$, GeV | 188.6 | 191.6 | 195.5 | 199.5 | 201.8 | 205.0 | 206.5 | 208.0 |
| $\int\mathcal{L}$, $\mathrm{pb}^{-1}$ | 176.8 | 29.7 | 83.7 | 82.8 | 37.0 | 78.9 | 130.1 | 8.3 |
| # $\mathrm{q\bar{q}q\bar{q}}$ events | 1431 | 229 | 635 | 699 | 298 | 683 | 1144 | 72 |
| # $\mathrm{q\bar{q}e\bar{\nu}}$ events | 349 | 76 | 179 | 157 | 73 | 185 | 291 | 15 |
| # $\mathrm{q\bar{q}\mu\bar{\nu}}$ events | 363 | 57 | 144 | 139 | 76 | 152 | 253 | 23 |
| # $\mathrm{q\bar{q}\tau\bar{\nu}}$ events | 313 | 55 | 194 | 156 | 64 | 167 | 294 | 20 |

The event generator KORALW [85] is used to simulate the signal processes. Within KORALW, BEC are simulated using the $\mathrm{BE}_{32}$ or $\mathrm{BE}_0$ algorithms [31]. Note that within the L3 collaboration, the WW MC models are generated, simulated, fully reconstructed and tuned to the L3 Z-decay data, with these two algorithms only. For most comparisons, $\mathrm{BE}_{32}$ is used, since we find the $Q$ distribution of unlike-sign particles to be less distorted by $\mathrm{BE}_{32}$ than by $\mathrm{BE}_0$ and therefore find it to agree better with the data than $\mathrm{BE}_0$, see subsection 4.7.2. Furthermore, the authors prefer this model to the $\mathrm{BE}_0$ model [31], since energy-momentum is better conserved in $\mathrm{BE}_{32}$. Where $\mathrm{BE}_0$ is used, it is explicitly stated. The BEC are implemented for *all* particles, which we refer to as BEA, or only for particles coming from the *same* W (intra-W BEC), which we refer to as BES. The background processes $\mathrm{e^+e^-} \to \mathrm{Z}/\gamma \to \mathrm{q\bar{q}}(\gamma)$, $\mathrm{e^+e^-} \to \mathrm{ZZ}$ and $\mathrm{e^+e^-} \to \mathrm{Ze^+e^-}$ (the last relevant only to the $\mathrm{q\bar{q}e\bar{\nu}}$ and $\mathrm{q\bar{q}\tau\bar{\nu}}$ channels) are generated using PYTHIA [37] with $\mathrm{BE}_0$. The generated events are passed through the L3 detector simulation program, reconstructed and subjected to the same WW selection criteria as the data.

MC studies using the above generators show that the selection efficiency for fully hadronic events changes by less than 0.5% when BEC (intra-W, or both intra-W and inter-W) are included or not. The efficiencies for the channels $\mathrm{q\bar{q}e\bar{\nu}}$, $\mathrm{q\bar{q}\mu\bar{\nu}}$, $\mathrm{q\bar{q}\tau\bar{\nu}}$ and $\mathrm{q\bar{q}q\bar{q}}$ are found to be around 83%, 75%, 50%, 86%, respectively. The fractions of background for these channels are around 5%, 5%, 15%, 20%, respectively. The percentages that are quoted here vary a few percent between the different energy bins. It is clear that the fully hadronic channel has the highest background. Most of the background (∼75%) originates from the process $\mathrm{e^+e^-} \to \mathrm{Z}/\gamma \to \mathrm{q\bar{q}}(\gamma)$, which has a relatively high cross section. Only a small fraction, $\mathcal{O}(1\%)$, of those events are selected as WW events. Therefore, it needs to be investigated whether the BEC in this sub-sample of $\mathrm{q\bar{q}}(\gamma)$ events describe the corresponding data set. This is done in subsection 4.4.3.

### 4.4.2 Track Selection

The BEC study in WW events is based on charged-particle information from the central tracker. The selection of charged tracks is the same as in the hadronic Z decay events at $\sqrt{s} \simeq 91.2\,\mathrm{GeV}$, see subsection 3.2.1. This means that tracks are required to have at least 40 (of 62 possible) hits, the span to be at least 50, the DCA to be less than 5 mm and the transverse momentum of a track greater than 100 MeV.

With this selection, reasonable agreement is obtained between the data and the MC simulation for the distributions of $Q$ and the difference in azimuthal, as well as polar angle with respect to the beam, for pairs of like-sign tracks, in both the fully hadronic and semi-hadronic channels. An example is shown in fig. 4.3, where the raw data collected at $\sqrt{s} \simeq 189\,\mathrm{GeV}$ are compared to simulated, reconstructed and selected KORALW with BES and background events. Similar agreement is observed when BEA is used. Note, that the distributions themselves vary slightly with energy since the W's are more and more boosted as $\sqrt{s}$ increases. Also, time-dependent detector effects exist. E.g., in 1999, there were periods when part of the TEC was malfunctioning, which influences the number of high quality tracks in those periods.

### 4.4.3 Bose-Einstein Correlations in $\mathrm{q\bar{q}}(\gamma)$ Background Events

In the data sample of fully- and semi-hadronic WW events, background events are taken into account by replacing $\rho_2(Q)$, eqn. (4.4), by

$$\rho_{2\,\mathrm{data-bg}} = \frac{1}{\mathcal{P}N_{\mathrm{ev}}}\left(\frac{\mathrm{d}n_{\mathrm{pairs}}}{\mathrm{d}Q} - \frac{\mathrm{d}n_{\mathrm{pairs,\,bg}}}{\mathrm{d}Q}\right) \quad , \tag{4.20}$$

where $\mathcal{P}$ is the purity of the selection and $n_{\mathrm{pairs,\,bg}}$ is the number of pairs of tracks corresponding to $(1-\mathcal{P})N_{\mathrm{ev}}$ background events.

In general, BEC in MC generated events are tuned, among other variables, to the inclusive $Q$ distribution. However, when we look at background processes in the selection of WW events, we only consider a small sub-sample of the generated events: the sample that pass the WW selection criteria. The question arises whether the BEC still describe the data in this particular sub-sample of events. If BEC in the background processes do not describe the corresponding data sets, we may under- or overestimate the two-particle density, (4.20), and thus under- or overestimate the BEC in WW events, in particular inter-W BEC.

Special attention is paid to the dominating background process $\mathrm{e^+e^-} \to \mathrm{Z}/\gamma \to \mathrm{q\bar{q}}(\gamma)$, present in the fully hadronic channel. The sub-sample of $\mathrm{q\bar{q}}(\gamma)$ events that pass the selection of fully hadronic WW events contains four-jet events, presumably from multiple gluon radiation. To test whether BEC in these $\mathrm{q\bar{q}}(\gamma)$ events describe the corresponding data set, we go back to the data collected in 1994 at $\sqrt{s} \simeq 91.2\,\mathrm{GeV}$. Since we have a pure sample of $\mathrm{q\bar{q}}$ events at our disposal at that energy, we are able to select events that look like WW events, without selecting many non $\mathrm{Z} \to \mathrm{q\bar{q}}$ events, which *would* be the case if LEP2 data were used. Although we deal with an energy reduction of a factor two, we are able to use

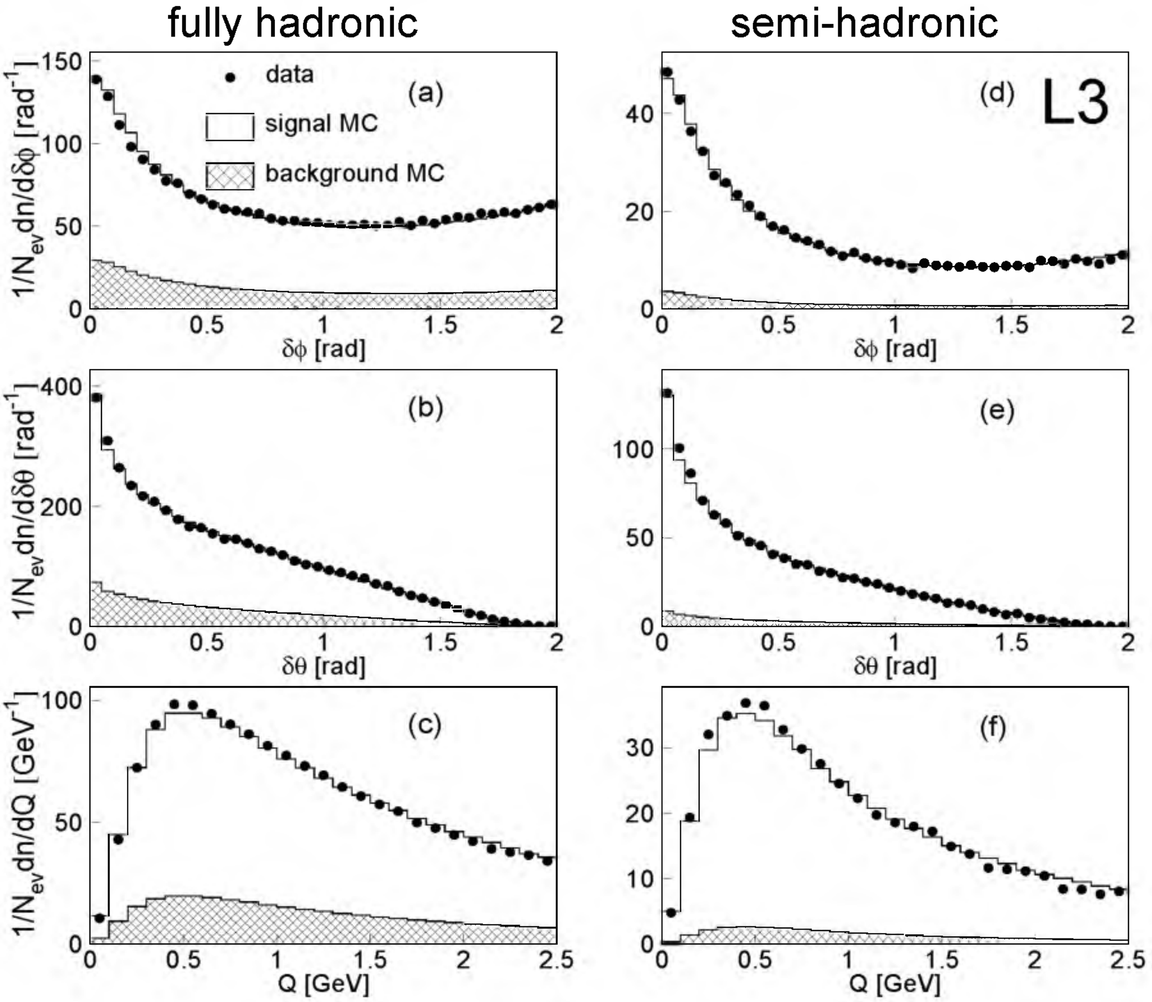

Figure 4.3: Distributions of the difference in azimuthal angle of pairs of tracks $\delta\phi$ ((a) and (d)), the difference in polar angle of pairs of tracks $\delta\theta$ ((b) and (e)), and the inclusive four-momentum difference $Q$ ((c) and (f)), for the fully hadronic WW events (a-c) and the semi-hadronic WW events (d-f). Only like-sign pairs of tracks are considered. The dots are the uncorrected data at 189 GeV, the open histograms are the expectation of KORALW with intra-W BE correlations and the shaded histograms are the background expectation.

the WW selection criteria (as high multiplicity four-jet events with low missing energy) on the LEP1 data. There is a possible dependence of the variables on the centre-of-mass energy. This is especially true for the number of tracks and energy bumps (group of crystals containing energy deposits), which scale, at first approximation, as the logarithm of the energy. However, selecting WW-like events at the Z resonance, serves as a reasonable check to study BEC in this particular sub-sample. About 56k events are selected as WW events that correspond to a fraction of approximately 7% of the total sample investigated.

This fraction is larger than the fraction of selected Z → $q\bar{q}$ events at LEP2. This is mainly due to the fact that the selection requires "well spread" events. At LEP1, most Z → $q\bar{q}$ events have such properties and hence, have the potential to get selected. At LEP2, the two quarks from a Z decay are usually boosted by large amounts. They become narrow jets and are thus no longer well spread and hence not selected.

Fig. 4.4 shows the inclusive $Q$ distribution and the $Q$ distribution after applying the WW selection criteria for fully hadronic WW events, for data and MC (JETSET with BE effects according to the BE$_0$ algorithm) at $\sqrt{s} \simeq 91.2\,\mathrm{GeV}$, after dividing it by the $Q$ distribution computed from a MC without BEC at the detector level in order to make the comparison between data and MC more clear. Reasonable agreement is observed between data and MC for the inclusive $Q$ distribution. This can be expected since it has been tuned, among other variables, to this distribution. Also the $Q$ distributions of the data and MC after the WW selection (fig. 4.4b), show reasonable agreement, except at small values of $Q$ where the MC overestimates the data by approximately 20%. However, the overestimation is small enough to be absorbed into the systematic errors. This gives confidence in taking background events into account via eqn. (4.20).

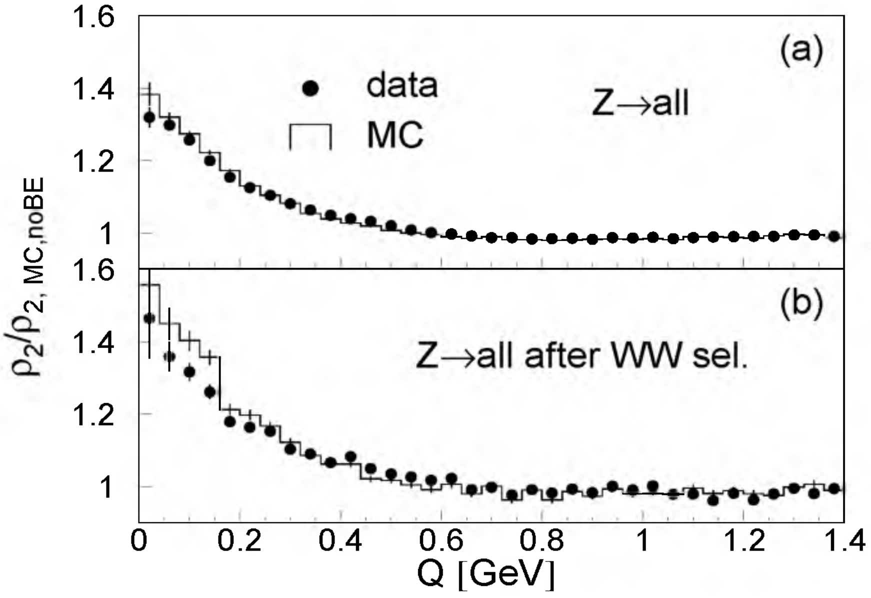

Figure 4.4: The inclusive $Q$ distribution, (a), and the $Q$ distribution after applying the WW selection criteria for fully hadronic WW events, (b), for data and MC (JETSET with BE effects according to the BE$_0$ algorithm) at $\sqrt{s} = 91.2\,\mathrm{GeV}$, after dividing it by the $Q$ distribution computed from a MC without BEC.

## 4.5 Measurement of $R_2$

To compute the BE correlation function, eqns. (4.7) and (4.8) are used. In determining $R_2$ using eqn. (4.7), KORALW without BEC is used as the reference sample. For the detector correction, BES with the $\mathrm{BE}_{32}$ algorithm is used for both eqns. (4.7) and (4.8).

Fig. 4.5 shows the correlation function, eqn. (4.7), for the fully hadronic and for the semi-hadronic WW events, when the data of 1998, 1999 and 2000 are combined.

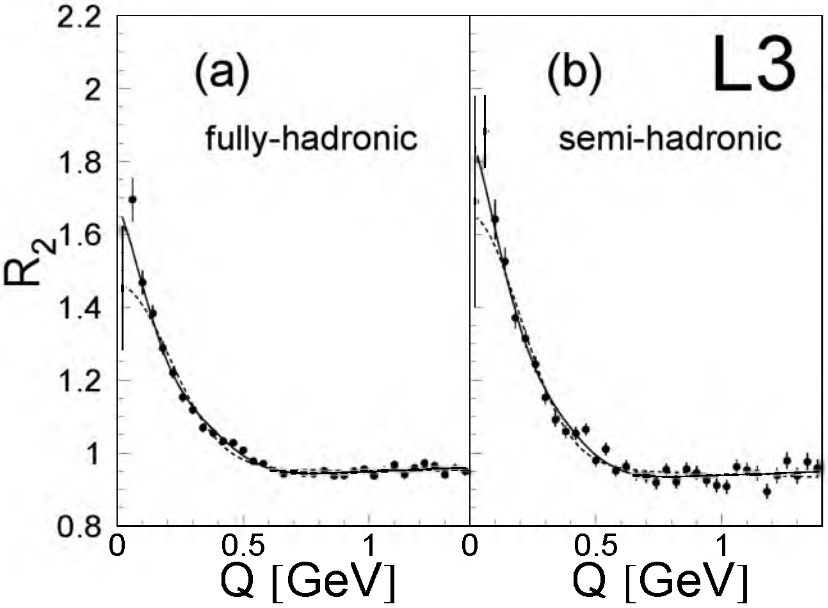

Figure 4.5: The BE correlation function $R_2$, eqn. (4.7), for (a) the fully hadronic WW events, and (b) the semi-hadronic WW events. The full lines correspond to the fit with the lowest-order Edgeworth expansion, eqn. (4.22), the dashed lines to the Gaussian fit, eqn. (4.21).

It has been verified that the results for the different energy bins are compatible with each other, within the statistical uncertainty. The BE enhancement at low $Q$ values is parametrized (from 0 to 1.4 GeV) by the Gaussian

$$R_2(Q) = \gamma(1+\delta Q)(1+\lambda \exp(-R^2Q^2)) \quad , \tag{4.21}$$

and by the lowest-order Edgeworth expansion of the Gaussian (analogously to eqn.(3.15))

$$R_2(Q) = \gamma(1+\delta Q)\left[1+\lambda \exp(-R^2Q^2)\cdot\left(1+\frac{\kappa}{3!}H_3(RQ)\right)\right] \quad . \tag{4.22}$$

The $\gamma$ parameter is an overall normalization factor, the term $(1+\delta Q)$ takes into account possible long-range momentum correlations, $\lambda$ measures the strength of the BEC, $R$ is related to the source size in space-time, $\kappa$ is the third-order cumulant moment measuring the first-order deviation from the Gaussian and $H_3(RQ) \equiv (\sqrt{2}RQ)^3 - 3\sqrt{2}RQ$ is the third Hermite polynomial.

The combined fit results for all energy bins and for both choices of reference sample, eqns. (4.5) and (4.6), are given in table 4.2. The statistical error includes bin-to-bin correlations, by estimating the full covariance matrix and using this in the fit (see subsection 4.5.1). For the estimation of the systematic uncertainty I refer to subsection 4.5.2.

BEC are observed ($\lambda > 0$) in both fully hadronic and semi-hadronic WW events. From both fig. 4.5 and the $\chi^2$ values in table 4.2 we learn that the fit by the lowest-order Edgeworth expansion, eqn. (4.22), does a better job than the Gaussian fit, eqn. (4.21). The values of $\lambda$ are higher for the semi-hadronic than for the fully hadronic channel. However, the difference, for each choice of reference sample and parametrization, is only about 2.5 standard deviations using only the statistical error and about 2 standard deviations using in addition the systematic uncertainty from inter-W BEC on the detector correction factor. Using a MC without BEC to correct the data for detector effects, reduces $\lambda$ in both channels by approximately 30%, but the difference in the $\lambda$ values remains. If true, already this difference in $\lambda$ would indicate a suppression of inter-W BEC [24], which we study in detail in section 4.7.

Table 4.2: Values of the fit parameters $\gamma$, $\lambda$, $R$, $\delta$ and $\kappa$, according to the Gaussian parametrization (subscript G), eqn. (4.21), and the first-order Edgeworth expansion (subscript E), eqn. (4.22), for the fully hadronic and the semi-hadronic WW events. Two different reference samples are used: KORALW without BEC, eqn. (4.5), and unlike-sign particle pairs, eqn. (4.6). The first error is statistical, including bin-to-bin correlations, the second systematic.

| reference | MC, no BEC | | (+, −) pairs | |
|---|---|---|---|---|
| channel | fully hadronic | semi-hadronic | fully hadronic | semi-hadronic |
| $\gamma_\mathrm{G}$ | 0.96±0.01±0.02 | 0.96±0.02±0.02 | 0.99±0.02±0.02 | 0.96±0.02±0.03 |
| $\lambda_\mathrm{G}$ | 0.53±0.03±0.07 | 0.71±0.05±0.05 | 0.44±0.03±0.05 | 0.62±0.06±0.05 |
| $R_\mathrm{G}$ (fm) | 0.67±0.03±0.06 | 0.69±0.05±0.06 | 0.67±0.04±0.05 | 0.85±0.05±0.06 |
| $\delta_\mathrm{G}$ | −0.01±0.01±0.06 | −0.02±0.02±0.06 | 0.02±0.01±0.05 | 0.02±0.02±0.05 |
| $\chi^2_\mathrm{G}$/ndf | 81/31 | 64/31 | 44/31 | 41/31 |
| $\gamma_\mathrm{E}$ | 0.92±0.02±0.02 | 0.92±0.03±0.03 | 0.99±0.03±0.02 | 0.97±0.02±0.03 |
| $\lambda_\mathrm{E}$ | 0.83±0.05±0.09 | 1.03±0.10±0.05 | 0.47±0.05±0.09 | 0.80±0.12±0.06 |
| $R_\mathrm{E}$ (fm) | 0.73±0.05±0.07 | 0.72±0.05±0.07 | 0.68±0.06±0.06 | 0.83±0.06±0.07 |
| $\delta_\mathrm{E}$ | 0.03±0.02±0.06 | 0.02±0.03±0.06 | 0.02±0.02±0.06 | 0.01±0.02±0.07 |
| $\kappa_\mathrm{E}$ | 0.81±0.09±0.10 | 0.53±0.14±0.11 | 0.33±0.21±0.25 | 0.81±0.23±0.26 |
| $\chi^2_\mathrm{E}$/ndf | 35/30 | 43/30 | 40/30 | 38/30 |

### 4.5.1 Bin-to-Bin Correlations

The statistical errors in table 4.2 include the effect of bin-to-bin correlations. The existence of these correlations is obvious when realizing that every event may give many entries in the $Q$ distribution and several entries per $Q$ bin, and that the number of these entries fluctuates strongly from event to event. The elements of the full covariance matrix, $V$, for bins in $Q$, are estimated by

$$V_{jk} = \frac{1}{N_{\mathrm{ev}} - 1} \cdot \sum_{i=1}^{N_{\mathrm{ev}}} (h_j^i - H_j/N_{\mathrm{ev}})(h_k^i - H_k/N_{\mathrm{ev}}) \quad , \tag{4.23}$$

where $i$ runs over the number of events, $h_j^i$ are the number of entries in bin $j$ of event $i$ and $H_j = \sum_i h_j^i$. In case bin-to-bin correlations are absent, we only remain with the diagonal elements, which are equal to

$$V_{jj} = \frac{1}{N_{\mathrm{ev}} - 1} \cdot \sum_{i=1}^{N_{\mathrm{ev}}} (h_j^i - H_j/N_{\mathrm{ev}})^2 \equiv \sigma_j^2 \quad . \tag{4.24}$$

Fig. 4.6 shows the normalized correlation coefficients, $\rho_{ij} \equiv \frac{V_{ij}}{\sigma_i \sigma_j}$, for the $Q$ distribution of the selected fully hadronic and semi-hadronic WW events, at $\sqrt{s} \simeq 189\,\mathrm{GeV}$. Similar results are obtained for the other energy bins, be it with larger statistical fluctuations. From the figure one can conclude that there are non-negligible bin-to-bin correlations, up to 45% in the fully hadronic channel and 30% in the semi-hadronic channel. The difference between the two channels can be explained by the difference in multiplicity: the average multiplicity in fully hadronic WW events is about twice the average multiplicity in semi-hadronic WW events, which leads to more pair combinations per event in the fully hadronic channel and thus to more bin-to-bin correlations. The covariance matrices for unlike-sign particle pairs look similar.

The origin of the bin-to-bin correlations is mainly a consequence of fluctuations of the multiplicity of the events being considered. This can be seen by computing the following adapted covariance matrix

$$\hat{V}_{jk} = \left( \frac{\sum_i^{N_{\mathrm{ev}}} n_i}{N_{\mathrm{ev}}} \right)^2 \cdot \frac{1}{N_{\mathrm{ev}} - 1} \cdot \sum_{i=1}^{N_{\mathrm{ev}}} (\hat{h}_j^i - \hat{H}_j/N_{\mathrm{ev}})(\hat{h}_k^i - \hat{H}_k/N_{\mathrm{ev}}) \quad , \tag{4.25}$$

where $n_i$ is the number of tracks in event $i$, $\hat{h}_j^i = \frac{h_j^i}{n_i}$ and $\hat{H}_j = \sum_i \frac{h_j^i}{n_i}$. This adapted covariance matrix suppresses the multiplicity fluctuations and, as can be seen from fig. 4.7, where the normalized adapted covariance matrix of the selected fully hadronic WW events at 189 GeV is shown, almost all bin-to-bin correlations are removed.

Since we consider the inclusive $Q$ distribution in the computation of $R_2$, and further on in the computation of the test statistics $\Delta\rho$, $D$ and $D'$, we use the covariance matrix as defined in eqn. (4.23). Eqn. (4.25) would be appropriate if fixed multiplicities were considered.

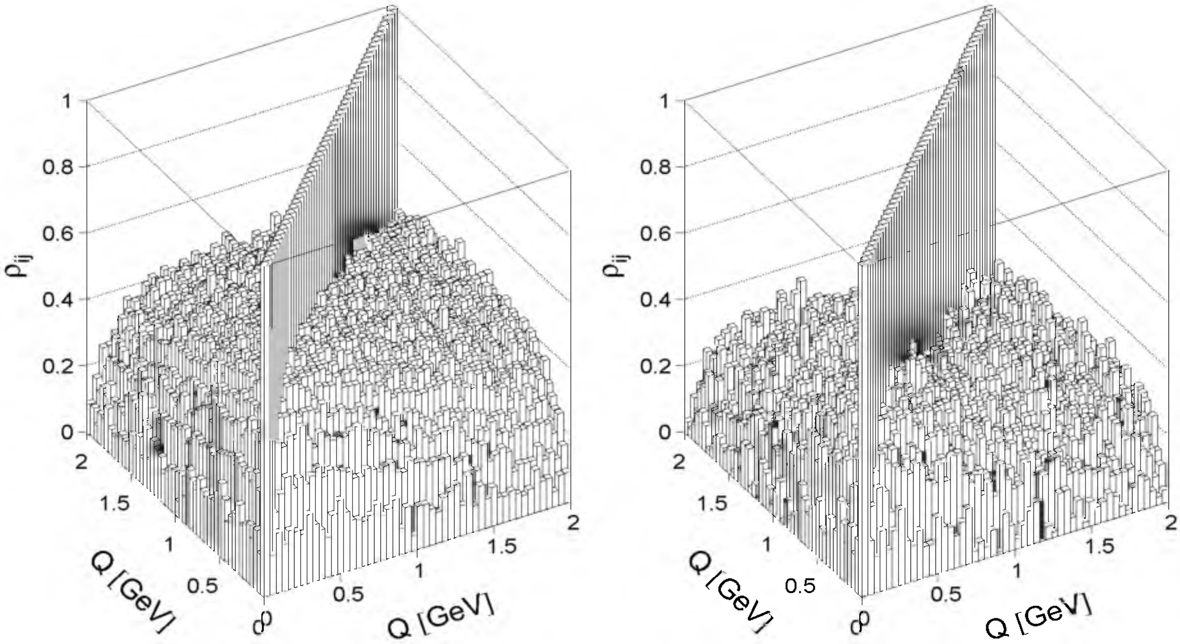

Figure 4.6: Normalized covariance matrices according to eqn. (4.23) for the $Q$ distribution of the selected fully hadronic WW events (left) and semi-hadronic WW events (right), at 189 GeV.

By error propagation, the covariance matrix, $\tilde{V}$, for the BE correlation function, $R_2$, is constructed and a fit is performed by minimizing

$$\chi^2 = \sum_{i=1}^{N_{\rm bins}} \sum_{j=1}^{N_{\rm bins}} \left(f_i^{\rm th} - f_i^{\rm exp}\right) \left(\tilde{V}^{-1}\right)_{ij} \left(f_j^{\rm th} - f_j^{\rm exp}\right) \quad , \tag{4.26}$$

where the sums over $i$ and $j$ run over the number of bins, $N_{\rm bins}$, that is used, $f^{\rm th}$ is the theoretical prediction for $R_2$, i.e., the parametrization that is used, $f^{\rm exp}$ is the measured $R_2$, and $\tilde{V}^{-1}$ is the inverse of the covariance matrix of $R_2$. The fit results, obtained by minimizing (4.26), are given in table 4.2.

The covariance matrix of $R_2$, and also of the test statistics $\Delta\rho$ and the ratios $D$ and $D'$, which are computed further on, is dominated by the statistics of the semi-hadronic WW channel. The reason for this is that the number of semi-hadronic events selected from the data is less than the number of selected fully hadronic events and the number of pair combinations is on average a factor four less than in fully hadronic events.

To see the influence of the bin-to-bin correlations on the fit results, it is investigated what happens if no bin-to-bin correlations are assumed and when the error on the data points is computed, 1. according to a Poisson distribution of the number of entries in each bin (i.e., $\sigma_j = \sqrt{H_j}/N_{\rm ev}$), 2. according to eqn. (4.24).

Within the errors, calculations 1. and 2. do not change the fit results, only the errors change. Assuming the number of entries in each bin to be Poisson distributed, the

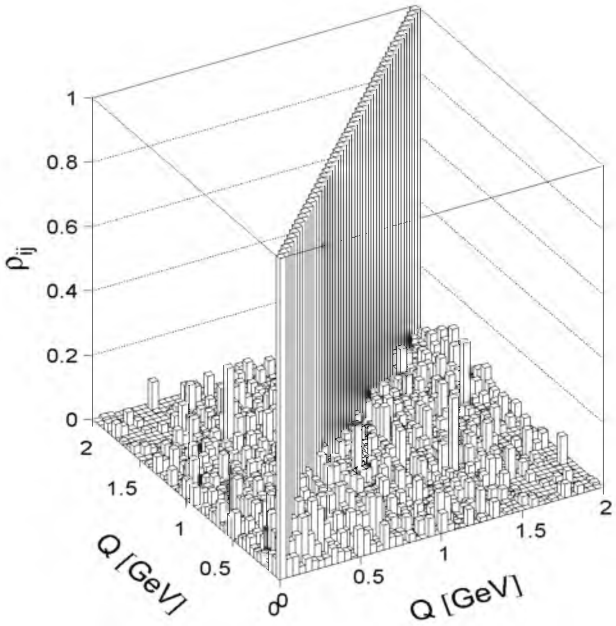

Figure 4.7: Normalized adapted covariance matrix according to eqn. (4.25) for the Q distribution of the selected fully hadronic WW events at 189 GeV.

errors on the fit parameters are 20 to 80% smaller than when the full covariance matrix is used, the 20% corresponding to the situation where unlike-sign pairs are used to make the reference sample and semi-hadronic WW events are considered, the 80% corresponding to the situation where a MC without BEC is used to make the reference sample and fully hadronic WW events are considered. When only the diagonal elements of the covariance matrix are used, i.e., only eqn. (4.24), the errors on the fit parameters are approximately 10 to 20% lower than when the full covariance matrix is used, with the lower and higher values corresponding to the same situations as mentioned above.

### 4.5.2 Systematic Uncertainties

The systematic uncertainties on the fit parameters as quoted in table 4.2 are estimated by studying six different sources. Track and event selections are varied: both stronger and weaker cuts are applied to tracks (i.e., cuts on the number of hits, span, distance of closest approach and transverse momentum are varied), slightly different event selections are made and the background fractions are varied (by ±20%). The maximum deviation that is found by varying each selection criterion, keeping the other cuts at their standard values, is taken as the contribution to the systematic error of the measurement due to this cut. The influence of the choice of the MC used for the reference sample and for the detector correction is also taken into account. The MCs that are used are KORALW and PYTHIA. For the detector correction a MC with BE effects is used, since we find it to agree best with the data in the variables given in fig. 4.3. Using a MC without BEC gives an underestimation at low values of these variables, from a few percent for the angular distributions up to 20% for the $Q$ distribution. For the fully hadronic WW events, both the BES and BEA scenarios are considered. Part of the systematic uncertainty comes from the choice of the fit range: the fit range is varied by ±320 MeV. As a total systematic error, the systematic uncertainties from the different sources are added in quadrature.

The systematic uncertainties are computed for each energy bin, but no significant differences are observed between the different bins. Part of the systematic uncertainties is highly correlated between the different energy bins: variations on track selection, background fractions and including inter-W BEC in the detector correction factor in the fully hadronic channel, show the same behaviour in each of the bins. The other systematic uncertainties are highly uncorrelated. For each of the sources, the total systematic error when all energy bins are combined, is obtained by taking the average of the correlated systematic errors and the RMS of the uncorrelated systematic errors.

The contributions to the systematic error on $\lambda$ when all energy bins are combined, are shown in table 4.3. The large systematic uncertainty on $\lambda$ in the fully hadronic channel is mainly due to the difference of including or not including inter-W BEC in the MC for the detector correction. Using inter-W BEC in the correction factor increases the measured value of $\lambda$. The sources of systematic uncertainties labelled with a * are the correlated uncertainties.

Table 4.3: Contributions to the systematic uncertainty on the $\lambda$ parameter, according to the Gaussian parametrization (subscript G) and the first-order Edgeworth expansion of the Gaussian (subscript E). Explanation of the sources is given in the text. Sources labelled with a * are highly correlated between the different energy bins.

| reference | MC, no BEC | | | | (+, −) pairs | | | |
|---|---|---|---|---|---|---|---|---|
| channel | fully hadronic | | semi-hadronic | | fully hadronic | | semi-hadronic | |
| fit parameter | $\lambda_G$ | $\lambda_E$ | $\lambda_G$ | $\lambda_E$ | $\lambda_G$ | $\lambda_E$ | $\lambda_G$ | $\lambda_E$ |
| track selection* | 0.039 | 0.042 | 0.035 | 0.031 | 0.034 | 0.034 | 0.032 | 0.036 |
| event selection | 0.015 | 0.011 | 0.017 | 0.014 | 0.022 | 0.026 | 0.022 | 0.023 |
| background fraction* | 0.011 | 0.011 | 0.008 | 0.009 | 0.020 | 0.022 | 0.023 | 0.019 |
| fit range | 0.013 | 0.018 | 0.013 | 0.020 | 0.020 | 0.029 | 0.023 | 0.030 |
| other MC reference | 0.014 | 0.013 | 0.015 | 0.013 | 0.019 | 0.018 | 0.018 | 0.021 |
| other MC corr. | 0.012 | 0.014 | 0.016 | 0.019 | 0.015 | 0.025 | 0.014 | 0.019 |
| inter-W BE in MC corr.* | 0.051 | 0.071 | - | - | 0.048 | 0.057 | - | - |
| total | 0.07 | 0.09 | 0.05 | 0.05 | 0.07 | 0.09 | 0.05 | 0.06 |

## 4.6 Comparison with Z decay Events

Since, apart from the quark flavour, hadronic W and Z decays are expected to be similar, a high statistics hadronic Z decay sample, collected by the L3 detector in 1994 at $\sqrt{s} \simeq 91.2\,\mathrm{GeV}$, is analysed.

### 4.6.1 b-tagging Procedure

Since b quarks are greatly suppressed in W decay (the LEP energy is too low to produce a W that decays into a bottom and a top quark, which is by far the most dominant W decay mode that would include a b-quark), a b-tagging procedure [86] is used to reduce the $\mathrm{b\bar{b}}$ fraction in Z decays from 22% to 3%. The b-tagging procedure works as follows. The technique, which is possible due to the presence of the SMD, see subsection 2.2.2, makes use of the relatively long lifetime and hence the relatively long decay length of B mesons to tag $\mathrm{Z} \to \mathrm{b\bar{b}}$ events. The mean lifetime of B mesons is approximately $1.5 \cdot 10^{-12}$ s, corresponding to a mean decay length of approximately 0.5 mm. The decay length tag starts by reconstructing the primary vertex of the event in three dimensions. This is done by minimizing the following $\chi^2$

$$\chi^2 = \sum_{i=1}^{N} \left(\vec{t}_i - \vec{f}(\vec{v}, \vec{q}_i)\right)^{\mathrm{T}} G_i^{-1} \left(\vec{t}_i - \vec{f}(\vec{v}, \vec{q}_i)\right) (\vec{v} - \vec{v}_{\mathrm{fill}})^{\mathrm{T}} V_{\mathrm{fill}}^{-1} (\vec{v} - \vec{v}_{\mathrm{fill}}) \quad , \tag{4.27}$$

where the sum runs over the $N$ number of tracks under consideration (see [86]), $\vec{t}_i$ is the vector of measured parameters for track $i$, $G_i$ the corresponding covariance matrix, $\vec{f}(\vec{v}, \vec{q}_i)$ the predicted measurement assuming the track originates from the vertex $\vec{v}$ with momentum $\vec{q}_i$, $\vec{v}_{\mathrm{fill}}$ the so-called fill or $M$-event vertex [87, 88], which is the mean event vertex in $M$ events, and $V_{\mathrm{fill}}$ the matrix describing the size of the beam spot. A typical value for $M$ in the $M$-event vertex is 200 and the time between event 1 and $M$ is around 15 min. Typical sizes for the beam spot are 150 $\mu$m in the $x$ direction and 10 $\mu$m in the $y$ direction.

Once the primary vertex is reconstructed, it is used as the reference point of the tracks in the event and defines the tracks' distance of closest approach in the $r$–$\phi$ and $s$–$z$ planes. The distances between the crossing points in the two planes of each track with the axis of the jet ($\hat{j}$) containing that track and the primary vertex ($\vec{V}$), are denoted by $L_{r\phi}$ and $L_{sz}$. This is illustrated in fig. 4.8, for positive $L_{r\phi}$ and $L_{sz}$. $L_{r\phi}$ and $L_{sz}$ are defined to be negative when the vertex is on the other side of the crossing point. Defined in this way, $L_{r\phi}$ and $L_{sz}$ represent approximately independent measurements of the decay length of a particle and can be averaged to form the decay length $L$ [86]. To compute the probability that a certain track with decay length $L$ is compatible with originating from the primary vertex, the significance $S = L/\sigma_L$ is introduced, where $\sigma_L$ is the error on the decay length $L$. Let $P(S)$ be the probability that a track originates from the primary vertex, with the property

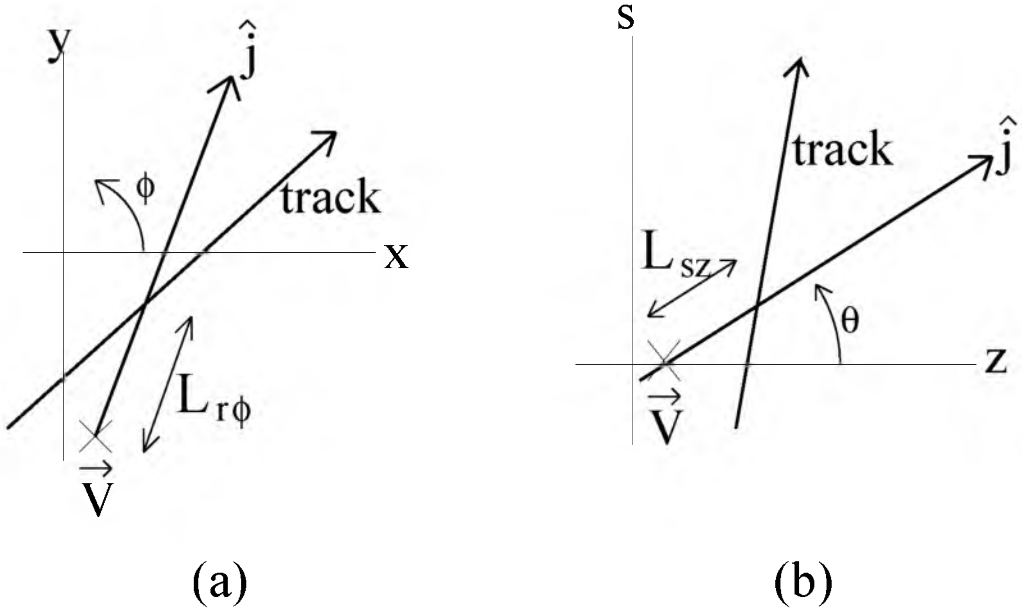

Figure 4.8: The tagging variable in the $r$–$\phi$ plane, $L_{r\phi}$, (a), and in the $s$–$z$ plane, $L_{sz}$, (b). The cross indicates the position of the primary vertex and $\hat{j}$ the axis of the jet containing the track.

that $P(S) \to 1$ when $S \to 0$, then one can define the following event probability [86,89]

$$P_{\text{ev}} = \frac{\Pi}{2^N} \sum_{i=0}^{N-1} \sum_{j=i+1}^{N} \binom{N}{j} \frac{(-\ln\Pi)^i}{i!} \quad , \tag{4.28}$$

where $\Pi = \prod_{j=1}^{N^+} P(S_j)$, with $N^+$ the number of tracks with positive decay length. Thus, the probability, $P(S)$, for any track with negative decay length is defined to be equal to the probability of a track with zero decay length, i.e., $P(S) = 1$ for $S \leq 0$. The sums over $i$ and $j$ run over the total number of tracks $N$ in the event. In the case that events contain no long-lifetime particles, the distribution of $P_{\text{ev}}$ is flat, while events that do contain long-lifetime particles have probabilities close to zero. Since the event probability is very small in case of Z → b$\bar{\text{b}}$ decays, one can expand the region of interest by defining the discriminant

$$B_{\text{ev}} \equiv -\log(P_{\text{ev}}) \quad . \tag{4.29}$$

The value of this discriminant will be used to distinguish light-quark (u, d, s or c) Z decay events from Z → b$\bar{\text{b}}$ events. A sample of light-quark Z decays can be selected by demanding $B_{\text{ev}}$ to be smaller than a certain value.

In fig. 4.9 the b-tagging performance is shown. The distribution of the event-discriminant, $B_{\text{ev}}$, and the purity and efficiency as a function of a cut on the discriminant, where only the events with lower values than the cut are accepted, are shown for the 1994 data and MC (with BE effects). The overflows are entered into the last bin. For the MC,

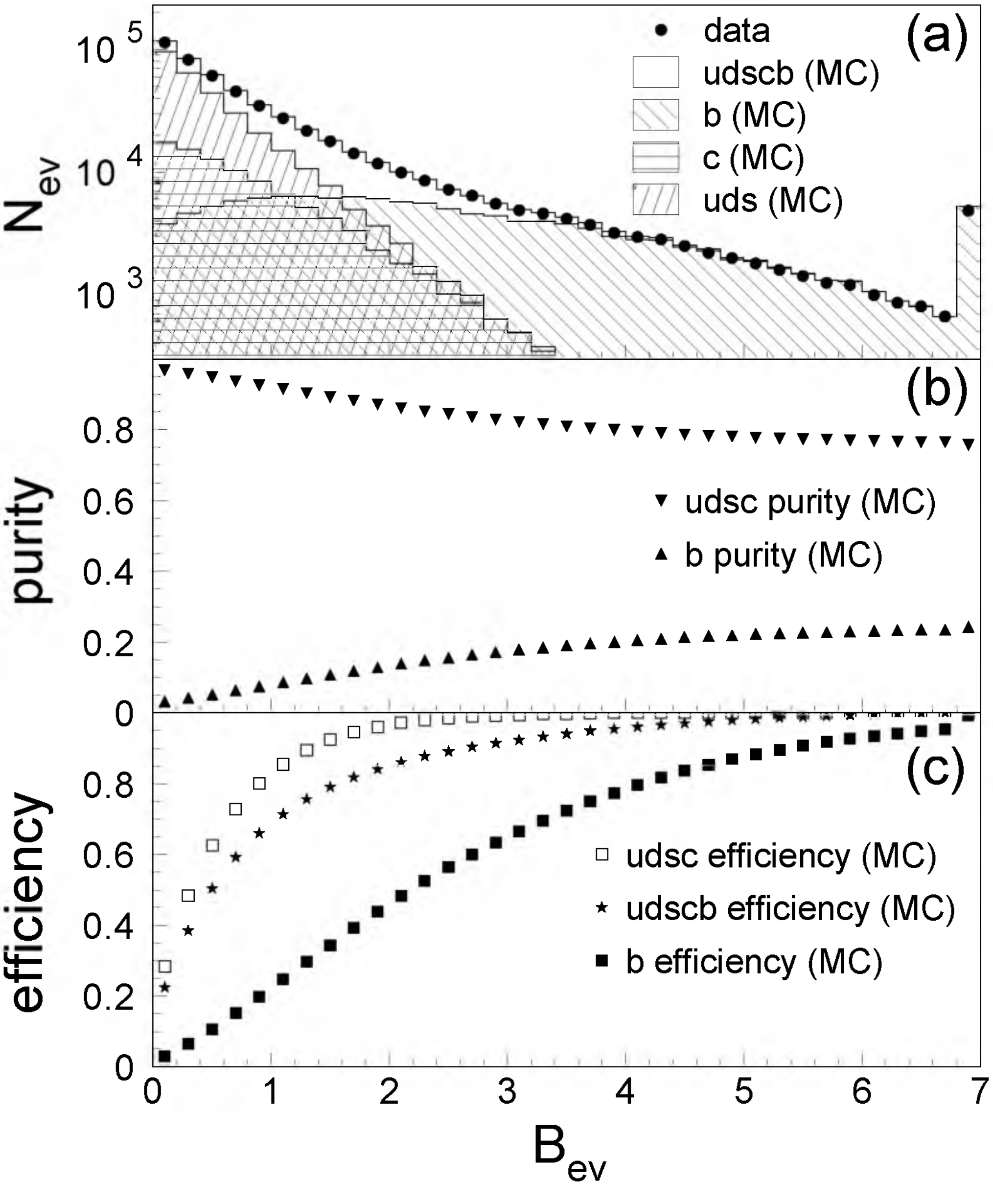

Figure 4.9: The distribution of the event-discriminant, $B_{\mathrm{ev}}$, for the 1994 data and MC is shown in (a). The purity and efficiency as a function of a cut on the discriminant, where only the events on the left side of this cut are accepted, are shown in (b) and (c). The overflows are entered into the last bin. For the MC, different hadronic Z decay channels are shown: only $b\bar{b}$ decays, "b", only $c\bar{c}$ decays, "c", only quark antiquark pair decays with u, d or s flavour, "uds", only light-quark decays, "udsc", and all channels, "udscb".

different hadronic Z decay channels are shown: only $b\bar{b}$ decays, “b”, only $c\bar{c}$ decays, “c”, only quark antiquark pair decays with u,d or s flavour, “uds”, only light-quark decays, “udsc”, and all channels, “udscb”. From fig. 4.9a, one observes good agreement between data and MC when all hadronic decay channels are considered.

To obtain a relatively pure sample of light-quark Z decays, a cut of $B_{\text{ev}} < 0.3$ is chosen. This results in a udsc purity of 97% and an udsc efficiency of 48%, or 180k selected events.

### 4.6.2 Results

From the high statistics light-quark Z decay sample, the BE correlation function is obtained in the same way as for the WW events, i.e., by using eqns. (4.7) and (4.8), respectively. In fig. 4.10, the BE correlation function, eqn. (4.7), is shown for the fully hadronic and semi-hadronic WW events (as in fig. 4.5). The BE correlation function extracted from the 180k light-quark Z decay events is plotted in fig. 4.10b as a full histogram. As expected, good agreement is observed between this histogram and the correlation function of the semi-hadronic WW events. The statistical error on this histogram is negligible and the same cuts on tracks are used as on the WW events. Furthermore, it is checked that varying the cut on the discriminant, $B_{\text{ev}}$, in the range 0.15 to 0.8 hardly changes the BE correlation function.

On the contrary, when b quark decays of the Z are not removed from the sample (dashed histogram in fig. 4.10b), a depletion of the correlation function at small $Q$ is observed and a clear discrepancy exists with the WW data. The same observations are made when the BE correlation function is computed according to eqn. (4.8). The depletion can be expected since B mesons (that mainly decay into pions) produced in $Z \rightarrow b\bar{b}$ events travel some distance before they decay. Consequently, the distance between two pions produced in $b\bar{b}$ events will on average be larger than in light-quark Z decay events, leading to less correlations.

Under the assumption that the light-quark Z decay sample describes the BE correlation function for semi-hadronic WW events, the BE correlation function in the fully hadronic channel can be estimated by eqn. (4.16) for the case of absence of inter-W BEC. For this estimation, firstly, the overlap function, $F(Q)$, eqn. (4.13), needs to be computed. For this, a mixing technique is used (see subsection 4.7.1) to determine from a MC without BEC the fraction of pairs with one particle from $W^+$ and the other from $W^-$, as a function of $Q$. Assuming that there are no inter-W BEC, these pairs do not contribute to the correlation function of the fully hadronic channel. In fig. 4.11, $F(Q)$ is shown when KORALW without BEC is used. Going to low values of $Q$, the fraction of pairs where both particles come from the same W increases. This is to be expected since, in general, the momentum difference between two particles within a jet is smaller than between two particles coming from different jets. Using this result in eqn. (4.16), one is now able to estimate the BE correlation function for fully hadronic WW events, when inter-W BEC are absent. The result is shown in fig. 4.10a. Good agreement is observed at low $Q$ between the histogram and the data points, thus indicating no or only weak inter-W BEC.

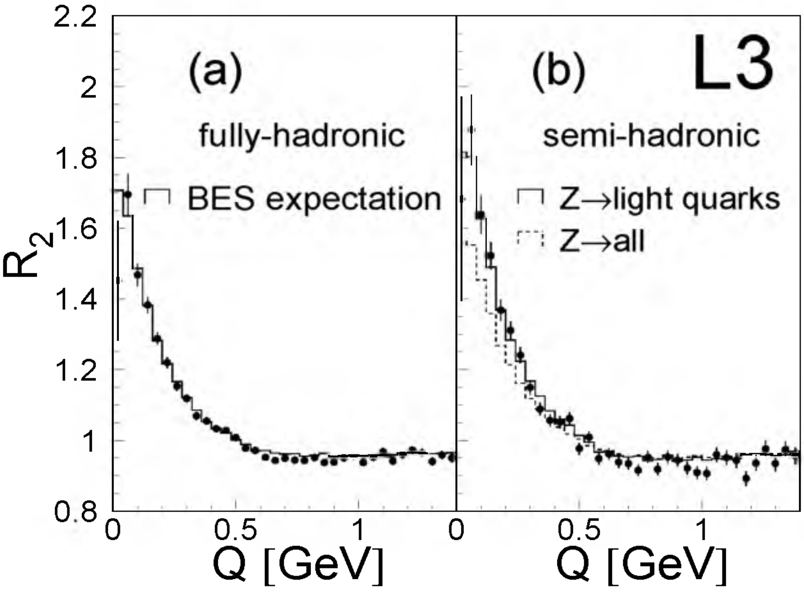

Figure 4.10: The BE correlation function $R_2$, eqn. (4.7), for (a) the fully hadronic WW events, and (b) the semi-hadronic WW events. In (a) the full histogram gives the expectation when inter-W BEC are absent. In (b) the full histogram is for the light-quark Z decay data sample and the dashed histogram is for the data sample containing all hadronic Z decays.

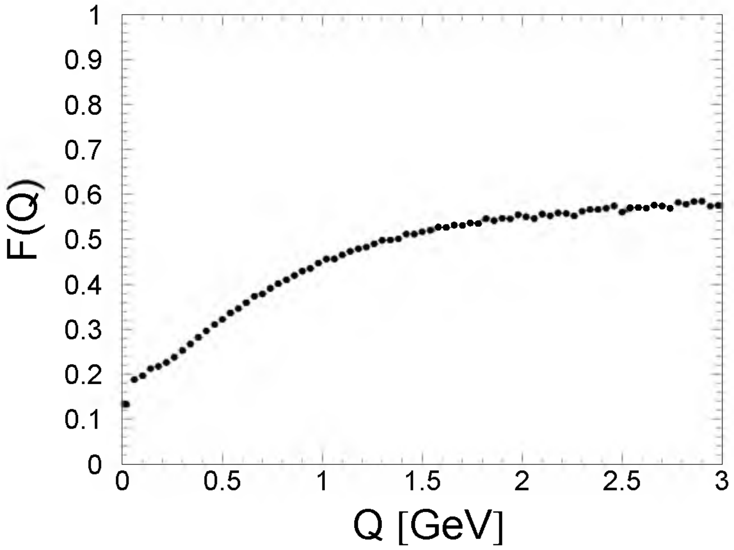

Figure 4.11: Fraction of pairs with one particle coming from $W^+$ and the other from $W^-$, as a function of $Q$, $F(Q)$, according to KORALW without BEC.

## 4.7 Measurement of Inter-W BEC

In this section, a direct measurement is performed of inter-W BEC. The hypothesis that the two W's decay independently is tested using eqns. (4.17), (4.18) and (4.19).

### 4.7.1 Mixing Procedure

To compute these test statistics, the two-particle density $\rho_{\mathrm{mix}}^{\mathrm{W^+W^-}}$ needs to be constructed. This is done by combining two semi-hadronic events having oppositely charged hadronically decaying W's. Particles identified as decay products of a leptonically decaying W are discarded and the sum of the momenta of the particles originating from a hadronically decaying W is used to estimate the direction and momentum of that W. In general, in semi-hadronic events, the charge of the leptonically decaying W is easy to reconstruct by determining the charge of the lepton. Hence, the charge of the hadronically decaying W is the opposite of the charge of the leptonically decaying W. Then, the particles from one of the two events are rotated as follows: Since real fully hadronic WW events have a small longitudinal energy imbalance that we ascribe to initial state radiation (ISR) and since experimental resolution leads to both transverse and longitudinal energy imbalance, we do not force the W's to be exactly back-to-back. We introduce an extra momentum, $\vec{p}_{\mathrm{extra}}$, Gaussian distributed in all three components, and impose $\vec{p}_{\mathrm{extra}} + \vec{W}_1 = -\vec{W}_2$, where $\vec{W}_{1,2}$ are the momenta of the two W's. For the longitudinal component the Gaussian has mean 0 and standard deviation 7.9 GeV, while for the transverse components the mean is randomly chosen as $\pm 0.5$ GeV and the standard deviation is 1.4 GeV. These values were chosen to obtain reasonable agreement between the energy imbalance distributions of fully hadronic and mixed events.

In addition, the following cuts, related to the pre-selection of real fully hadronic WW events [80–82] are imposed: Only events with sphericity [90] bigger than 0.045 are accepted. After forcing the event into two jets with the Durham clustering algorithm [83], the average of the jet masses is required to be bigger than 30 GeV. After forcing the event into four jets with the Durham clustering algorithm, we assign two pairs of jets to the two W's by rejecting the combination with the smallest dijet mass and accepting the combination with the smallest difference between the two dijet masses of the remaining two pairing possibilities (best pairing). We then demand that the total visible energy be larger than $0.7\sqrt{s}$, that the number of particles identified with the calorimeter (the cluster multiplicity) be larger than 30, that the ratio of the total longitudinal energy imbalance to the visible energy be smaller than 0.25, that the $y$-cut value at which the event changes from a three- to a four-jet topology, $y_{34}$, be larger than 0.001, that the difference between the two W masses be less than 70 GeV, that the smallest angle between any two jets be larger than 0.28 radians, and that the average of the two smallest angles between two jets from different W's be bigger than 0.6 radians. These cuts reject only approximately 2% of the events and hardly change the $Q$ distribution.

The final selection of fully hadronic events involves a neural network [80–82], see subsection 4.4.1, with an efficiency of approximately 88% for a cut of 0.6 on the neural network output. We find that about 92% of the mixed events pass this neural network selection. The influence of the cut on the neural-net output at 0.6 on the mixed events is included in the systematic error.

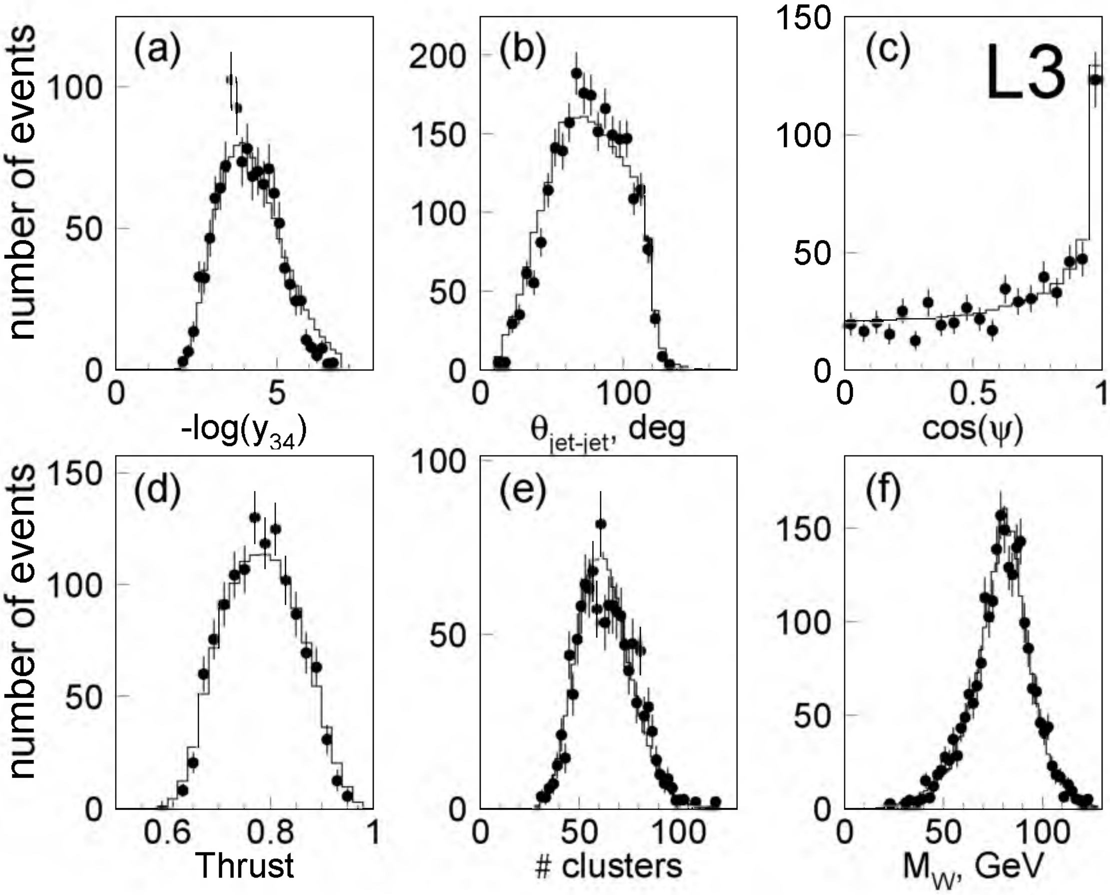

Figure 4.12: Comparison of uncorrected distributions for fully hadronic events after background subtraction (dots) and mixed events (histograms), at 189 GeV: (a) $-\log y_{34}$, (b) the two smallest angles between jets of different W's, after jet finding and best pairing, (c) the cosine of the angle $\psi$ between the decay planes of the two W's, after jet finding and best pairing, (d) the event thrust, (e) the number of clusters, and (f) the W mass after best pairing.

The mixing procedure has been checked by comparing the distributions and quantities of the following variables between mixed events and real fully hadronic WW events, for each energy bin: thrust; sphericity; visible energy; cluster multiplicity; charged-particle multiplicity; sum of momenta of all tracks; longitudinal and transverse energy imbalance computed from the energy deposition in the calorimeter; longitudinal and transverse momentum imbalance computed from the momenta of the tracks; $y_{23}$; $y_{34}$; $y_{45}$; jet mass (after jet finding); energy difference between the two W's after jet finding and for the three possible pairings of jets; mass difference between the two W's after jet finding and for the three possible pairings of jets; sum of masses of the two W's after jet finding and for the three possible pairings of jets; angle between the W's after jet finding and best pairing; angle between the decay planes of the two W's after jet finding and best pairing; the angle between two jets for each of the six possible pairs of jets; the sum of these six angles; energy and mass of the W after jet finding and best pairing; the five angles related to the analysis of the triple gauge couplings, i.e., the polar angle of the W's and the angles of the jets in the $\mathrm{W}^+$ and $\mathrm{W}^-$ rest frame; $\frac{\langle N_1 N_2 \rangle}{\langle N_1 \rangle \langle N_2 \rangle}$ and $\frac{\langle E_1 E_2 \rangle}{\langle E_1 \rangle \langle E_2 \rangle}$ after jet finding and best pairing, where $N_1$ and $N_2$ are the cluster multiplicities and $E_1$ and $E_2$ the energies of the two W's. The dependence of inter-W correlations on these variables is found to be negligible from MC studies. Examples are shown in fig. 4.12 and in general good agreement is observed between the mixed events and the real WW events. For all the other variables the agreement is more or less similar.

### 4.7.2 Results

Fig. 4.13 shows the distributions of the three terms in the right-hand side of eqn. (4.17) for the data at 189 GeV. The distributions have not been corrected for detector effects, but MC-estimated background has been subtracted, using eqn. (4.20), from $\rho_2^{\mathrm{W}}$ and $\rho_2^{\mathrm{WW}}$.

At low values of $Q$ we observe more pairs of unlike-sign particles than pairs of like-sign particles, both in the two-particle densities for fully hadronic (fig. 4.13a) and semi-hadronic (fig. 4.13b) events. Furthermore, we observe that $\rho_{\mathrm{mix}}^{\mathrm{WW}}(\pm,\pm)$ and $\rho_{\mathrm{mix}}^{\mathrm{WW}}(+,-)$ coincide (fig. 4.13c). Similar results are obtained for the other energy bins, except that the statistical errors are larger.

From these distributions, $\Delta\rho$ for like-sign and unlike-sign particle pairs, eqn. (4.17), is computed. The resulting raw data distributions, after combining all energy bins, are shown in fig. 4.14. Also shown are the predictions of KORALW after full detector simulation, reconstruction and selection. Both the BEA and BES scenarios, using $\mathrm{BE}_{32}$, are shown.

The BEA scenario shows an enhancement in the $\Delta\rho$ distribution for like-sign pairs (fig. 4.14a), but also a small enhancement for unlike-sign pairs (fig. 4.14b). The effect for unlike-sign pairs is larger if $\mathrm{BE}_0$ is used, see fig. 4.15, where the MC predictions for $\Delta\rho$ are derived from the $\mathrm{BE}_0$ algorithm. These implementations of BEC, which are based on shuffling the momenta of particles, clearly affect both the like-sign and unlike-sign particle spectra.

The BES scenario shows a flat distribution in both the like-sign and unlike-sign distributions, except at low $Q$ ($0 < Q \lesssim 0.8\,\mathrm{GeV}$) where a small dip is observed. This dip is a consequence of the selection procedure and the mixing technique. Since we look at uncorrected distributions a deviation from a flat distribution might occur. Fortunately, the dip is small and we can clearly distinguish both MC scenarios, so that we take the dip for granted here. Further on, the $D'$ variable is computed where artificial distortions of the mixing procedure and detector related effects are diminished by dividing the uncorrected data distribution by a MC distribution at detector level.

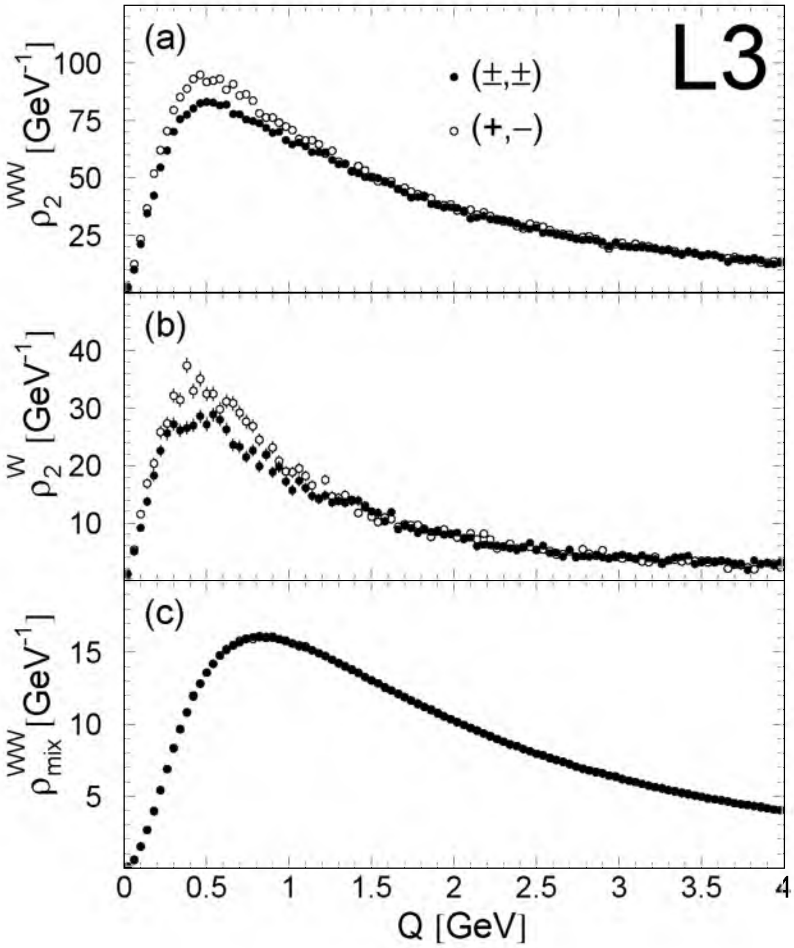

Figure 4.13: Distributions for uncorrected data at 189 GeV of (a) $\rho_2^{\mathrm{WW}}$, (b) $\rho_2^{\mathrm{W}}$ and (c) $\rho_{\mathrm{mix}}^{\mathrm{W^+W^-}}$ for pairs of like-sign tracks and pairs of unlike-sign tracks.

From figs. 4.14a and 4.15a (and even 4.15b) it is clear that the BES scenario describes the $\Delta\rho(\pm,\pm)$ distribution, while the BEA scenario is disfavoured.

For a quantitative comparison, the integral

$$J \equiv \int_0^{Q_{\max}} \Delta\rho(Q)\,\mathrm{d}Q \quad , \tag{4.30}$$

is computed for like-sign and unlike-sign track pairs. Taking $Q_{\max} = 0.68\,\mathrm{GeV}$ (the value where the two MC scenarios have converged to less then one standard deviation), the values of $J$ are computed, for each energy bin, and summarized in table 4.4. In the last two rows of the table the results of two MC scenarios are given: KORALW with BEA (inter-W) and BES (no inter-W), both after simulation, reconstruction and WW selection. Within the statistics that are used for the MC, no energy dependence is observed between 189

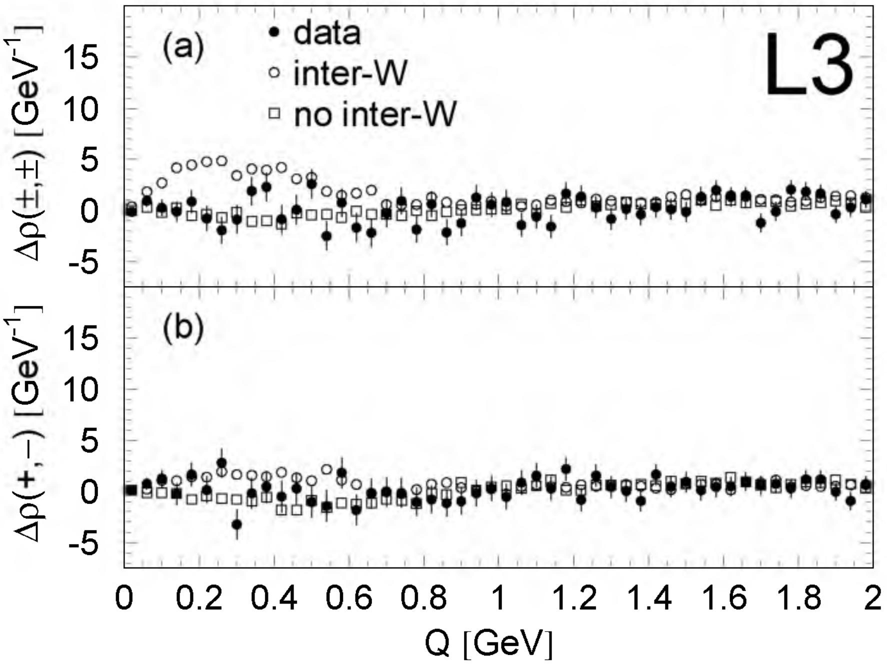

Figure 4.14: Distributions for uncorrected data at 189-209 GeV of (a) $\Delta\rho(\pm,\pm)$ and (b) $\Delta\rho(+,-)$. Also shown are the MC predictions of KORALW (at the detector level) with BEA (inter-W) and BES (no inter-W). BEC are simulated according to $BE_{32}$.

Table 4.4: The integral values, $J$, for like-sign track pairs and unlike-sign track pairs, and the values of the $\Lambda$ parameter, eqn. (4.31), for each energy bin. The last two rows give the prediction of two MC scenarios: KORALW with BEA (inter-W) and BES (no inter-W). The first error is statistical, the second systematic.

| energy bin, GeV | $J(\pm,\pm)$ | $J(+,-)$ | $\Lambda$ |
|---|---|---|---|
| 189 | $-0.20 \pm 0.62 \pm 0.24$ | $-0.22 \pm 0.66 \pm 0.25$ | $0.001 \pm 0.029 \pm 0.015$ |
| 192 | $0.70 \pm 1.53 \pm 0.25$ | $1.06 \pm 1.66 \pm 0.25$ | $0.076 \pm 0.080 \pm 0.017$ |
| 196 | $0.04 \pm 0.98 \pm 0.22$ | $-0.18 \pm 1.07 \pm 0.25$ | $-0.012 \pm 0.045 \pm 0.015$ |
| 200 | $0.49 \pm 0.94 \pm 0.22$ | $0.24 \pm 1.00 \pm 0.23$ | $0.031 \pm 0.044 \pm 0.016$ |
| 202 | $0.58 \pm 1.24 \pm 0.26$ | $0.07 \pm 1.35 \pm 0.26$ | $0.051 \pm 0.073 \pm 0.014$ |
| 205 | $-0.44 \pm 0.90 \pm 0.25$ | $0.28 \pm 0.97 \pm 0.24$ | $-0.022 \pm 0.046 \pm 0.015$ |
| 207 | $-0.08 \pm 0.71 \pm 0.25$ | $-0.28 \pm 0.75 \pm 0.25$ | $0.003 \pm 0.041 \pm 0.018$ |
| 208 | $0.66 \pm 2.51 \pm 0.29$ | $0.98 \pm 2.98 \pm 0.26$ | $0.012 \pm 0.130 \pm 0.018$ |
| total | $0.02 \pm 0.33 \pm 0.24$ | $-0.01 \pm 0.35 \pm 0.25$ | $0.007 \pm 0.017 \pm 0.016$ |
| MC inter-W | $1.78 \pm 0.10$ | $0.67 \pm 0.10$ | $0.126 \pm 0.008$ |
| MC no inter-W | $-0.34 \pm 0.10$ | $-0.43 \pm 0.10$ | $0.000 \pm 0.008$ |

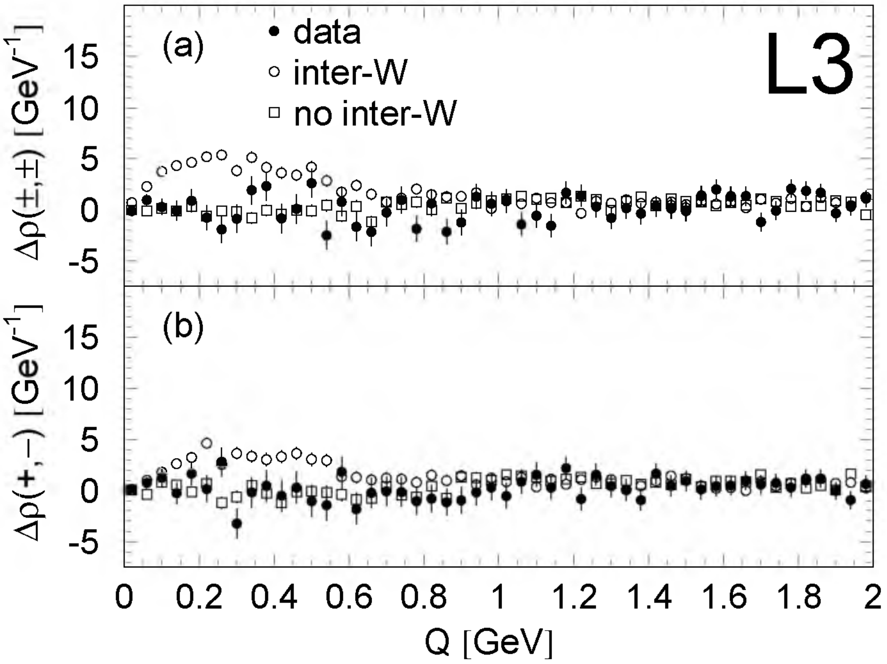

Figure 4.15: Distributions for uncorrected data at 189-209 GeV of (a) $\Delta\rho(\pm,\pm)$ and (b) $\Delta\rho(+,-)$. Also shown are the MC predictions of KORALW (at the detector level) with BEA (inter-W) and BES (no inter-W). BEC are simulated according to $\mathrm{BE}_0$.

and 208 GeV. The statistical errors include bin-to-bin correlations (see subsection 4.7.3). The estimation of the systematic uncertainties are given in subsection 4.7.4. In addition, fig. 4.17 shows the results of $J(\pm,\pm)$ for each energy bin. The errors are statistical only, taking into account bin-to-bin correlations. Also shown in this figure (as a vertical band) is the prediction of KORALW BEA, which clearly disagrees with the data.

From the values of $J$ in table 4.4 one can conclude that the MC without inter-W BEC describes the data (within one standard deviation), whereas the MC with inter-W BEC disfavours the data by approximately four standard deviations.

As a check, the integral is also computed over the full range of $Q$ for the two MC scenarios (note that this range extends up to several tens of GeV). Since there is no change in multiplicity when switching on the BEC (intra-W or both intra- and inter-W) in the MC, these integrals should be zero. Indeed, when all generated events are used, including the non-selected events, the integral is zero for both scenarios. However, after applying the selection, the integral for BEA is found to be $1.2 \pm 0.4(\mathrm{stat})$ and for BES $0.1 \pm 0.4(\mathrm{stat})$. For the experimental data $1.1 \pm 1.7(\mathrm{stat})$ is found. The difference between the two MCs and the excess in the BEA scenario are due to the selection procedure. A few fully hadronic WW events with high multiplicity (out of approximately 40k events), that give relatively many pairs of particles, are not selected in the BES scenario, but are selected in the BEA scenario. This leads to the non-zero value of the integral in the BEA case. To estimate the effect on the significance of the results in this section, the $\Delta\rho$ distributions of both the data and the two MCs, are normalized such that their integrals over the full range of $Q$ are exactly zero. Consequently, the disfavour of the BEA scenario decreases by approximately 0.2 standard deviations.

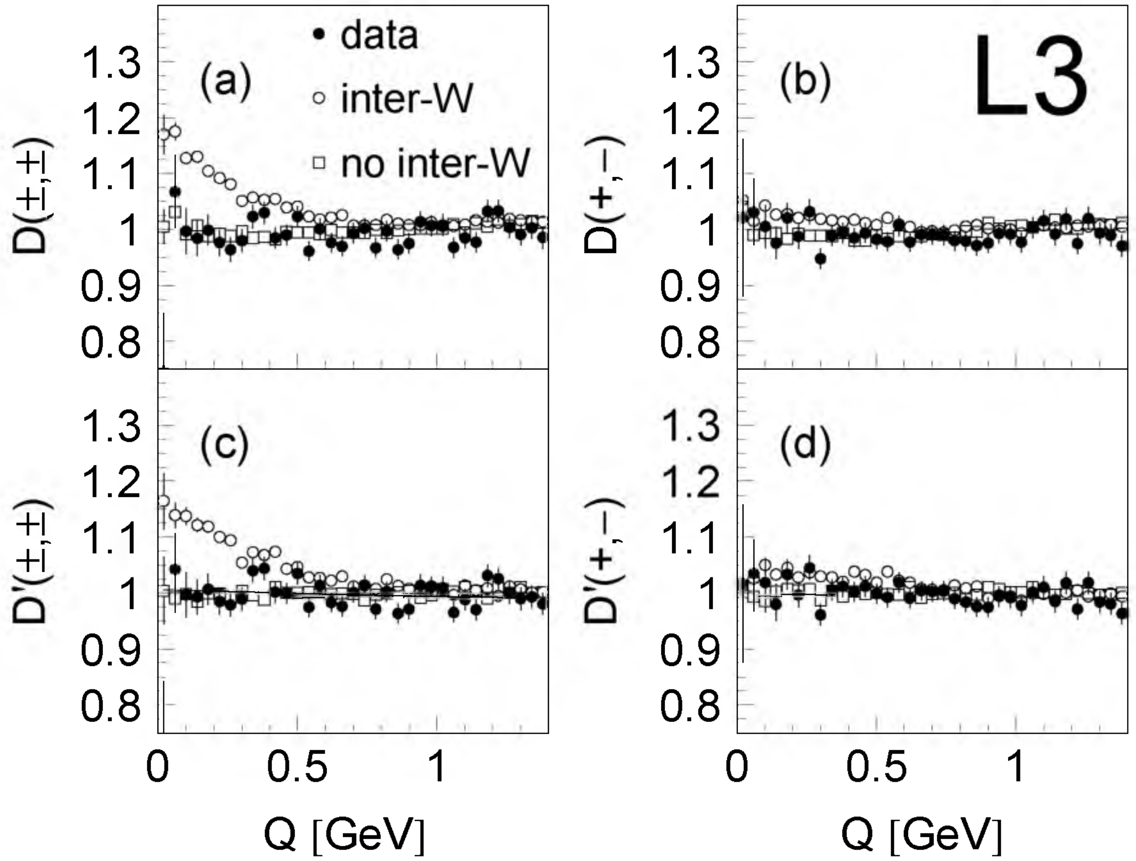

Figure 4.16: Distributions for uncorrected data at 189-209 GeV of (a) $D(\pm,\pm)$, (b) $D(+,-)$, (c) $D'(\pm,\pm)$ and (d) $D'(+,-)$. Also shown are the MC predictions of KORALW (at the detector level) with BEA (inter-W) and BES (no inter-W).

In fig. 4.16 the distributions of $D$ and $D'$ are shown for like-sign and unlike-sign track pairs, eqns. (4.18) and (4.19), for the raw data. For the double ratio $D'$ the BES scenario of KORALW is used as the reference sample. Also shown in the figure are the predictions of KORALW for the scenarios BEA and BES. Again, it is clear that the BES scenario of KORALW describes the data, while the BEA scenario is disfavoured. The same conclusions are obtained when $\mathrm{BE}_0$ is used instead of $\mathrm{BE}_{32}$. Within the statistics that are used for the MC, no energy dependence is observed between 189 and 208 GeV. Note that the $D'$ distributions are by definition equal to unity (apart from statistical fluctuations) when KORALW without inter-W BEC is used. Note also that $D$ is already close to unity for

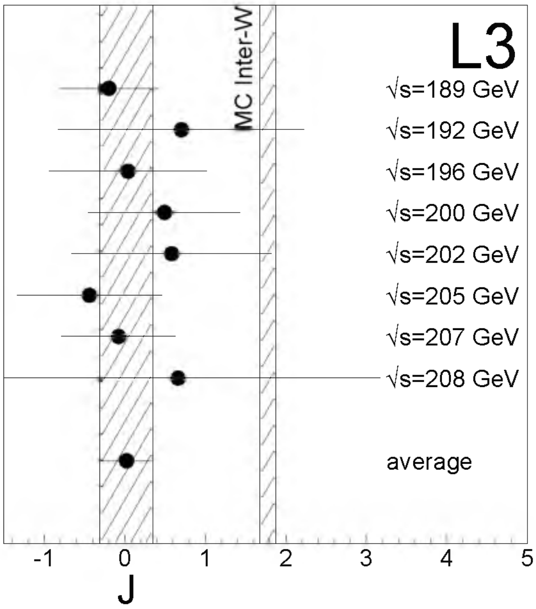

Figure 4.17: Values of the integral $J(\pm,\pm)$ found at the different energy bins. The errors are statistical only, including bin-to-bin correlations. Also shown is the MC prediction of KORALW (at the detector level) with BEC between all particles (BEA).

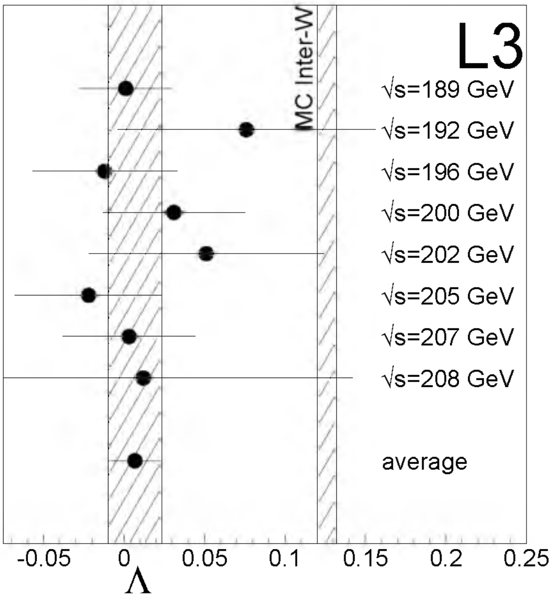

Figure 4.18: Values of the $\Lambda$ parameter found at the different energy bins. The errors are statistical only, including bin-to-bin correlations. Also shown is the MC prediction of KORALW (at the detector level) with BEC between all particles (BEA).

BES, so that the difference between $D$ and $D'$ is small, which supports the validity of the mixing procedure and the model independent analysis of $D$.

To estimate the strength of inter-W BEC, the $D'(\pm,\pm)$ distribution is fitted (from 0 to 1.4 GeV) by the following function

$$D'(Q) = (1+\epsilon Q)\left(1+\Lambda \exp(-k^2Q^2)\right) \quad , \tag{4.31}$$

where $\epsilon$, $\Lambda$ and $k$ are the fit parameters. The results of $\Lambda$ for each energy bin are given in table 4.4. In the last two rows of the table the results of two MC scenarios are given: KORALW with BEA (inter-W) and BES (no inter-W), both after simulation, reconstruction and WW selection. The result of the fit for the strength of $\Lambda$ when the fit results of all the energy bins are combined, is

$$\Lambda = 0.007 \pm 0.017 \pm 0.016 \quad .$$

The fit result after all the data of the different energy bins are combined, yields ($\chi^2/\mathrm{NDF} = 32/32$)

$$\Lambda = 0.008 \pm 0.018 \pm 0.016 \quad ,$$

where the first error is statistical and the second systematic. The statistical error includes bin-to-bin correlations that are estimated by using the full covariance matrix in the fit (see subsection 4.7.3). The value of $\Lambda$ is consistent with zero, i.e., with no inter-W BEC. For the estimation of the systematic uncertainty I refer to subsection 4.7.4. The value of $k$ is found to be $0.4 \pm 0.4 \pm 0.3$ fm and the correlation coefficient between $\Lambda$ and $k$ is found to be 0.45.

The results of $\Lambda$ for each energy bin are also shown in fig. 4.18. The errors are statistical only, taking into account bin-to-bin correlations. From fig. 4.18 one can conclude that the results are consistent with each other and with zero. A fit was also performed for the KORALW BEA distribution, resulting in $\Lambda = 0.126 \pm 0.008$ (statistical error only). In fig. 4.18 this value is shown as a vertical band. The data disagree with this value by 4.7 standard deviations.

### 4.7.3 Bin-to-Bin Correlations

As in subsection 4.5.1, where bin-to-bin correlations are estimated for the BE correlation function, bin-to-bin correlations are also taken into account when computing the integral (4.30) and when performing the fit (4.31) to extract the $\Lambda$ parameter.

Bin-to-bin correlations are included in the statistical error on the value of the integral $J$ by dividing the $\Delta\rho$ distribution into two bins: the first bin corresponding to the integration region ($0 < Q \leq 0.68\,\text{GeV}$), the second bin to the non-integration region ($Q > 0.68\,\text{GeV}$). The corresponding $2 \times 2$ covariance matrix is computed and the first diagonal element of this matrix estimates the statistical error on the value of the integral $J$, including the effect of bin-to-bin correlations in this first bin. This result has been checked by generating 100 sets of WW events, using PYTHIA, with the same statistics as the data and calculating the integral value $J$ for each of these sets, in the same way as explained above. The variation of $J$ from its average value is determined and the Gaussian width is found to be consistent with the statistical error computed directly from the data.

The covariance matrix for $D'$, normalized to its diagonal elements, is given in fig. 4.19, for the 189 GeV data. Both a lego plot and a contour plot are shown. Similar results, but with larger statistical fluctuations, are obtained for the other energy bins. It is clear that bin-to-bin correlations exist and that they vary from a few percent (at low $Q$) to 30% (at $Q$ values around 0.5 GeV). The effect of using the full covariance matrix in the fit, i.e., minimizing the $\chi^2$, eqn. (4.26), where the full covariance matrix of $D'$ is used, is that the statistical error on $\Lambda$ is about 20% larger than when only the diagonal elements are used. It is approximately 80% larger than when the assumption is made that the number of entries in each bin of $Q$ is Poisson distributed. From these results the importance of using the full covariance matrix is obvious. Also for the computation of the statistical error on $\Lambda$, MC studies have been performed as a cross check. For 100 sets of generated WW events, using PYTHIA, with the same statistics as the data, $\Lambda$ is computed and the variation from its average value is determined. The Gaussian width is found to be consistent with the statistical error computed directly from the data.

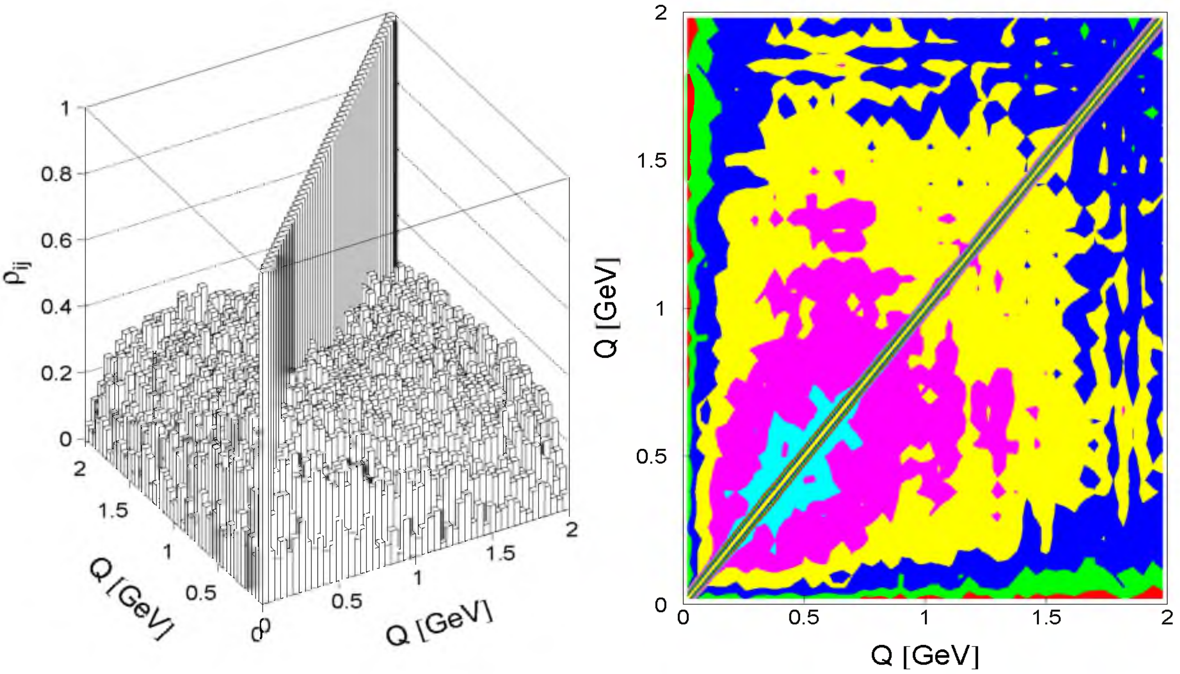

Figure 4.19: The normalized covariance matrix for the $Q$ distribution for the ratio $D'$ at 189 GeV. A lego plot is shown left, a contour plot is shown right.

### 4.7.4 Systematic Uncertainties

The systematic uncertainties on $J(\pm,\pm)$ and $J(+,-)$, eqn. (4.30), and on $\Lambda$, are given by the sums in quadrature of the contributions listed in table 4.5 and table 4.6, respectively.

The amount of background was varied by ±20%. The track and event selections were varied: both stronger and weaker cuts were applied to tracks (i.e., cuts on the number of hits, span, distance of closest approach and transverse momentum were varied) and slightly different event selections were made. The maximum deviation that is found by varying each selection criterion, keeping the other cuts on their standard values, is taken as the contribution to the systematic error of the measurement due to this cut. Furthermore, contributions to the systematic uncertainty on $\Lambda$ are obtained by varying the choice of MC for the reference sample in $D'$, using PYTHIA and KORALW, both with no BEC at all, as well as with only intra-W BEC. Also the effect of various models for colour reconnection [1] (CR) was included. A change in the fit range (±0.4 GeV), a change in the bin size (from 40 to 80 MeV) and a change in the parametrization (removing the factor $(1+\epsilon Q)$ from the fit (4.31)) also give contributions to the systematic uncertainty on $\Lambda$.

In the mixing procedure, a semi-hadronic WW event is allowed to be combined with all possible other semi-hadronic WW events. To be sure that this does not introduce a bias,

---

[1] The so-called SKI, SKII, SKII' [74] and GH [75] models, as implemented in PYTHIA, were used.

the analysis was repeated for a mixed sample where every semi-hadronic event was used at most once. The influence of the mixing procedure was also studied by not only combining oppositely charged W's, but also like-sign W's. The influence of the extra momentum $\vec{p}_{\text{extra}}$, used in the event mixing, is also included as a systematic effect. The RMS of the systematic uncertainties due to these three changes in the mixing procedure is computed for both the $J$ values and the $\Lambda$ parameter. Moreover, the influence of the cut on the neural network output for the mixed events was investigated by removing the cut.

Furthermore, the effect of uncertainties in the energy calibration of the calorimeters was studied. Finally, the influence of the $\mathrm{q\bar{q}}\tau\bar{\nu}$ channel was investigated. Since this channel is the most difficult to identify, and therefore has relatively high background and low efficiency, the analysis was repeated without it.

In both tables 4.5 and 4.6 the systematic uncertainties of the different sources are shown when the energy bins are combined. No significant differences are observed between these uncertainties in the different energy bins. However, some uncertainties are highly correlated, i.e., show the same behaviour when variations are made on a certain cut. These correlated uncertainties are labelled with a * in tables 4.5 and 4.6. The other systematic uncertainties are highly uncorrelated. The 207 and 208 GeV energy bins are taken together to compute the systematic uncertainties, since the statistics of the 208 GeV data is so poor that it becomes difficult to estimate systematic effects without including any statistical components.

Table 4.5: Contribution to the systematic error of $J(\pm,\pm)$ and $J(+,-)$, eqn. (4.30). Explanation of the sources are in the text. Sources labelled with a * are highly correlated between the different energy bins.

| source | contr. to $J(\pm,\pm)$ | contr. to $J(+,-)$ |
|---|---|---|
| background contribution* | 0.055 | 0.049 |
| change track selection* | 0.140 | 0.153 |
| change event selection | 0.068 | 0.066 |
| change mixing | 0.065 | 0.064 |
| neural net output cut | 0.038 | 0.039 |
| energy calibration uncertainties | 0.024 | 0.021 |
| influence $\tau$ channel* | 0.151 | 0.164 |
| total systematic error | 0.24 | 0.25 |

## 4.8 Analyses with Increased Sensitivity

To make the analysis possibly more sensitive to inter-W BEC, the analysis is repeated three times using different selections to increase the overlap of the $\mathrm{W}^+$ and $\mathrm{W}^-$ decay products, i.e., increase $F(Q)$, eqn. (4.13), at low $Q$ values:

Table 4.6: Contribution to the systematic error of the $\Lambda$ parameter. Explanation of the sources are in the text. Sources labelled with a * are highly correlated between the different energy bins.

| source | contribution |
|---|---|
| background contribution* | 0.0042 |
| other Monte Carlo (PYTHIA, BES or no BE) | 0.0060 |
| allowing CR in the reference | 0.0026 |
| changing fit range | 0.0018 |
| rebinning (40 → 80 MeV) | 0.0020 |
| removing $(1+\epsilon Q)$ from the fit | 0.0017 |
| change track selection* | 0.0071 |
| change event selection | 0.0049 |
| change mixing | 0.0044 |
| neural net output cut | 0.0033 |
| energy calibration uncertainties | 0.0017 |
| influence $\tau$ channel* | 0.0072 |
| total systematic error | 0.016 |

- Since BEC occur mainly among soft particles and the overlap is expected to be larger for these particles than for high-momentum ones, the analysis is repeated using only tracks with momentum smaller than 1.5 GeV.

- Requiring that jets from different W's be close together is another way to increase the overlap. Therefore, the analysis is repeated requiring that the average of the smallest two of the four angles between jets from different W's (after jet finding and best pairing) be less than 75°. This results in a reduction of approximately 60% of the fully hadronic WW events.

- Applying a cut in the two-dimensional distribution of the opening angle between two like-sign tracks, $\delta\alpha$, and $Q$, is a third way to increase the overlap [2]. Inter-W pairs with low $Q$ values are more likely to have larger opening angles, with respect to intra-W pairs. This is shown in fig. 4.20 where the two-dimensional distribution is shown for inter-W pairs, computed from the event mixing procedure, and for intra-W pairs, computed from semi-hadronic WW events. KORALW without BEC (at the detector level) is used to compute the distributions. Only pairs with $\delta\alpha > 50Q$ are accepted, which increases the fraction of inter-W pairs by approximately 40% in the region up to 0.6 GeV, with respect to the inclusive sample.

Fig. 4.21 shows the distributions of $D'(\pm,\pm)$, eqn. (4.19), for these three analyses, for the raw data. The BES scenario of KORALW is used as the reference sample. Also shown

---

[2] N. van Remortel, whose idea this is, is being thanked for his useful discussions on this point.

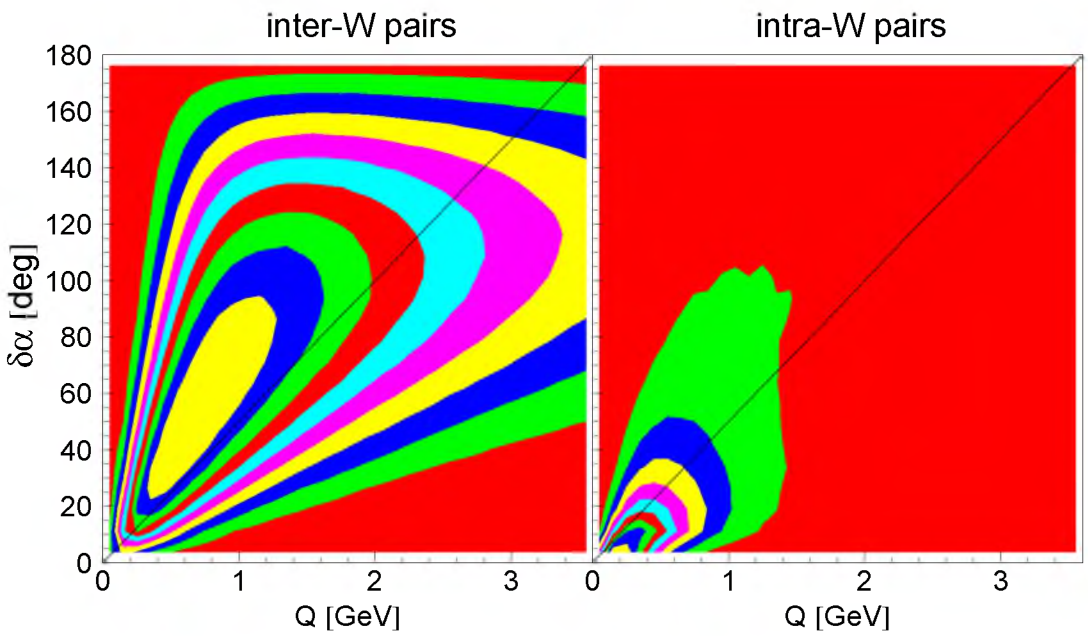

Figure 4.20: Two-dimensional distributions of the opening angle between two like-sign tracks, $\delta\alpha$, and $Q$, for inter-W pairs (left), computed from the event mixing procedure, and for intra-W pairs (right), computed from semi-hadronic WW events. KORALW without BEC (at the detector level) is used to compute the distributions. The diagonal lines show the cut.

in the figure are the predictions of KORALW for the scenarios BEA and BES. It is again clear that the BEA scenario is greatly disfavoured, while BES describes the data, which are still around unity.

The following values for $\Lambda$ are found: $\Lambda = 0.017 \pm 0.023$ for the low-momentum sample, $\Lambda = -0.008 \pm 0.025$ for the sample with the angular cut between jets and $\Lambda = 0.028 \pm 0.030$ for the sample with the $\delta\alpha > 50Q$ cut. All three values are consistent with zero. The errors here are statistical only and include bin-to-bin correlations.

From fig. 4.21 it is clear that, for all three sensitivity analyses, the BEA prediction deviates more from the BES prediction, than when the inclusive sample, see, e.g., fig. 4.16, is considered. E.g., the value of $\Lambda$, see eqn. (4.31), is found to be in the range 0.166-0.203, depending on the selection, which is clearly above the result of the inclusive sample ($0.126 \pm 0.008$). However, at low $Q$ the statistical errors on the data points increase by 30 to 65%, depending on the selection, with respect to the inclusive sample. Consequently, the gain in sensitivity is lost by the reduction of the statistics.

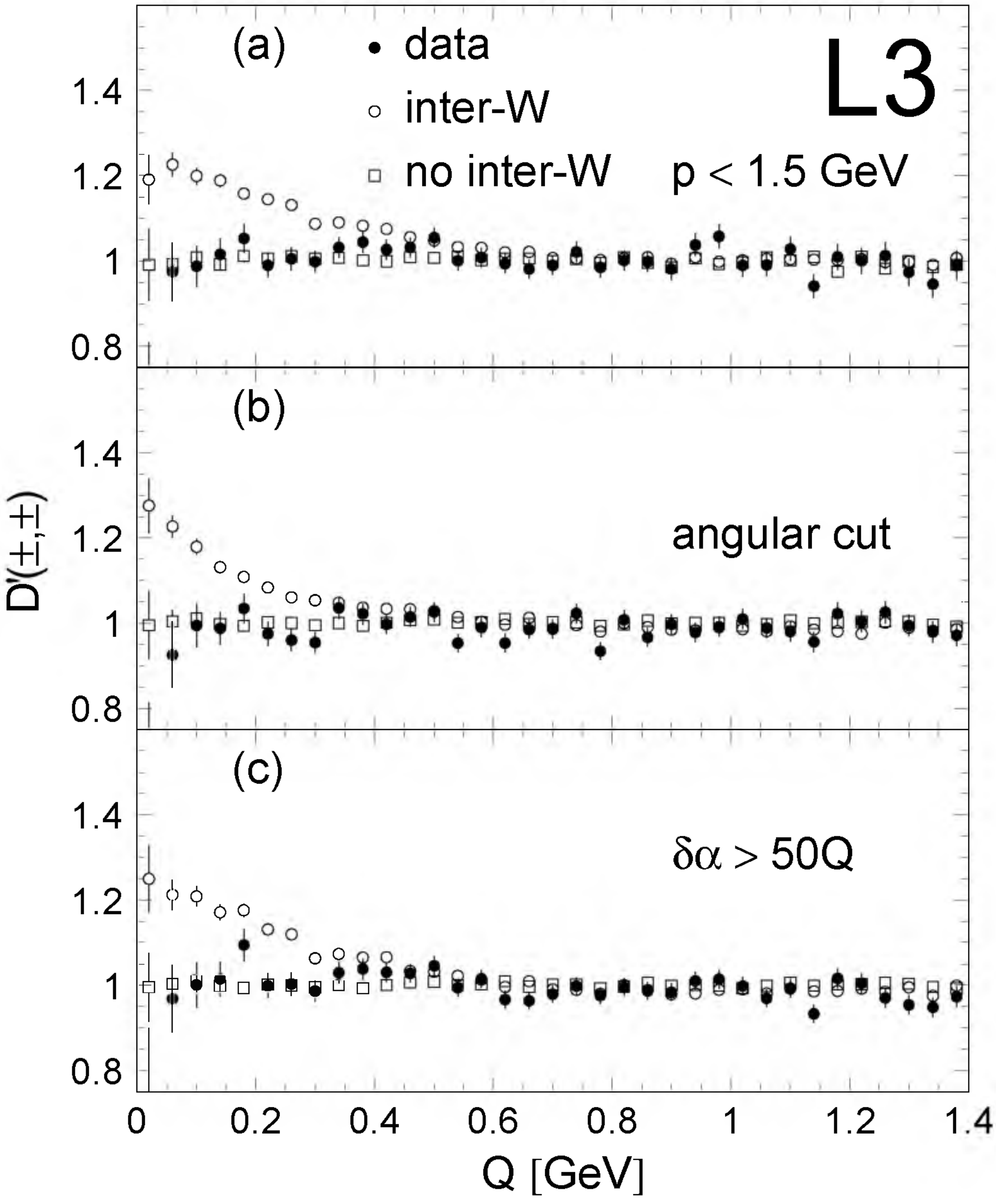

Figure 4.21: Double ratio distribution, $D'(\pm,\pm)$, for the three sensitivity analyses: for the low-momentum sample, (a), for the sample with the angular cut between jets, (b), and for the sample with the $\delta\alpha > 50Q$ cut, (c). Also shown are the MC predictions of KORALW (at the detector level) with BEA (inter-W) and BES (no inter-W).

## 4.9 Comparison with other LEP experiments

Also the other LEP collaborations have done BE analyses in WW events, and in particular inter-W BE analyses. The results, some of which are based on different methods, are consistent with the result of L3.

The result of the ALEPH analysis [91, 92] is that BEC are observed in semi-hadronic W-pair decays and are described by a JETSET model which is tuned and corrected at the Z resonance for light-quark flavours. The same model describes BEC in the fully hadronic WW channel when only intra-W BEC are allowed and disfavours the scenario with inter-W BEC at the level of 2.7 standard deviations [91], when almost all LEP2 data up to 189 GeV are used. Preliminary results including the data up to 202 GeV, again show an agreement when only intra-W BEC are used in the model. However, the discrepancy with the model including inter-W BEC has decreased to 2.2 standard deviations [92]. The latest studies performed by the ALEPH collaboration make use of the same formalism as given in this work. Although no quantitative results are given, qualitatively they are consistent with no inter-W BEC [92, 93]: The data show flat distributions for $\Delta\rho(Q)$ and $D(Q)$. A MC model with inter-W BEC shows a clear enhancement in these distributions and is disfavoured.

Preliminary results from OPAL [94], using almost all LEP2 data up to 189 GeV, are inconclusive due to lack of statistics, so far. Three event samples are studied by OPAL, each dominated by one of the processes $\mathrm{WW} \rightarrow \mathrm{q\bar{q}}\ell\bar{\nu}$, $\mathrm{WW} \rightarrow \mathrm{q\bar{q}q\bar{q}}$ or $\mathrm{Z} \rightarrow \mathrm{q\bar{q}}(\gamma)$. In a simultaneous fit, BE correlation parameters are determined for pions originating from the same and from different W's, as well as for pions from $\mathrm{Z}/\gamma \rightarrow \mathrm{q\bar{q}}(\gamma)$ events. The result is that different MC models (with or without inter-W BEC) describe the three event samples.

Using the same formalism as given in this work, preliminary results of the DELPHI collaboration [95] do not give any indication for the existence of inter-W BEC. In particular, a fit is performed on the single ratio distribution, $D(Q)$, using the parametrization $\gamma(1+\delta Q)(1+\Lambda\exp(-kQ))$. Fixing $k$ to 1.01 fm (fit result for the BEA scenario), results in $\Lambda = -0.037 \pm 0.055 \pm 0.055$, and the BEA scenario according to the $\mathrm{BE}_{32}$ model is disfavoured by 3.2 standard deviations.

Thus, measurements on the (non-)existence of inter-W BEC done by other LEP experiments, give results consistent with what is found in this analysis: no evidence is found for the existence of inter-W BEC.

## 4.10 Interpretation and Discussion of the Results

Intra-W BEC have been found to be similar to those observed in Z decay to light quarks. In addition, an excess at small values of $Q$ in the distributions of $\Delta\rho(\pm,\pm)$, $D(\pm,\pm)$ and $D'(\pm,\pm)$ is expected from inter-W BEC, but none is seen, even when the analysis is made more sensitive to inter-W BEC. These distributions agree well with KORALW using $\mathrm{BE}_{32}$ when inter-W BEC are not included, but not when they are. Thus, no evidence is found for BEC between identical pions originating from different W's and its implementation using the $\mathrm{BE}_{32}$ and $\mathrm{BE}_0$ algorithms is disfavoured.

### 4.10.1 Effect on the W Mass Measurement

The positive outcome of the analysis in this chapter, is that the effect on the W mass measurement due to inter-W BEC, is small. The reduction of the systematic uncertainty due to the effect of inter-W BEC is large. At the time that W production started at LEP2, the worst case scenario predicted an effect on the measurement of the W mass up to 100 MeV [23]. Before the results of this analysis, the L3 collaboration estimated the error to be 60 MeV [96]. After publication of the inter-W BEC analysis at $\sqrt{s} = 189\,\mathrm{GeV}$ [70], the error was reduced to 20 MeV [97, 98].

Since there is no alternative model available (at detector level and tuned to the data) besides LUBOEI to simulate BEC, the mass shift due to inter-W BEC is computed with this model [99]. For simplicity we assume that $\Lambda$, see eqn. (4.31), is linearly proportional to the inter-W BEC and that the input parameter $\lambda$ in the MC (i.e., PARJ(92), see subsection 1.4.2), is also linearly proportional to the inter-W BEC and to the mass shift. The mass shift due to intra-W BEC appears to be $6 \pm 12\,\mathrm{MeV}$ [99], consistent with zero. Uncertainties in the simulation of these correlations are part of the fragmentation and hadronization uncertainties. When $\mathrm{BE}_{32}$ with inter-W BEC is used (with the tuned parameter values PARJ(92)=1.68 and PARJ(93)=0.38 GeV) at $\sqrt{s} = 189\,\mathrm{GeV}$, the mass shift is found to be $56 \pm 12\,\mathrm{MeV}$ [99]. The result of the analysis in this chapter is that this MC is disfavoured by approximately 4.7 standard deviations. From this we can estimate an upper limit mass shift of $56\,\mathrm{MeV}/4.7 \simeq 12\,\mathrm{MeV}$. The final estimation of the systematic error on the W mass measurement due to inter-W BEC, is still ongoing. It is likely that combining the results of the four LEP experiments will reduce the upper limit below 10 MeV.

### 4.10.2 Why No Inter-W Bose-Einstein Correlations?

However, even more importantly from a physics point of view, the question arises why no such inter-W BEC are observed. In the following, an interpretation of this result will be given in the form of a discussion, i.e., only *possible* reasons are given why no inter-W BEC are observed. In the discussion, experimental and theoretical arguments are given.

Firstly, it needs to be emphasized that it is not claimed here that inter-W BEC do not exist at all. The non-zero errors on the result still leave room for (weak) inter-W BEC. So, two hypotheses will be discussed: 1. inter-W BEC *do* exist, 2. inter-W BEC do *not* exist. In these two hypotheses we have to ask why inter-W BEC do, or do not, exist, respectively. For the first hypothesis we even need to add the question: "Why then do we not see inter-W BEC"?

The case that no inter-W BEC exist, is consistent with the expectations of the Lund string model [38, 39]. In this model, the confining colour field is approximated by a massless relativistic string. The endpoints of the string are identified with quark and antiquark properties, while the gluons are assumed to behave as transverse excitations on the string. The string can break up into smaller pieces by the production of $\mathrm{q\bar{q}}$ pairs (i.e., new endpoints). The basic result of this model is the Lund area law, which describes the production probability of a set of hadrons with certain four-momenta, in terms of the area $A$ of the string before the decay, i.e., before the hadrons are formed, in space-time. The negative exponential, $\exp(-bA)$, of this area is related to the squared matrix element (as in Fermi's Golden rule): $\mathcal{M} = \exp(i\xi A)$ with $\mathrm{Re}(\xi) = \kappa$ being the string tension and $\mathrm{Im}(\xi) = b/2$ being half of the correlation length in rapidity. If there are identical bosons, then the matrix element has to be symmetrized before it is squared. The area $A_{12}$ is not equal to the area $A_{21}$, where the two identical particles are interchanged. Therefore, a phase difference $\Delta A = |A_{12} - A_{21}|$ appears, leading to

$$R_2 \simeq 1 + \cos(\kappa \Delta A)/\cosh(b\Delta A/2) \quad . \tag{4.32}$$

In the limit of $Q = 0$, $\Delta A = 0$ and $R_2 = 2$, in agreement with the results from the conventional interpretation for a completely incoherent source.

Important is that the model starts with one string where the endpoints are identified with a quark and an antiquark, e.g., those originating from a hadronically decaying W. If two strings are considered, e.g., two W's decaying hadronically at LEP2, then the production probability of a set of hadrons with certain four-momenta is computed for each system separately. Thus, in the Lund string model as it stands there is no need for cross-talk: the strings are independent from each other, as long as there is no colour reconnection.

However, in [100] it is argued that BEC, as they were conceived in astronomy, are different from BEC observed in high-energy collisions, but that the former kind of correlations *may* occur between two sources that are uncorrelated in colour, even in the framework of the Lund string model. The argument states that BEC, as they were conceived in astronomy, are based upon the incoherence between the radiation emitted from different sources, whereas no such incoherence has to exist in pion emission from a single source. This last statement is supported by Low's theorem [100] that predicts photons with long wave-length to be emitted coherently from a small hadronic production region, and by the experimental observations (at least for photons with wave-length between 0.2 and 2 fm) that agree with this prediction. In the Lund string model, hadrons are produced coherently within a string, and BEC are predicted (as a consequence of the Lund area law). But then the origin of these correlations is different from that of the correlations observed in astronomy. On the other hand, in systems where the particle production stems from two or more independent sources, e.g., as seems to be the case for the two hadronically decaying W's at LEP2, there could well be an additional phenomenon similar to the "original" BE phenomenon, as observed in astronomy.

In [101], a one-to-one correspondence, in terms of interferometry of binary sources, is made between stellar astronomy and high energy physics: oscillations are observed due to BE interference between photons emitted from a binary star system in stellar astronomy [102] (as observed by Hanbury Brown and Twiss), similar to the oscillations which might be expected in particle interferometry between the hadronically decaying W's at LEP2. In the binary source formalism, an oscillating pre-factor, $\Omega(Q)$, is expected in the cumulant correlation function $C_2(Q)$ $(= R_2(Q) - 1)$. This factor is given by [101]

$$\Omega(Q) = f_+^2 + f_-^2 + 2f_+f_- \cos\left[Q(x_+ - x_-)\right] \quad , \tag{4.33}$$

where $f_\pm$ is the fraction of emission from a source, e.g., from $W^\pm$, which is centred at space-time point $x_\pm$. The strength of the oscillations is controlled by the relative strength of emission from the displaced sources and the period of oscillation is a measure for the distance between the two emitters. In the limit of only one emitter, $f_\pm = 1$ and $f_\mp = 0$, the oscillations disappear and $\Omega(Q) = 1$. Using eqn. (4.1), the distance between the $W^+W^-$ decay vertices is estimated to be 0.12 fm (at $\sqrt{s} = 189\,\text{GeV}$). From this, one can conclude that the period of oscillation is large enough to become observable. However, the data do not show oscillating behaviour in any of the energy bins, at the level of statistics that was used in the analysis.

An experimental reason why no inter-W BEC are observed (if they do exist), may be that the fraction of pairs, where one particle comes from $W^+$ and the other particle from $W^-$, is small for low values of $Q$ (see, e.g., fig. 4.11). There might be too many pairs coming from the same W (intra-W pairs), to make inter-W BEC visible. Attempts are made in section 4.8 to increase this fraction, but this might still be too small to observe inter-W BEC. Moreover, MC studies show that only around 64% of the particle pairs are pion pairs, which further reduces the sensitivity of the analysis. Unfortunately, there is no good hadron identification possible with the L3 detector.

In model comparisons, the observation is made that the models with the $BE_{32}$ (or $BE_0$) implementation are strongly disfavoured when inter-W BEC are taken into account, see, e.g., figs. 4.14 and 4.16. The outcome of these model comparisons is only to be used to exclude them from further analyses, e.g., in the estimation of the systematic uncertainty on the W mass measurement. On the level of inter-W BEC, no predictive power should be given to these models, since the implementation of BEC is done in an unacceptable way: it has no quantum mechanical basis and it is implemented in an ad hoc way by shuffling the momenta of particles in such a way that a correlation effect is imitated. That is the reason why inter-W BEC still might exist, although they seem to be excluded when the data are compared with the predictions of KORALW with the $BE_{32}$ (or $BE_0$) implementation when inter-W BEC are allowed.

A reason why the effect of inter-W BEC could be very small, is that the overlap in space-time of the hadron production regions of the two hadronically decaying W's might be smaller than expected from the above models. In chapter 3, the region of homogeneity of hadronic Z decay is found to be elongated along the thrust axis. The amount of overlap between two hadronically decaying W systems will therefore be less than when spherical symmetry of the region of homogeneity was observed. Moreover, the analysis in chapter 3 does not give information on what part is measured from the total space-time region where the production of hadrons take place, and on whether the production is uniformly distributed in this space-time region, or, e.g., more concentrated at the edge of this region, as it is observed in hadron-hadron collisions [103]. All this information would give insight into the actual amount of overlap between two hadronically decaying systems. Experimental work is indeed going on at the Z resonance, but including the available information into a more exact modelling of the overlap will be important.

# Chapter 5

# Three-Particle Bose-Einstein Correlations in Hadronic Z decays

So far in this thesis, only two-particle correlations have been considered. Additional information, not present in two-particle correlations, can be derived from higher-order correlations. Furthermore, higher-order correlations constitute an important theoretical issue for the understanding of Bose-Einstein correlations (BEC) [32], themselves.

In this chapter, three-particle correlations are analysed. These correlations are sensitive to asymmetries in the particle source shape which cannot be studied by two-particle correlations. More importantly, by combining two- and three- particle correlation analyses, one can investigate the degree of coherence of pion production. From two-particle correlations alone this is very difficult due to (long-lived) resonances which affect the correlation function, and also due to the poor resolution of the detector to measure particles with almost the same momenta. Furthermore, higher-order correlations are of crucial importance for much of the search for scaling phenomena in multiparticle processes [34]. Studies of (higher-order) correlations at high energies are thus related to the composition of jets and test of QCD models.

The outline of this chapter is as follows. Firstly, the theoretical background of the analysis is shown. Secondly, the data selection is given, including the three-track resolution. Then, it is shown how the relevant distributions of this analysis are determined experimentally. The results are given in section 5.4, after which an overview of systematic uncertainties is given. Finally, a comparison is made with JETSET MC predictions and the conclusions are summarized and compared with results of other experiments.

It may be noted that part of this chapter shows similarities with chapter 3. Especially, the event and track selection and the way correlation functions are determined are in many aspects the same.

## 5.1 The Analysis

In this section, the theoretical background for this analysis is repeated and extended with respect to subsection 1.3.3.

In general, the three-particle correlation function of particles with momenta $p_1, p_2$ and $p_3$ is defined in nine-dimensional momentum space as

$$R_3'(p_1,p_2,p_3) \equiv \frac{\rho_3(p_1,p_2,p_3)}{\rho_1(p_1)\rho_1(p_2)\rho_1(p_3)} \quad , \tag{5.1}$$

where $\rho_3(p_1,p_2,p_3)$ is the three-particle number density and $\rho_1(p_1)\rho_1(p_2)\rho_1(p_3)$ is the product of three single-particle densities. The density $\rho_3(p_1,p_2,p_3)$ can be described in terms of single-particle, two-particle and genuine three-particle densities as (see also eqns. A.6-A.8 of Appendix A)

$$\rho_3(p_1,p_2,p_3) = \rho_1(p_1)\rho_1(p_2)\rho_1(p_3) + \sum_{(3)} \left[\rho_1(p_1)\left(\rho_2(p_2,p_3) - \rho_1(p_2)\rho_1(p_3)\right)\right] + C_3(p_1,p_2,p_3) \quad , \tag{5.2}$$

where the sum is over the three possible permutations and where $C_3$ is the third-order cumulant measuring the genuine three-particle correlations. The $\rho_1\rho_2$ terms contain all the two-particle correlations. Since we are interested here only in the correlation function $R_3$ due to BE interference, the product of single-particle densities is replaced by $\rho_{0,3}(p_1,p_2,p_3)$, the three-particle density that would occur in the absence of BEC:

$$R_3(p_1,p_2,p_3) \equiv \frac{\rho_3(p_1,p_2,p_3)}{\rho_{0,3}(p_1,p_2,p_3)} \quad . \tag{5.3}$$

The kinematical variable $Q_3$ is used to study three-particle correlations. For a three-pion system, $Q_3 = \sqrt{M_{123}^2 - 9m_\pi^2}$, with $M_{123}$ the invariant mass of the pion triplet and $m_\pi$ the mass of the pion. In this chapter, $\rho_3$ is defined as

$$\rho_3(Q_3) \equiv \frac{1}{N_{\mathrm{ev}}} \frac{\mathrm{d}n_{\mathrm{triplets}}}{\mathrm{d}Q_3} \quad , \tag{5.4}$$

with $N_{\mathrm{ev}}$ the number of events that is used and $n_{\mathrm{triplets}}$ being the number of triplets of like-sign tracks.

Assuming totally incoherent production of particles and a source density $f(x)$ in space-time, with no energy-momentum dependence, we are able to write the three-particle BE correlation function as [35]

$$R_3(Q_{12},Q_{13},Q_{23}) = 1 + |G(Q_{12})|^2 + |G(Q_{13})|^2 + |G(Q_{23})|^2 + 2\mathrm{Re}\{G(Q_{12})G(Q_{13})G(Q_{23})\} \quad , \tag{5.5}$$

where

$$G(Q_{ij}) = \int \mathrm{d}x \exp(iQ_{ij}x) f(x) \tag{5.6}$$

is the Fourier transform of $f(x)$, which can be derived from the two-particle BE correlation function $R_2$ via

$$R_2(Q_{ij}) = 1 + |G(Q_{ij})|^2 \quad . \tag{5.7}$$

Thus, $R_2 - 1$ is related to the space-time particle density through a Fourier transformation [4, 13]. The genuine three-particle BE correlation function therefore reads

$$R_3^{\text{genuine}}(Q_{12}, Q_{13}, Q_{23}) = 1 + 2\text{Re}\{G(Q_{12})G(Q_{13})G(Q_{23})\} \quad . \tag{5.8}$$

In general, the production of particles is not completely incoherent. A first measurement of the fraction of coherence can be obtained from the measured strength of the two- and three-particle BE correlation function, $R_2(0)-1$ and $R_3(0)-1$ [104]. The measured strength is an extrapolation since the available phase space diminishes considerably for two particles when $Q_{ij} \to 0$ and experimentally we are not able to resolve two particles when $Q_{ij} \to 0$. A deviation of the measured intercept parameter $R_2(0) - 1$ from unity can be due to particles from (long-lived) resonances which contribute at very low $Q_{ij}$, $\mathcal{O}(10)$ MeV [21], not resolvable by the detector, and/or a (partially) coherent particle emitting source. In [104] the following expressions are derived for the intercept parameters, $R_2(0) - 1$ and $R_3(0) - 1$:

$$\lambda \equiv R_2(0) - 1 = f_c^2 \left[(1-p_c)^2 + 2p_c(1-p_c)\right] \quad , \tag{5.9}$$

$$\lambda_3 \equiv R_3(0) - 1 = 3f_c^2 \left[(1-p_c)^2 + 2p_c(1-p_c)\right] + 2f_c^3 \left[(1-p_c)^3 + 3p_c(1-p_c)^2\right] \quad , \tag{5.10}$$

where $f_c$ is the fraction of particles coming from the centre of particle emission that is assumed to be resolvable by the BE microscope ("core" fraction) and $p_c$ the fraction of the core that emits the particles in a coherent manner. Thus, from $\lambda$ and $\lambda_3$, one can extract a region of values for $f_c$ and $p_c$ that fulfil eqns. (5.9) and (5.10). A disadvantage of this measurement is that it does not use the information of the width of the correlation function.

Therefore, not only the intercept, but the $Q_3$ dependence of the genuine three-particle BE correlation function, eqn. (5.8), is analysed. When the production of pions is not completely incoherent and/or $f(x)$ not symmetric, the Fourier transform $G(Q_{ij})$, eqn. (5.6), is complex, $G \to G\exp(i\phi_{ij})$. The phase factor, $\exp(i\phi_{ij})$, cancels in the two-particle BE correlation function, eqn. (5.7), but survives in the three-particle BE correlation function as seen from eqn. (5.5). In fact, from eqn. (5.8), using $\phi \equiv \phi_{12} + \phi_{13} + \phi_{23}$, we find

$$\cos\phi = \frac{R_3^{\text{genuine}}(Q_{12}, Q_{13}, Q_{23}) - 1}{2\sqrt{(R_2(Q_{12}) - 1)(R_2(Q_{13}) - 1)(R_2(Q_{23}) - 1)}} \quad , \tag{5.11}$$

which is a function of $Q_{ij}$. In particular, due to the normalization, $\cos\phi \to 1$ when all $Q_{ij} \to 0$. The phase factor $\cos\phi$ differs from unity, either because the source is asymmetric or because the emission is (partially) coherent. However, asymmetry in the production mechanism will only result in a small (a few percent) reduction of $\cos\phi$ [33, 36], and this only in the case where the asymmetry occurs around the point of highest emissivity. It is important to note that eqn. (5.5) is *not* valid for partially coherent sources, in which case complicated expressions are needed [36]. We can always define $\cos\phi$ by eqn. (5.11), but $\cos\phi$ has a defined meaning as a phase factor only for incoherent sources. If $\cos\phi$ differs from one, we can infer that partial coherence is present, but $\cos\phi$ does not measure directly the fraction of pions produced incoherently.

In the special case where $f(x)$ is Gaussian, and to the extent that phase factors may be neglected, i.e., assuming a completely incoherent production of particles and a symmetric source density function, or $\cos\phi = 1$, $R_3^{\text{genuine}}$ is related to $R_2$ via

$$R_3^{\text{genuine}}(Q_3^2) - 1 = 2\sqrt{R_2(Q_3^2) - 1} \quad , \tag{5.12}$$

depending only on $Q_3^2$. A deviation from this equation reveals new information not present in two-particle BE correlations, namely information related to the (in)coherence and/or (a)symmetry of the source.

## 5.2 Event and Track Selection

The data used in this analysis were collected by the L3 detector in 1994 at a centre-of-mass energy of $\sqrt{s} \simeq 91.2\,\text{GeV}$. The data selection uses information on charged particles from the Time Expansion Chamber (TEC) and the Silicon Microvertex Detector (SMD) [44], and is identical to that presented in section 3.2, apart from two additional cuts.

For the computation of three-particle correlations, each possible triplet of like-sign tracks is used to compute the kinematical variable $Q_3 \equiv \sqrt{Q_{12}^2 + Q_{13}^2 + Q_{23}^2}$, where $Q_{ij}$ ($i, j = 1, 2, 3$) is the four-momentum difference between particles $i$ and $j$. Thus, the resolution of the angle between pairs of tracks is of crucial importance, especially for small $Q_{ij}$ values. To reduce the dependence of detector correction on the MC model used (see section 5.3), tracks with measured momentum larger than 1 GeV are rejected, as are pairs of like-sign tracks whose opening angle is measured to be less than 3°.

Since $Q_{ij}$, and thus $Q_3$, depends both on the energy of the particles, as well as on the angle between them, small $Q_{ij}$ can be due to either small angles or low energies (or both). In a MC with BE effects, the fraction of pairs at small $Q_{ij}$ with small angle is larger than in a MC without BE effects. The limited ability of the detector to distinguish tracks that are close to each other, leads to a lower estimate of the detection efficiency. Consequently, there is a large model dependence on the measurement of three-particle correlations. The momentum and opening angle cuts reduce this model dependence. The efficiency to resolve two nearby tracks decreases when their momenta increase, since the bending of the tracks by the magnetic field is small for high momentum tracks, resulting in less room for the tracks to deviate from each other. In the region of interest, $Q_3 < 1\,\text{GeV}$, the loss of statistics by the momentum and opening angle cut is about 40%. The relative loss approaches zero for decreasing $Q_3$.

Another important effect of the momentum cut is that the resolution for $Q_3$ increases considerably with respect to the resolution using the inclusive momentum spectrum. The resolution for $Q_3$ is determined by computing $\delta Q_3 \equiv Q_3^{\text{det}} - Q_3^{\text{gen}}$ for each triplet of like-sign tracks, where $Q_3^{\rm det}$ is computed at detector level of MC and $Q_3^{\rm gen}$ the corresponding value at generator level. The distribution of $\delta Q_3$ found from 500k events generated by JETSET (with BE), is shown in fig. 5.1 before and after the momentum cut. Also shown in this figure is $\delta Q_3$ after the momentum cut and using only triplets of tracks with $Q_3 < 0.8\,\mathrm{MeV}$.

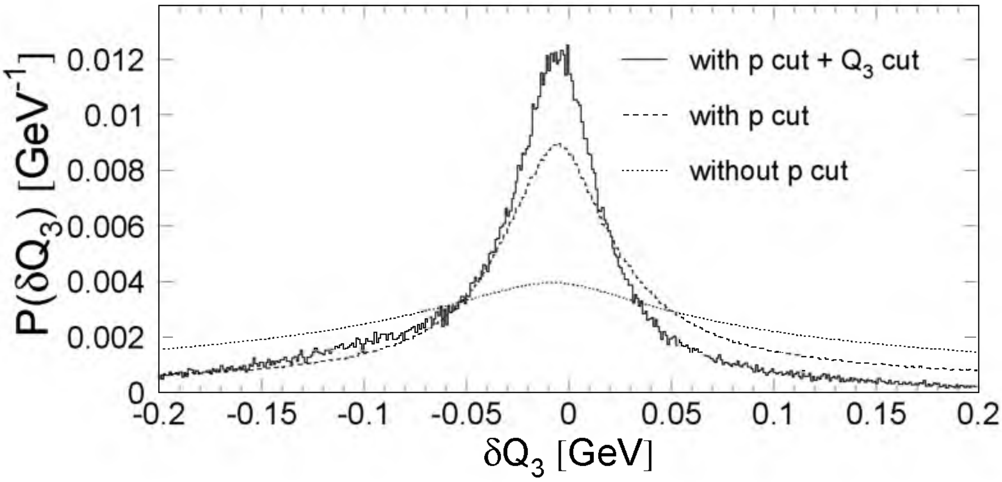

Figure 5.1: Resolution $\delta Q_3$, in GeV, of $Q_3$, between triplets of like-sign tracks according to JETSET, before the momentum cut (dotted histogram), after the momentum cut (dashed histogram) and after both the momentum cut and the cut on $Q_3$ (full histogram).

It is clear that the resolution is much better when the momentum cut is applied. The half-width at half-maximum, $H$, which is used as a characteristic of the resolution, is found to be $H \simeq 37\,\mathrm{MeV}$ when the momentum cut is applied and $H \simeq 26\,\mathrm{MeV}$ when both the momentum cut and the cut on $Q_3$ are applied. Note that the resolution for $Q_3$ improves further when applying a stronger cut on $Q_3$. Knowing this resolution, a bin-size of 40 MeV is chosen for the three-particle BE analysis.

Furthermore, we observe that the peak position of the $\delta Q_3$ distribution has a slightly negative value. There are two reasons for this feature. Firstly, due to finite momentum resolution, the momentum cut at 1 GeV at detector level, may result in momenta above 1 GeV at generator level. Secondly, at detector level MC all charged particles are assumed to be pions. At generator level MC, however, the generated mass of the particles is taken.

In fig. 5.2, the raw data are compared to JETSET (with and without BE effects) and HERWIG (not having a BE option) at the detector level, after performing all cuts, in the three-particle distributions $\sum \delta\phi$, $\sum \delta\theta$, and $Q_3$. The sums run over the three pairs of like-sign tracks in the triplet and $\delta\phi$ and $\delta\theta$ are the differences in azimuthal and polar angle between two like-sign tracks, respectively. The MC distributions are normalized to the total number of entries in the corresponding data distributions.

Within 10%, the angular distributions of the MCs agree with those of the data. None

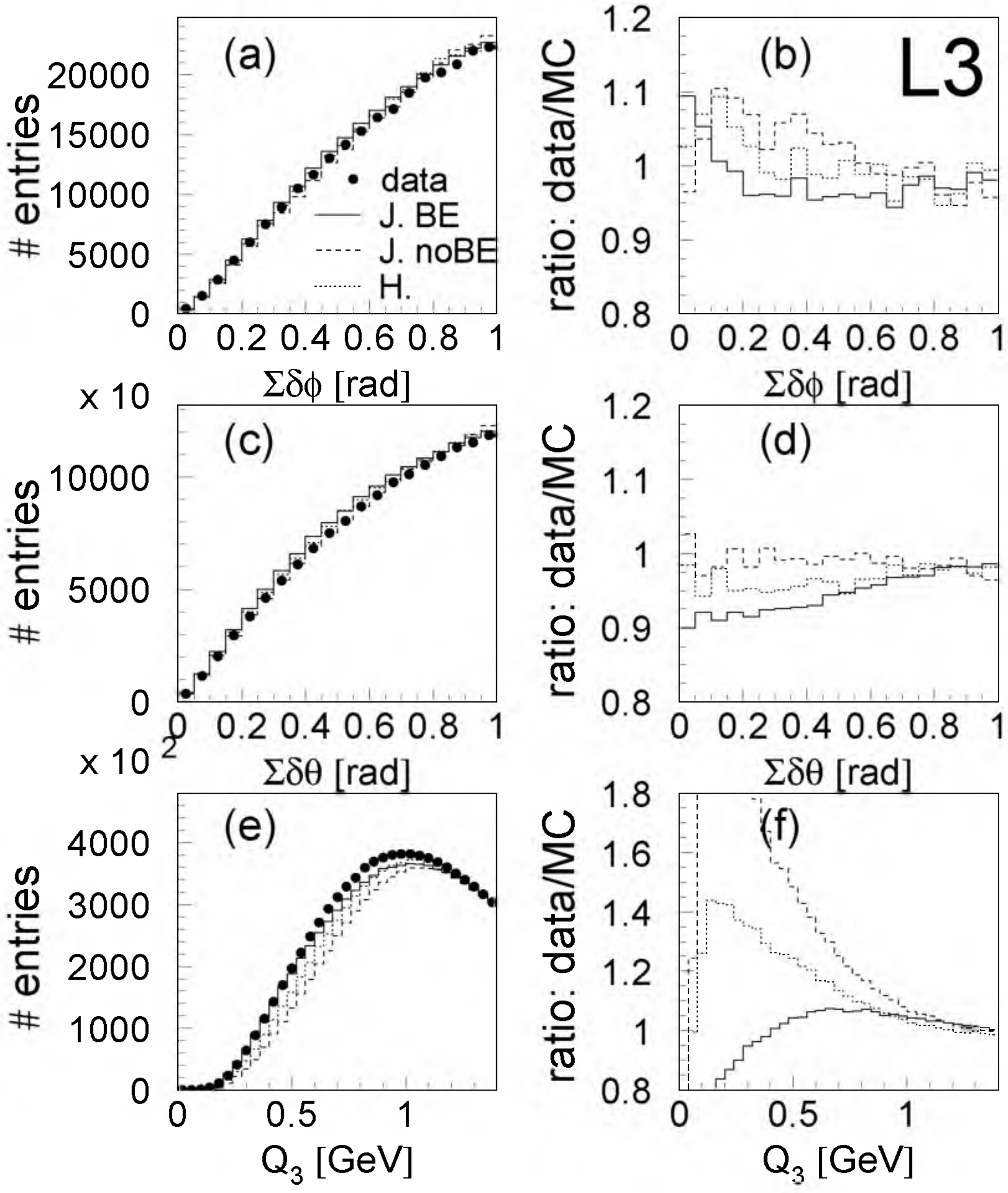

Figure 5.2: Distributions of (a) the sum of the difference in azimuthal angle of pairs of like-sign tracks in a triplet, $\sum \delta\phi$, (c) the sum of the difference in polar angle of pairs of like-sign tracks in a triplet, $\sum \delta\theta$, (e) $Q_3$, for data (dots), JETSET with BE effects (full histogram), JETSET without BE effects (dashed histogram) and HERWIG (dotted histogram). The ratios of the data to the MC distributions are shown in (b), (d) and (f).

of the MCs describe the $Q_3$ distribution: JETSET with BE effects overestimates the data (by more than 20% at low $Q_3$), JETSET without BE effects and HERWIG underestimate the data (by several tens of percent). The statistics for $Q_3 < 160\,\mathrm{MeV}$ are so poor, that this region is rejected from the analysis.

## 5.3 Determination of $R_3$ and $R_3^{\mathrm{genuine}}$

The reference sample, from which $\rho_{0,3}$ is determined, is in many respects the same as described in subsection 3.4.1. It is formed by mixing particles from different data events in the following way. Firstly, events are rotated to a system with the $z$-axis along the thrust axis and are stored in a "pool". Then, tracks of each new event outside the pool are exchanged by tracks of the same charge from events in the pool of the same multiplicity class under the condition that no track originates from the same event. Also in these mixed events only tracks with momenta smaller than 1 GeV and like-sign track pairs with opening angle larger than 3° are accepted. Finally, $Q_3$ is calculated for each triplet of like-sign tracks.

However, this mixing procedure removes more correlations than just those of BE, e.g., those from energy-momentum conservation and from resonances. This effect is estimated by MC using a generator with no BE effects (JETSET or HERWIG). Thus, in the absence of BEC, the corrected three-particle density is given by

$$\rho_{0,3}(Q_3) = \rho_{\mathrm{mix}}(Q_3) \cdot C_{\mathrm{mix}}(Q_3) \quad , \quad \text{where } C_{\mathrm{mix}}(Q_3) = \left[\frac{\rho_3(Q_3)}{\rho_{\mathrm{mix}}(Q_3)}\right]_{\mathrm{MC,noBE}} \quad . \tag{5.13}$$

The ratio $\rho_3/\rho_{\mathrm{mix}}$ must further be corrected for detector resolution, acceptance, efficiency and for particle misidentification. For this we use a multiplicative factor derived from MC studies. Since the L3 detector does not identify the hadrons, this factor, $C_{\mathrm{det}}$, is given by the ratio of the three-*pion* correlation function found from MC events at generator level to the three-*particle* correlation function found using all particles after full detector simulation, reconstruction and selection:

$$C_{\mathrm{det}}(Q_3) = \left(\frac{\rho_3(Q_3)}{\rho_{\mathrm{mix}}(Q_3)}\right)_{\mathrm{gen,\,pions}} \Big/ \left(\frac{\rho_3(Q_3)}{\rho_{\mathrm{mix}}(Q_3)}\right)_{\mathrm{det,\,all}} \quad . \tag{5.14}$$

Combining this correction factor with (5.3) and (5.13) results in

$$R_3(Q_3) = \frac{\rho_3(Q_3)}{\rho_{\mathrm{mix}}(Q_3)} \cdot \frac{1}{C_{\mathrm{mix}}(Q_3)} \cdot C_{\mathrm{det}}(Q_3) \quad . \tag{5.15}$$

To see the gain in model independence of the correction factor due to the momentum cut at 1 GeV and the opening angle cut at 3°, fig. 5.3 shows the ratio of $C_{\mathrm{det}}$ from JETSET with BE effects to that of JETSET without BE effects, before and after these two cuts. We observe that after the cuts, the difference between the two correction factors has diminished by approximately a factor two.

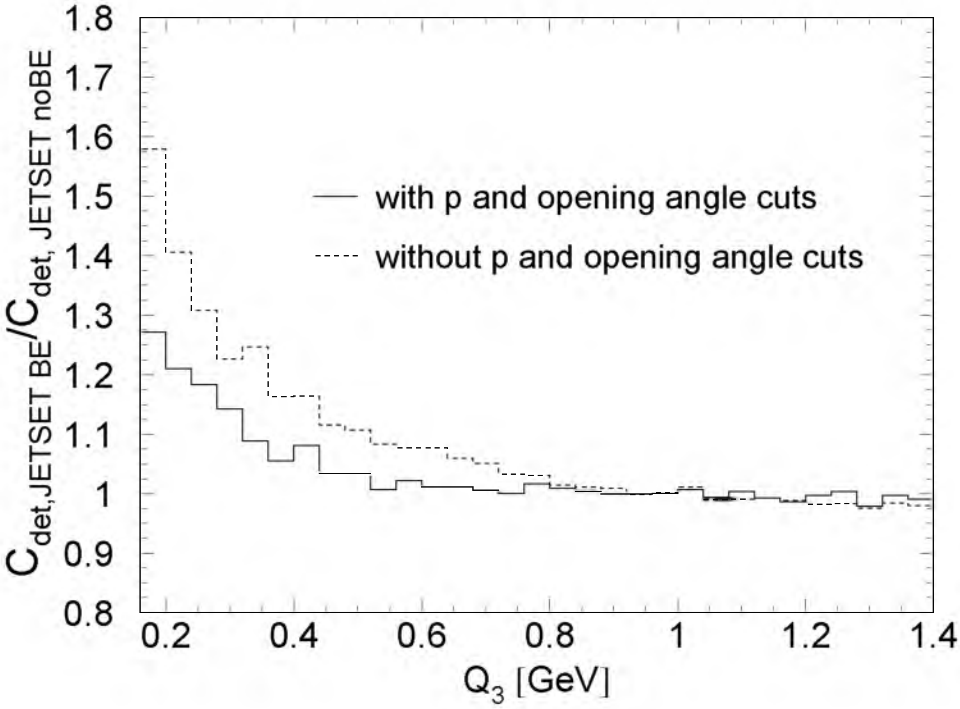

Figure 5.3: The ratio of $C_{\mathrm{det}}$, eqn. (5.14), from JETSET with BE effects to that of JETSET without BE effects, before (dashed histogram) and after (full histogram) the momentum and opening angle cuts.

The main goal of this chapter is to determine the *genuine* three-particle BE correlation function, $R_3^{\mathrm{genuine}}$, eqn. (5.8). Therefore, we need to determine not only $R_3$, but also $\sum \rho_1(p_1)\rho_2(p_2,p_3)$, see eqn. (5.2), containing the contribution of the two-particle correlations. This product of densities is determined by combining two like-sign tracks from the same event and one track with the same charge from another event with the same multiplicity, after rotating the events to a system with the $z$-axis along the thrust axis. Finally, the variable $Q_3$ is calculated from these three tracks. This procedure is similar to that given in [105]. To correct $(\sum \rho_1\rho_2)/\rho_{0,3}$ for detector effects, this ratio is multiplied by its value found from MC events using pions at generator level to that found using all particles at the detector level, similarly to eqn. (5.14).

In this analysis, we use JETSET without BEC and HERWIG to determine the mixing correction factor, $C_{\mathrm{mix}}$, and JETSET (with and without BEC) as well as HERWIG to determine the detector correction factor, $C_{\mathrm{det}}$. Together with a variation of the mixing technique, the selection criteria and the fit range, these 6 MC combinations will serve to estimate systematic errors.

No attention has yet been paid to the effect of Coulomb repulsion of the like-charged pions in the final-state. A way to correct the data for two-pion Coulomb repulsion is to weight each pair of pions by the inverse Gamow factor [9]

$$G_2^{-1}(\eta) = \frac{\exp(2\pi\eta) - 1}{2\pi\eta}, \quad \text{where} \quad \eta = \frac{m_\pi \alpha}{Q} \quad , \tag{5.16}$$

where $m_\pi$ is the mass of the pion, $\alpha$ the fine-structure constant and $Q$ the four-momentum difference between the two pions. It is shown in [63] that this Gamow factor is in principle suitable for our purposes. For $\rho_3$ the following correction factor is used

$$G_3^{-1}(Q_3) \equiv \langle G_2^{-1}(Q_{12}) G_2^{-1}(Q_{13}) G_2^{-1}(Q_{23}) \rangle \quad . \tag{5.17}$$

For $\sum \rho_2 \rho_1$ the same correction factor is used but with $G_2(Q_{ij}) \equiv 1$ when particles $i$ and $j$ come from different events.

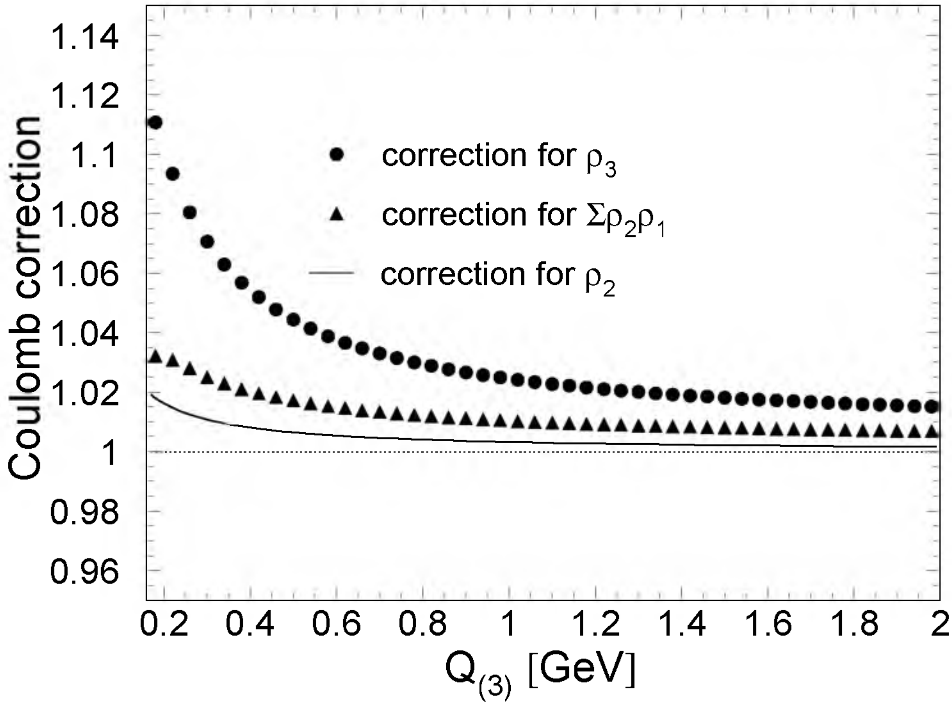

Figure 5.4: The Gamow Coulomb corrections for the densities $\rho_3$, $\sum \rho_2 \rho_1$ and $\rho_2$.

Fig. 5.4 shows the Coulomb correction for $\rho_3$, $\sum \rho_1 \rho_2$ and $\rho_2$. For $\rho_3$ and $\sum \rho_1 \rho_2$ this is done as a function of $Q_3$, for $\rho_2$ as a function of $Q$. It is clear that there is a non-negligible contribution when triplets are considered, in contrast to the two-particle density where the Coulomb correction is small.

Instead of applying the Coulomb correction to the data, we could also apply it on the MC reference sample. This does not necessarily have to yield identical results since, unlike the MC generated sample without BEC, the data are affected by both the BEC and the

Coulomb interactions. However, the effect of using the Coulomb correction factors on the MC reference sample instead of using it on the data, turns out to be negligible.

The genuine three-particle BE correlation function, $R_3^{\text{genuine}}$, eqn. (5.8), is now obtained via

$$R_3^{\text{genuine}} = R_3 - R_{1,2} + 1 \quad , \tag{5.18}$$

where $R_{1,2} \equiv (\sum \rho_1 \rho_2)/\rho_{0,3} - 2$ is the contribution due to two-particle correlations.

## 5.4 Results

The result of the three-particle BE correlation function, $R_3$, eqn. (5.15), is given in fig. 5.5a. In fig. 5.5b the contribution due to two-particle correlations is shown, i.e., $R_{1,2}$. The dots correspond to the data, the small errors indicate the statistical uncertainty, the larger errors include the systematic uncertainty obtained with the six possible combinations of mixing and detector MC corrections, which gives the major part of the total systematic error. Note that the systematic uncertainty obtained from the MC corrections, are correlated between the two distributions of fig. 5.5. The data points in fig. 5.5 are the averages of the data points obtained from the six possible MC mixing and detector corrections. From fig. 5.5a we observe the existence of three-particle correlations and from fig. 5.5b it is clear that a major part is due to two-particle correlations.

As a check, $R_3$ and $R_{1,2}$ are also computed for a MC without BEC (at detector level MC), i.e., JETSET without BEC or HERWIG, instead of the experimental data. For the mixing and detector corrections all possible MC combinations, giving non-trivial results, are studied. E.g., using JETSET without BEC instead of the data and using this MC also for the mixing and detector corrections, gives by construction the trivial result $R_3 = R_{1,2} = 1$. The results of this check are shown in fig. 5.5 as open circles and, as expected, a flat distribution around unity is observed.

Fig. 5.6 shows the genuine three-particle BE correlation function, $R_3^{\text{genuine}}$, eqn. (5.18). The dots correspond to the data, the small errors indicate the statistical uncertainty, the larger errors include the systematic uncertainty obtained with the six possible combinations of mixing and detector MC corrections. From fig. 5.6 we observe the existence of genuine three-particle BE correlations.

The open circles in fig. 5.6 correspond to MC without BEC. As expected, a flat distribution around unity is observed.

In particular, a fit (from $Q_3 = 0.16$ to 1.40 GeV) is performed on the data points with the following parametrization

$$R_3^{\text{genuine}}(Q_3) = \tilde{\gamma}(1 + 2\tilde{\lambda}^{1.5}\exp(-\tilde{R}^2 Q_3^2/2))(1 + \tilde{\varepsilon} Q_3) \quad , \tag{5.19}$$

where $\tilde{\gamma}$ is an overall normalization factor, $\tilde{\lambda}$ measures the strength of the correlation, $\tilde{R}$ is a measure for the effective source size in space-time and the term $(1 + \tilde{\varepsilon} Q_3)$ takes into account possible long-range momentum correlations. The full line in fig. 5.6 corresponds to this fit. The form of this parametrization is a consequence of the assumption that

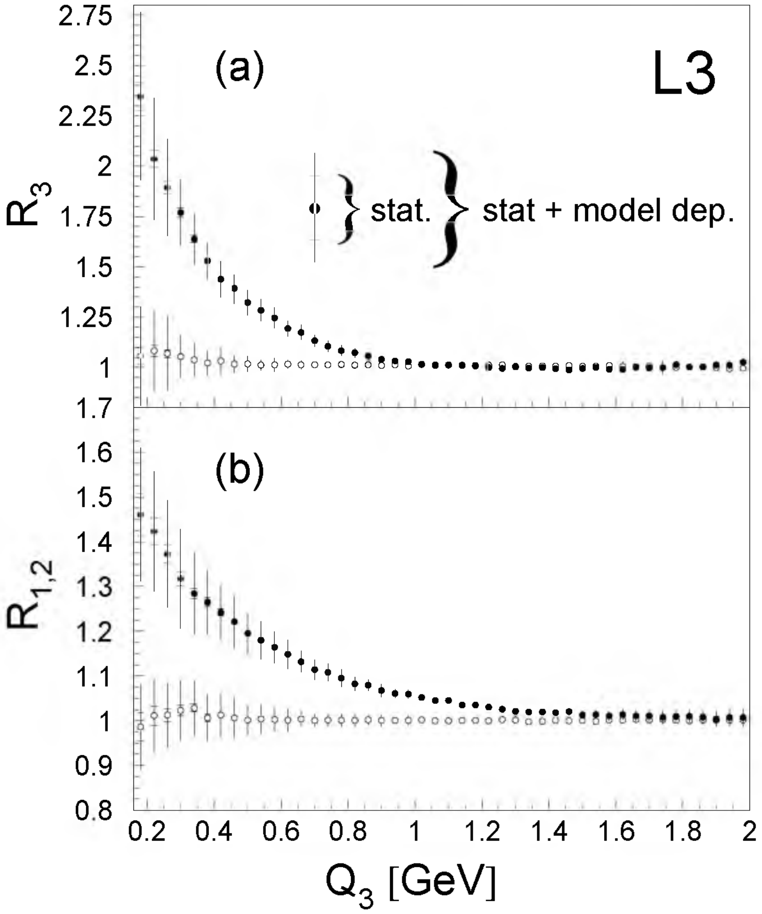

Figure 5.5: The three-particle BE correlation function, $R_3$, eqn. (5.15), (a), the contribution of two-particle correlations, $R_{1,2} \equiv (\sum \rho_2\rho_1)/\rho_{0,3} - 2$, see eqn. (5.2), (b). The dots correspond to the data. The small errors are statistical and the larger errors include the systematic uncertainty obtained with the six possible combinations of mixing and detector MC corrections. The open circles correspond to the results from MC without BEC.

the two-particle BE correlator, $R_2(Q_{ij}) - 1$, in eqn. (5.11), is described by the Gaussian $\tilde{\lambda}\exp(-\tilde{R}^2Q_{ij}^2)$, and $\cos\phi = 1$.

The fit results are given in the first column of table 5.1. The first error is statistical, the second systematic. The estimation of the systematic errors is given in section 5.5.

The fit parameters are found to be highly correlated. E.g., the correlation coefficient between $\tilde{\lambda}$ and $\tilde{R}$ is found to be 0.73, and between $\tilde{\gamma}$ and $\tilde{\lambda}$ $-0.98$.

As a cross-check, the analysis was repeated without the momentum cut of 1 GeV and without the cut of 3° on the opening angle of like-sign track pairs. The results agree with the results quoted in table 5.1, but the systematic errors are approximately twice as large.

Furthermore, the analysis was also repeated using the total number of like-sign particle pairs, instead of the total number of events, to normalize the three-particle density. The

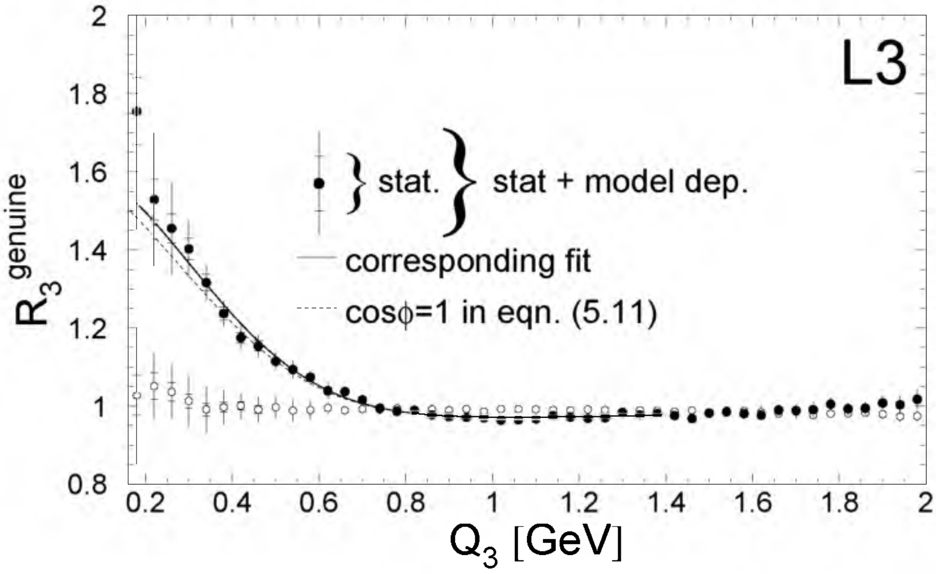

Figure 5.6: The genuine three-particle BE correlation function $R_3^{\text{genuine}}$, eqn. (5.18). The dots correspond to the data. The small errors are statistical, the larger errors include the systematic uncertainty obtained with the six possible combinations of mixing and detector MC corrections. The full line corresponds to the fit (5.19), the dashed line to the prediction of completely incoherent pion production mechanism and a symmetric Gaussian source density in space-time, derived from parametrizing $R_2$ with (5.20). The open circles correspond to results from MC without BEC.

Table 5.1: Value of the fit parameters for the genuine three-particle BE correlation function $R_3^{\text{genuine}}$, using eqn. (5.19) and (5.22). The first error is statistical, the second systematic.

| parameter | eqn. (5.19) | eqn. (5.22) |
|---|---|---|
| $\tilde{\gamma}$ | $0.95 \pm 0.02 \pm 0.03$ | $0.95 \pm 0.02 \pm 0.03$ |
| $\tilde{\lambda}$ | $0.50 \pm 0.03 \pm 0.06$ | $0.72 \pm 0.04 \pm 0.07$ |
| $\tilde{R}$ (fm) | $0.66 \pm 0.03 \pm 0.05$ | $0.72 \pm 0.04 \pm 0.05$ |
| $\tilde{\varepsilon}$ | $0.02 \pm 0.02 \pm 0.02$ | $0.02 \pm 0.02 \pm 0.03$ |
| $\tilde{\kappa}$ | - | $0.75 \pm 0.18 \pm 0.25$ |
| $\chi^2$/NDF | 38.6/27 | 25.8/26 |

effect on the results is negligible, which is due to the way correlation functions are determined. Since we make use of ratios, see, e.g., eqn. (5.15), the normalization factors more or less cancel.

The first measurement of the fraction of coherence is obtained by comparing the intercept parameters of the two- and three-particle BE correlation functions, eqns. (5.9) and (5.10), respectively. Therefore, $R_2(Q) \equiv \rho_2(Q)/\rho_{0,2}(Q)$, i.e., eqn. (5.7), is determined in the same way as the three-particle BE correlation function, i.e., similarly to eqn. (5.15). The result is shown in fig. 5.7, where a clear enhancement at low $Q$ is observed, indicating the BE effect.

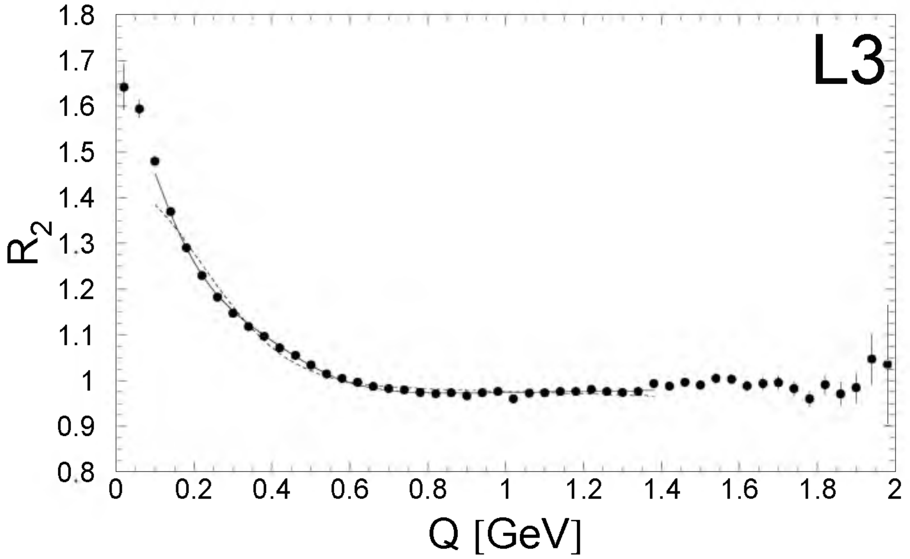

Figure 5.7: The two-particle BE correlation function $R_2$. The errors are statistical only. The full line corresponds to the fit (5.21), the dashed line to the fit (5.20).

The correlation function $R_2$ is parametrized (from $Q$=0.08 to 1.40 GeV) by the Gaussian

$$R_2(Q) = \gamma(1 + \lambda \exp(-R^2Q^2))(1 + \varepsilon Q) \quad . \tag{5.20}$$

The parametrization starts at $Q = 0.08\,\text{GeV}$, conform to starting parametrization (5.19) at $Q_3 = 0.16\,\text{GeV}$. The fit results are given in the first column of table 5.2 and the dashed line in fig. 5.7 corresponds to the fit.

Table 5.2: Value of the fit parameters for the two-particle BE correlation function, $R_2$, using eqn. (5.20) and (5.21). The first error is statistical, the second systematic.

| parameter | eqn. (5.20) | eqn. (5.21) |
|---|---|---|
| $\gamma$ | $0.98 \pm 0.01 \pm 0.02$ | $0.96 \pm 0.02 \pm 0.02$ |
| $\lambda$ | $0.46 \pm 0.01 \pm 0.06$ | $0.72 \pm 0.02 \pm 0.07$ |
| $R$ (fm) | $0.65 \pm 0.01 \pm 0.03$ | $0.73 \pm 0.02 \pm 0.04$ |
| $\varepsilon$ | $0.01 \pm 0.01 \pm 0.02$ | $0.01 \pm 0.01 \pm 0.02$ |
| $\kappa$ | - | $0.78 \pm 0.17 \pm 0.20$ |
| $\chi^2$/NDF | 88.5/29 | 35.6/28 |

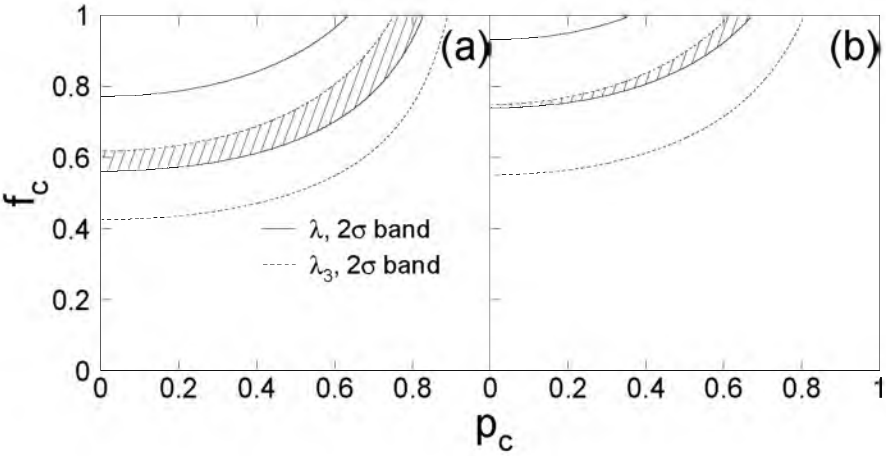

Figure 5.8: Allowed regions for possible values of the core fraction, $f_c$, and the partially coherent core fraction, $p_c$, evaluated on the $2\sigma$ level from the intercepts of the second and third-order BE correlation functions, $\lambda$ and $\lambda_3$, derived from parametrization (5.20), (a), and parametrization (5.21), (b). The dashed area indicates the overlap between the two bands.

The three-particle BE correlation function, $R_3$, is also fitted by the Gaussian, (5.20), where $Q$ is replaced by $Q_3$ and $\lambda$ by $\lambda_3$, resulting in the intercept parameter $\lambda_3 = 1.15 \pm 0.03 \pm 0.22$. The core fraction, $f_c$, and the partially coherent core fraction, $p_c$, are computed from the intercept parameter derived from parametrizing $R_2$, see first column of table 5.2, as well as from the value of $\lambda_3$. Using eqn. (5.9) and given the value of $\lambda$, $f_c$ is computed as a function of $p_c$. In the same way, using eqn. (5.10) and given the value of $\lambda_3$, the possible values for $f_c$ and $p_c$ are computed again. Fig. 5.8a shows the $2\sigma$ bands in the $(f_c, p_c)$ plane that are obtained for these parameters from the values $\lambda$ and $\lambda_3$, extracted from the Gaussian parametrization, (5.20). The overlap area in fig. 5.8a shows that a large range of $(f_c, p_c)$ values is able to describe simultaneously the strength of the two- and three-particle BE correlation functions within 2 standard deviations.

We know that the assumption of a Gaussian source density is not correct, see chapter 3. This is the reason for the poor $\chi^2/\mathrm{NDF}$ values of the Gaussian fits of $R_3^{\mathrm{genuine}}$ and $R_2$. Deviations from a Gaussian can be studied by expanding in terms of derivatives of the Gaussian, which are related to Hermite polynomials. Taking only the lowest-order non-Gaussian term into account, this Edgeworth expansion [65, 66] replaces parametrization (5.20) by

$$R_2(Q) = \gamma(1 + \lambda \exp(-R^2Q^2)(1 + \kappa H_3(\sqrt{2}RQ)/6))(1 + \varepsilon Q) \quad , \qquad (5.21)$$

where $\kappa$ measures the deviation from the Gaussian and $H_3(\sqrt{2}RQ) \equiv (\sqrt{2}RQ)^3 - 3\sqrt{2}RQ$ is the third-order Hermite polynomial.

The fit results for the two-particle BE correlation function, using parametrization (5.21), are given in the second column of table 5.2 and the full line in fig. 5.7 corresponds to this fit. The same parametrization is used for $R_3$, resulting in $\lambda_3 = 1.87 \pm 0.07 \pm 0.31$. Fig. 5.8b shows a similar plot as fig. 5.8a, but from the values $\lambda$ and $\lambda_3$, extracted from parametrization (5.21). Again, the overlap area shows that a large range of $(f_c, p_c)$ values is able to describe simultaneously the strength of the two- and three-particle BE correlation functions within 2 standard deviations. Thus, neither the fully incoherent, nor the partially coherent source picture can be excluded by these results.

The second measurement of the fraction of coherence also makes use of the information of the width of the correlation function. In case the space-time structure of the pion source is Gaussian, and the pion production mechanism is completely incoherent and symmetric, $\tilde{\lambda}$ and $\tilde{R}$, derived from the fit according to eqn. (5.19), measure the strength of the correlation and the effective source size as would be obtained from the two-particle BE correlation function, see eqn. (5.11). We observe that the values of $\lambda$ and $R$, shown in the first column of table 5.2, are consistent with $\tilde{\lambda}$ and $\tilde{R}$ shown in the first column of table 5.1. Using these values of $\lambda$ and $R$ instead of $\tilde{\lambda}$ and $\tilde{R}$ in eqn. (5.19), which is justified if $\cos\phi = 1$, results in the dashed line in fig. 5.6.

To see how well $R_3^{\text{genuine}}$ corresponds to a completely incoherent pion production mechanism and a symmetric Gaussian source density in space-time, the confidence level (CL) is computed by comparing $R_3^{\text{genuine}}$ with the prediction from the two-particle BE correlation function $R_2$, as a function of $\cos\phi$, eqn. (5.11). The result is shown in fig. 5.9, where the CL is shown as a function of $\cos\phi$, for two regions of $Q_3$. It is clear that no significant deviation from $\cos\phi = 1$ is observed. From the fit curves in fig. 5.6 we observe good agreement over the full range of $Q_3$, indicating that $\cos\phi = 1$ over the full range of $Q_3$. In particular, in the range $0.2 < Q_3 < 0.40$ GeV, $\cos\phi = 1$ at 79% CL, and in $0.2 < Q_3 < 0.64$ GeV, $\cos\phi = 1$ at 95% CL, using both statistical and systematic errors. This is consistent with a fully incoherent production mechanism of pions. However, partial coherence cannot be fully excluded. E.g., in the range $0.2 < Q_3 < 0.40$ GeV, $\cos\phi = 0.84$ at 5% CL, and in $0.2 < Q_3 < 0.64$ GeV, $\cos\phi = 0.82$ at 5% CL. Furthermore, $\cos\phi$ is calculated for each bin in $Q_3$ (from 0.16 to 0.80 GeV). The result is shown in fig. 5.10. At low $Q_3$, $\cos\phi$ is systematically higher than unity, which is a result of the Gaussian fit. From the curves shown in fig. 5.6 we observe that the Gaussian fit underestimates the data at low $Q_3$, resulting in high values of $\cos\phi$.

Using the first-order Edgeworth expansion of the Gaussian, eqn. (5.21), and using eqn. (5.11), assuming that $\cos\phi = 1$, the parametrization (5.19) becomes

$$\begin{aligned} R_3^{\text{genuine}}(Q_3) &= \tilde{\gamma}\left(1 + 2\tilde{\lambda}^{1.5}\exp(-\tilde{R}^2 Q_3^2/2)\left[\prod_{i,j=1,\, j>i}^{3}\left(1 + \frac{H_3(\sqrt{2}\tilde{R}Q_{ij})}{6}\tilde{\kappa}\right)^{1/2}\right]\right)(1+\tilde{\varepsilon}Q_3) \\ &\simeq \tilde{\gamma}\left(1 + 2\tilde{\lambda}^{1.5}\exp(-\tilde{R}^2 Q_3^2/2)\left[1 + \frac{H_3(\sqrt{2}\tilde{R}Q_3/2)}{6}\tilde{\kappa}\right]^{1.5}\right)(1+\tilde{\varepsilon}Q_3) \quad . \quad (5.22) \end{aligned}$$

In the second line the approximation is made that $Q_{ij} = Q_3/2$, which is found to be valid within approximately 25% at low $Q_3$. The results of the fit according to eqn. (5.22) are

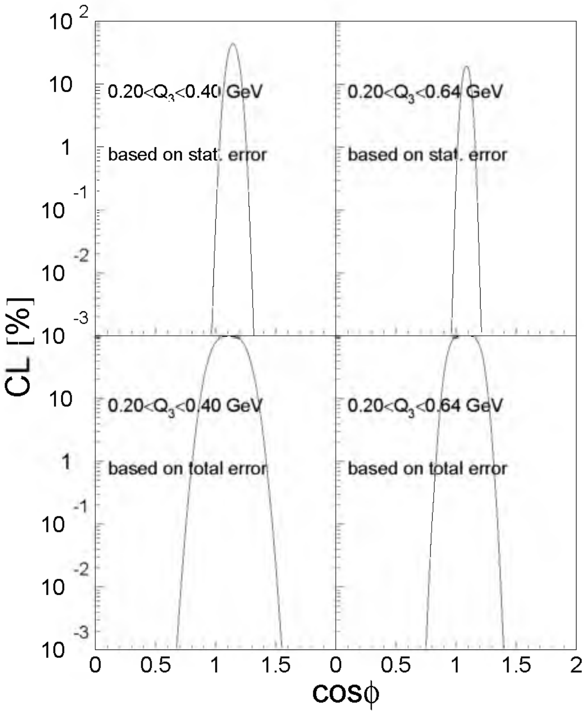

Figure 5.9: Confidence level distributions as a function of $\cos\phi$, assuming that $f(x)$ is Gaussian distributed. The upper plots are based on statistical errors, the lower plots include systematic errors as well.

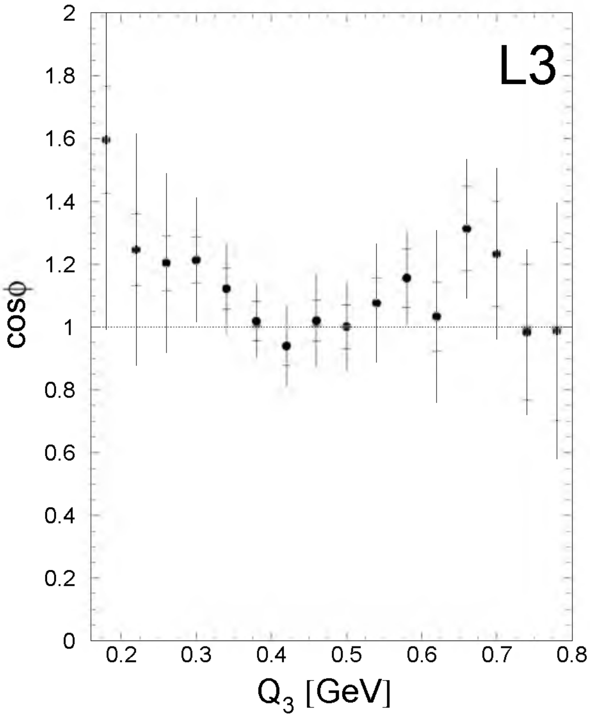

Figure 5.10: $\cos\phi$ as a function of $Q_3$ assuming $R_2$ is described by the Gaussian, (5.20). The small errors are statistical, the larger errors include systematic uncertainties as well.

given in the second column of table 5.1. The $\chi^2$/NDF is found to be better than when parametrization (5.19) is applied, and the value of $\tilde{\lambda}$ is significantly higher. Again, the fit parameters are found to be highly correlated.

The values for $\lambda$ and $R$, shown in the second column of table 5.2, are found to be consistent with the corresponding $\tilde{\lambda}$ and $\tilde{R}$ found from the genuine three-particle BE correlation function, shown in the second column of table 5.1, as would be expected for a fully incoherent production mechanism of pions.

For illustration, figs. 5.11, 5.12 and 5.13 show plots analogously to figs. 5.6, 5.9 and 5.10, respectively. The only difference is that the first-order Edgeworth expansion of the Gaussian is used.

From fig. 5.11 we observe good agreement between the fit of $R_3^{\text{genuine}}$ using parametrization (5.22) and the prediction of a completely incoherent and symmetric pion production region, derived from parametrizing $R_2$ with (5.21), over the full range of $Q_3$. Furthermore, the CL distributions shown in fig. 5.12 prefer a value of $\cos\phi$ consistent with unity. In particular, in the range $0.2 < Q_3 < 0.40$ GeV, $\cos\phi = 1$ at 99% CL, and in $0.2 < Q_3 < 0.64$

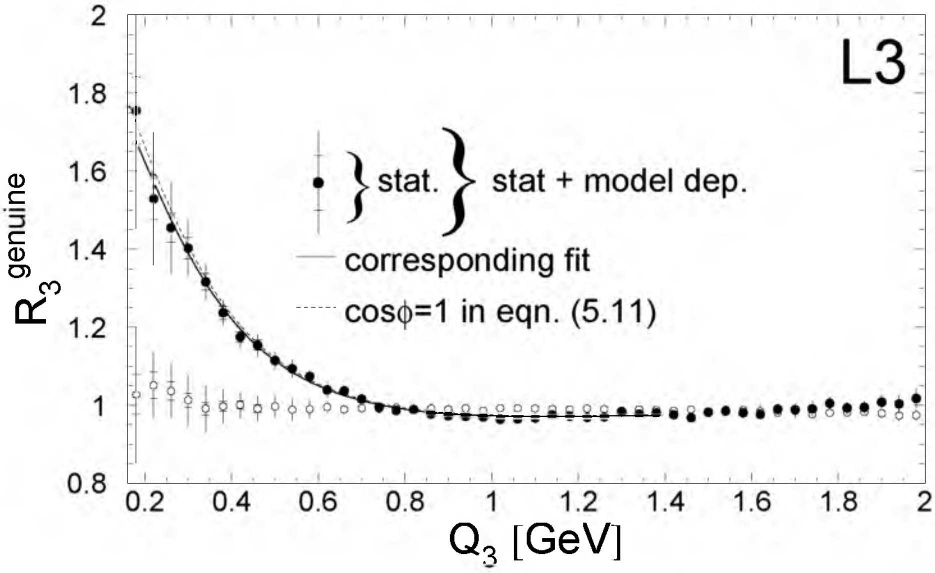

Figure 5.11: The genuine three-particle BE correlation function $R_3^{\text{genuine}}$, eqn. (5.18). The small errors are statistical, the larger errors include the systematic uncertainty obtained with the six possible combinations of mixing and detector MC corrections. The full line corresponds to the fit (5.22), the dashed line to the prediction of a completely incoherent and symmetric pion production derived from parametrizing $R_2$ with (5.21). The open circles correspond to the results from MC without BEC.

GeV, $\cos\phi = 1$ at 99% CL, using both statistical and systematic errors. This is consistent with a fully incoherent production mechanism of pions. However, partial coherence cannot be fully excluded. E.g., in the range $0.2 < Q_3 < 0.40$ GeV, $\cos\phi = 0.74$ at 5% CL, and in $0.2 < Q_3 < 0.64$ GeV, $\cos\phi = 0.78$ at 5% CL. Furthermore, $\cos\phi$ is calculated for each bin in $Q_3$ (from 0.16 to 0.80 GeV) again. The result is shown in fig. 5.13. No deviation from unity is observed.

## 5.5 Systematic Uncertainties

To estimate the systematic errors on the fit parameters, five different sources are examined. Firstly, we looked at the fit results obtained with the six possible combinations of mixing and detector MC corrections. The systematic error from this source is taken as the RMS of these six values. Secondly, the influence of a different mixing sample was studied by removing the conditions that tracks are replaced by tracks with the same charge and coming from events with approximately the same multiplicity. For each of the six MC combinations the difference in the results between the two mixing methods was taken as an estimate of the systematic error from this source and the square root of the mean of the squares of these differences taken as the systematic error from this source. In the

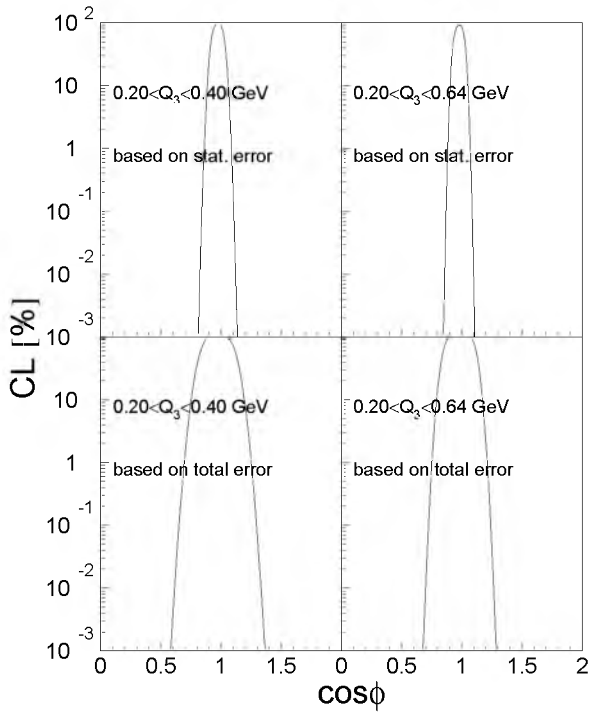

Figure 5.12: Confidence level distributions as a function of $\cos\phi$, assuming $R_2$ is described by the first-order Edgeworth expansion, eqn. (5.21). The upper plots are based on statistical errors, the lower plots include systematic errors as well.

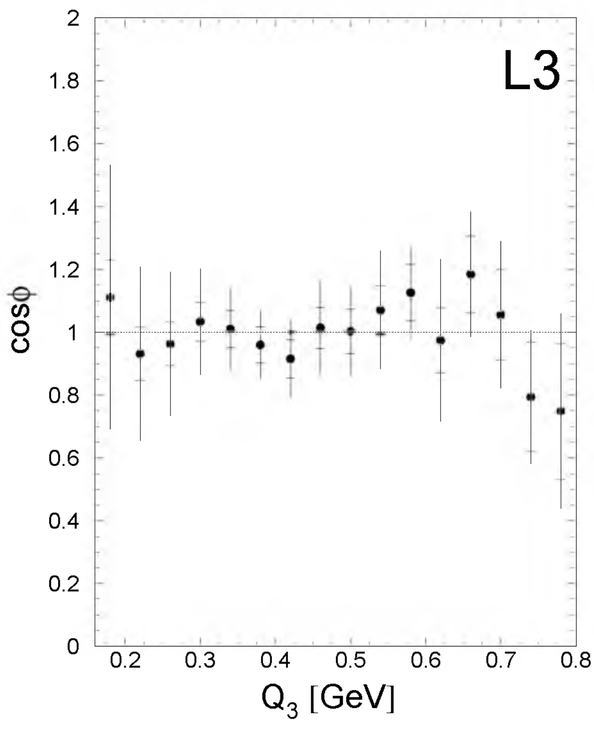

Figure 5.13: $\cos\phi$ as a function of $Q_3$ assuming $R_2$ is described by the first-order Edgeworth expansion of the Gaussian, (5.21). The small errors are statistical, the larger errors include systematic uncertainties as well.

same way, systematic errors related to track/event selection and to the choice of the fit range were evaluated. This analysis was repeated with stronger and weaker selection criteria, resulting in approximately 11% fewer/more events and 12% fewer/more tracks. The cuts presented in section 3.2 and the momentum and opening angle cuts were all varied separately within "reasonable" values keeping the other cuts on their standard values. For each cut the maximum deviation of the measurement obtained within this range is taken as the contribution to the systematic error of the measurement due to this cut. The fit range was varied by removing the first point of the fit and varying the end point by ±200 MeV. Finally, we studied the influence of removing like-sign track pairs with small polar and azimuthal opening angles. The maximum deviation that was found by varying the cuts on the opening angles up to 6°, was taken as the systematic error from this source. As a total systematic error we add the five errors from these sources in quadrature. For all fit parameters, the largest part (varying from approximately 50 to 90%, depending on the fit parameter) of the total systematic error is due to the six possible combinations of mixing

Table 5.3: Contribution to the systematic error on the fit parameters of parametrizations (5.19) and (5.22), respectively.

| parametr. | eqn. (5.19) | | | | eqn. (5.22) | | | | |
|---|---|---|---|---|---|---|---|---|---|
| fit par. | $\tilde{\gamma}$ | $\tilde{\lambda}$ | $\tilde{R}$, fm | $\tilde{\varepsilon}$, GeV$^{-1}$ | $\tilde{\gamma}$ | $\tilde{\lambda}$ | $\tilde{R}$, fm | $\tilde{\varepsilon}$, GeV$^{-1}$ | $\tilde{\kappa}$ |
| modelling | 0.021 | 0.053 | 0.040 | 0.013 | 0.024 | 0.065 | 0.045 | 0.019 | 0.16 |
| mixing | 0.004 | 0.006 | 0.009 | 0.007 | 0.010 | 0.009 | 0.011 | 0.011 | 0.04 |
| fit range | 0.008 | 0.019 | 0.020 | 0.013 | 0.010 | 0.022 | 0.017 | 0.019 | 0.14 |
| track/ev. sel. | 0.010 | 0.013 | 0.012 | 0.008 | 0.011 | 0.016 | 0.012 | 0.007 | 0.10 |
| $\delta\phi + \delta\theta$ cut | 0.013 | 0.014 | 0.012 | 0.009 | 0.014 | 0.017 | 0.010 | 0.008 | 0.11 |
| total | 0.03 | 0.06 | 0.05 | 0.02 | 0.03 | 0.07 | 0.05 | 0.03 | 0.25 |

and detector MC corrections.

For illustration, table 5.3 shows the systematic uncertainties for each of the sources, for the fit parameters of eqns. (5.19) and (5.22), respectively. Especially for $\tilde{\lambda}$ and $\tilde{R}$, it is clear that the systematic errors are dominated by the "modelling".

## 5.6 Comparison with JETSET

In this section, the results of the L3 data are compared with JETSET (with BE effects according to the BE$_0$ and BE$_{32}$ algorithms) generated samples.

For the JETSET generated samples, $R_3$ and $(\sum \rho_1\rho_2)/\rho_{0,3}$ are taken as

$$R_{3,\,\mathrm{JETSET}} \equiv \left(\frac{\rho_3}{\rho_{0,3}}\right)_{\mathrm{JETSET}} = \left(\frac{\rho_3}{\rho_{\mathrm{mix}}}\right)_{\mathrm{JETSET}} \cdot \left(\frac{\rho_{\mathrm{mix}}}{\rho_3}\right)_{\mathrm{JETSET,\,noBE}} , \tag{5.23}$$

$$\left(\frac{\sum \rho_1\rho_2}{\rho_{0,3}}\right)_{\mathrm{JETSET}} = \left(\frac{\sum \rho_1\rho_2}{\rho_{\mathrm{mix}}}\right)_{\mathrm{JETSET}} \cdot \left(\frac{\rho_{\mathrm{mix}}}{\rho_3}\right)_{\mathrm{JETSET,\,noBE}} . \tag{5.24}$$

The genuine three-particle BE correlation function is obtained via eqn. (5.18). The result is shown in fig. 5.14 as the histogram. The BEC are implemented according to the BE$_0$ algorithm. For comparison, the data are shown by the dots again. It is clear that JETSET overestimates the data, which we already concluded from fig. 5.2f.

In particular, the full line in fig. 5.14 corresponds to the fit on the JETSET sample with the first-order Edgeworth expansion, eqn. (5.22). The fit gives $\tilde{\lambda} = 1.07 \pm 0.03$(stat) and $\tilde{R} = 0.75 \pm 0.03$(stat). Although $\tilde{R}$ agrees with the data, $\tilde{\lambda}$ is significantly higher, see second column table 5.1. Also shown in fig. 5.14 is a dashed line which corresponds to the prediction of JETSET assuming a completely incoherent and symmetric pion production derived from parametrizing $R_{2,\,\mathrm{JETSET}}$ with (5.21). This line clearly underestimates the histogram (or the full line), indicating that $\cos\phi > 1$, i.e., there is an unphysical amount of genuine three-particle BEC in JETSET. When the BE$_{32}$ algorithm is used, instead of BE$_0$, the same conclusion is obtained.

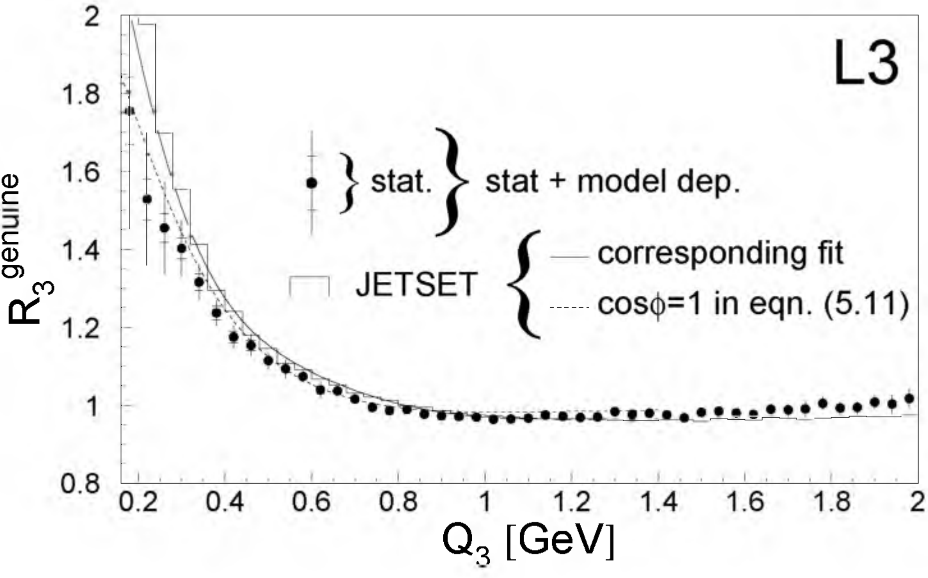

Figure 5.14: The genuine three-particle BE correlation function $R_3^{\text{genuine}}$ for the data (dots) and for MC generated events according to JETSET with BEC (histogram). The full line corresponds to the fit (5.22) on the JETSET sample, the dashed line to the prediction of a completely incoherent and symmetric pion production derived from parametrizing $R_{2,\,\text{JETSET}}$ with (5.21).

It is not surprising that JETSET does not describe three-particle BEC, since these correlations are not implemented, explicitly. Only two-particle BEC are implemented by shuffling the momenta of particles such that two-particle BEC are simulated. It appears that this shuffling algorithm artificially creates genuine three-particle BEC, even more than the data show.

## 5.7 Summary and Comparison with Other Experiments

An analysis was performed of the three-particle BE correlation function in the process $e^+e^- \rightarrow Z \rightarrow$ hadrons with the L3 detector at LEP. The three-particle BE correlation function of like-charged pions and the contribution to this function due to two-particle BEC were computed. The observation of the existence of genuine three-particle BEC was made. In particular, using parametrization (5.22) we extracted $\tilde{\lambda} = 0.72 \pm 0.04 \pm 0.07$, measuring the strength of the correlations, and $\tilde{R} = 0.72 \pm 0.04 \pm 0.05$ fm, measuring the effective source size in space-time. Combining this result with the measurement of two-particle BEC we find the data to be consistent with a fully incoherent production mechanism of pions, but a partially coherent mechanism cannot be fully excluded.

It is important to note that this result does not necessarily contradict [106] the Lund string model [38, 39]. The BE effect, as a coherent phenomenon, has been given an explanation by this model. The basic result of this model is the Lund area law, see also section 4.10, which describes the production probability of a set of hadrons with certain four-momenta, in terms of the area $A$ of the string before the decay, i.e., before the hadrons are formed, in space-time. If there are identical bosons, each pair of bosons gets a contribution from two different areas, as a consequence of symmetrizing the matrix element. Consequently, a phase difference, $\Delta A$, between any two bosons appears in the correlator, which is proportional to the area difference between them in the Lund model. In general, the value of $\Delta A$ depends on the intermediate system between the two bosons under consideration. The intermediate system differs from event to event. This leads to a variation of the phases and possibly the onset of incoherent like behaviour, depending on how much $\Delta A$ approaches a uniformly distributed random variable in the Lund string model.

The LEP collaborations DELPHI and OPAL have also performed three-particle BE analyses. The DELPHI collaboration was the first to observe genuine three-particle correlations in $\mathrm{e^+e^-} \to \mathrm{Z} \to$ hadrons events [107], which can be explained as higher-order BE correlations. Looking at two-jet events only, neglecting Coulomb repulsion and not correcting for pion purity, a Gaussian parametrization similar to eqn. (5.19), was fitted from $Q_3 = 0.15$ to 1.35 GeV. Correcting for pion purity would increase $\tilde{\lambda}$ by 39%. Applying this correction to their result gives $\tilde{\lambda} = 0.53 \pm 0.07 \pm 0.10$ and $\tilde{R} = 0.93 \pm 0.06 \pm 0.04$ fm. This value of $\tilde{\lambda}$ agrees within one standard deviation with our result while $\tilde{R}$ disagrees by about 3 standard deviations (see first column of table 5.1). The OPAL collaboration also observed genuine three-particle BEC [108]. Using the same parametrization as DELPHI, from $Q_3 = 0.25$ to 2 GeV, OPAL found $\tilde{\lambda} = 0.80 \pm 0.02 \pm 0.08$ (corrected for Coulomb repulsion and pion purity), which is 3 standard deviations higher than our result, and $\tilde{R} = 0.82 \pm 0.01 \pm 0.04$ fm, which deviates from our result by approximately 2.5 standard deviations. Note that OPAL did not use a mixing procedure, but simply took a Monte Carlo without BEC to obtain a reference sample free from these correlations. Furthermore, besides the differences in the analyses, there is also a large correlation between the fit parameters, which might cause differences in our results.

Neither DELPHI, nor OPAL, measured $\cos\phi$. It was measured in meson-proton collisions by NA22 [105] and found to be consistent with unity, be it within very large errors. It was also measured in sulphur-lead collisions by NA44 [109, 110] and found to be $0.20 \pm 0.20$, which is interpreted there as a partially coherent emission of particles, but may also be due to overlap of independent sources. For lead-lead collisions the same experiment found $0.85 \pm 0.22$ [110], compatible with an incoherent mechanism for particle production. The latter result is supported by the WA98 collaboration [111] with $0.61 \pm 0.18$.

These results may be difficult to explain by conventional pion interferometry: when interpreting $\phi$ as a phase, $\mathrm{e^+e^-}$ and lead-lead results would be consistent with a fully incoherent production mechanism, while sulphur-lead would be consistent with a coherent production mechanism. An alternative explanation could be overlap of independent sources which suppresses $R_3^{\text{genuine}} - 1$ faster than the denominator of (5.11), until the density of sources (strings) becomes large enough to allow percolation of strings [112] in lead-lead collisions.

# Appendix A

# Basic Relations

In this appendix, the necessary formalism and basic relations, on which the analyses in this thesis are based, are given. No originality is claimed in this appendix. The only purpose is to fix the notation and summarize a number of results which are used throughout this work. For a more complete review I refer to [34].

In a sample of $n$ identical particles in a phase space domain $\Omega$, let the symbol $y$ represent the kinematical variables needed to specify the position of each particle in this space. Defining $u(y)$ as an arbitrary function of $y$ in $\Omega$, one can write the generating functional

$$\mathcal{R}\left[u(y)\right] = 1 + \sum_{q=1}^{\infty} \frac{1}{q!} \int_{\Omega} \rho_q(y_1, \ldots, y_q) u(y_1) \cdots u(y_q) \prod_{i=1}^{q} \mathrm{d}y_i \quad , \tag{A.1}$$

which fully determines a distribution of points in $\Omega$. The number density, $\rho_q(y_1, \ldots, y_q)$, for $q$ points to be at $y_1, \ldots, y_q$, irrespective of the presence and location of any further point is then given by (when $\rho_0 \equiv 0$)

$$\rho_q(y_1, \ldots, y_q) = \partial^q \mathcal{R}\left[u(y)\right] / \partial u(y_1) \cdots \partial u(y_q)\big|_{u=0} \quad , \tag{A.2}$$

and normalized as

$$\int \rho_q(y_1, \ldots, y_q) \prod_{i=1}^{q} \mathrm{d}y_i = \langle n(n-1) \ldots (n-q+1) \rangle \quad . \tag{A.3}$$

The cumulant correlation function $C_q(y_1, \ldots, y_q)$ can be obtained via

$$C_q(y_1, \ldots, y_q) = \partial^q \mathcal{G}\left[u(y)\right] / \partial u(y_1) \cdots \partial u(y_q)\big|_{u=0} \quad , \tag{A.4}$$

where $\mathcal{G}\left[u(y)\right]$ is the generating functional which can be obtained by the functional identity

$$\mathcal{R}\left[u(y)\right] = \exp\left\{\mathcal{G}\left[u(y)\right]\right\} \quad . \tag{A.5}$$

The relation between the number density functions, $\rho_q$, and cumulant correlation functions, $C_q$, is now given by

$$\rho_1(y_1) = C_1(y_1) \quad , \tag{A.6}$$

$$\rho_2(y_1,y_2) = C_1(y_1)C_1(y_2) + C_2(y_1,y_2) \quad , \tag{A.7}$$

$$\rho_3(y_1,y_2,y_3) = C_1(y_1)C_1(y_2)C_1(y_3) + \sum_{(3)} C_1(y_1)C_2(y_2,y_3) + C_3(y_1,y_2,y_3) \quad , \tag{A.8}$$

etc., where the sum indicates that all possible permutations have to be taken into account.

To study correlations (e.g., Bose-Einstein correlations), one usually defines the following normalized correlation function (see e.g., eqns. (1.8) and (1.17))

$$R'_q(y_1,\ldots,y_q) = \frac{\rho_q(y_1,\ldots,y_q)}{\rho_1(y_1)\cdots\rho_1(y_q)} = 1 + \frac{C_q(y_1,\ldots,y_q)}{\rho_1(y_1)\cdots\rho_1(y_q)} \quad . \tag{A.9}$$

In particular, when one wants to study correlations between particles coming from different W's in the process $\mathrm{W^+W^-} \to \mathrm{q_1\bar{q}_2q_3\bar{q}_4}$, and wants to arrive at eqns. (4.9) and (4.10), which are valid when there is no stochastic dependence between hadrons coming from different W's, one can write the following equations for the generating functionals $\mathcal{R}\left[u(y)\right]$ and $\mathcal{G}\left[u(y)\right]$

$$\mathcal{R}^{\mathrm{WW}}\left[u(y)\right] = \mathcal{R}^{\mathrm{W^+}}\left[u(y)\right]\mathcal{R}^{\mathrm{W^-}}\left[u(y)\right] \quad , \tag{A.10}$$

$$\mathcal{G}^{\mathrm{WW}}\left[u(y)\right] = \mathcal{G}^{\mathrm{W^+}}\left[u(y)\right] + \mathcal{G}^{\mathrm{W^-}}\left[u(y)\right] \quad , \tag{A.11}$$

where the superscript WW indicates that both W's decay hadronically, and the superscript $\mathrm{W^\pm}$ indicates that only $\mathrm{W^\pm}$ decays hadronically. Performing two successive functional differentations of (A.10) over the probing function $u(y)$, leads to

$$\rho_1^{\mathrm{WW}}(y_1) = \rho_1^{\mathrm{W^+}}(y_1) + \rho_1^{\mathrm{W^-}}(y_1) \quad , \tag{A.12}$$

$$\rho_2^{\mathrm{WW}}(y_1,y_2) = \rho_2^{\mathrm{W^+}}(y_1,y_2) + \rho_2^{\mathrm{W^-}}(y_1,y_2) + \rho_1^{\mathrm{W^+}}(y_1)\rho_1^{\mathrm{W^-}}(y_2) + \rho_1^{\mathrm{W^+}}(y_2)\rho_1^{\mathrm{W^-}}(y_1), \tag{A.13}$$

and performing the same functional differentiations of (A.11) gives

$$C_2^{\mathrm{WW}}(y_1,y_2) = C_2^{\mathrm{W^+}}(y_1,y_2) + C_2^{\mathrm{W^-}}(y_1,y_2) \quad . \tag{A.14}$$

Eqns. (A.13) and (A.14) are used in section 4.3 to study BEC in WW events, in particular inter-W BEC.

# Summary

In this thesis, Bose-Einstein correlations (BEC) are studied between identical bosons originating from electron-positron collisions. These collisions take place at the $e^+e^-$-accelerator LEP, nearby Geneva, and the final-state particles of these collisions are detected with the L3 detector. BEC are studied in the two processes $e^+e^- \rightarrow Z \rightarrow q\bar{q}$ and $e^+e^- \rightarrow W^+W^-$, the latter where at least one W decays into a quark-antiquark pair.

The Bose-Einstein (BE) effect in a system of identical bosons is a direct consequence of the symmetrization of the wave function of this system. This quantum mechanical effect is experimentally observed as a relative enhancement of the production of identical bosons with small four-momentum differences, $Q$, with respect to the production that would occur in a world without BEC. In this thesis, there are three motivations to analyse BEC.

- The first interest to study BEC is that they give information on the structure of the source where the hadrons are formed. Or, quoting [113]: "Two-particle correlations provide the only way to obtain directly information about the space-time structure of the source from the measured particle momenta". In chapter 3 of this thesis, the form and shape of the two-particle BE correlation function is measured in three dimensions. In this way, information can be obtained on the structure of the source in three dimensions.

- In the last years, the interest in BEC has grown within the LEP community. This is due to the fact that BEC may influence the W mass measurement, which is one of the main goals of the second phase of LEP (LEP2). In the production of two W bosons that both decay hadronically, i.e., $e^+e^- \rightarrow W^+W^- \rightarrow q_1\bar{q}_2q_3\bar{q}_4$ events, BEC can be expected between bosons originating from different W's. If these inter-W BEC are observed, they will influence the W mass measurement, since then the observer cannot say from which W a boson in the final-state originates. In chapter 4 of this thesis, an analysis is performed to investigate the existence of inter-W BEC. The analysis is done in one dimension since in this case the statistics for a multi-dimensional analysis are too limited.

- In chapter 3, as well as in chapter 4, two-particle correlations are considered. However, additional information, not present in two-particle correlations, can be extracted from higher-order BEC. Higher-order BEC are sensitive to details of several dynamical fluctuations and they can, therefore, be used to distinguish between models for multi-boson production. Higher-order correlations are sensitive to asymmetries of the source and they give a handle on the degree of coherence of the boson production mechanism. In chapter 5 of this thesis, three-particle BEC are studied with the goal to search for indications for a coherent production mechanism.

The $e^+e^-$ events relevant for the studies mentioned above, are collected with the L3 detector, that is build around one of the $e^+e^-$ interaction points. The charged particles used for the analyses are reconstructed in a wire chamber and in a silicon vertex detector. The following main results are obtained from the analysed data.

From approximately 1 million $e^+e^- \rightarrow Z \rightarrow q\bar{q}$ events, selected from the data of 1994 at $\sqrt{s} \simeq 91.2\,\text{GeV}$, a three-dimensional BE correlation function is determined. This is done in the so-called longitudinal centre-of-mass system, where each pair of particles is Lorentz boosted, such that the sum of the two momenta in the direction of the thrust axis – that approximates the direction of the two initial quarks – is zero. The direction along the thrust axis is defined as the longitudinal direction and two directions perpendicular to this axis are called the out- and side-direction. The longitudinal-, as well as the side-direction, are, in Fourier transformed space, a measure of the geometry of the source. The out-direction measures a mixture between a time and a space component. What is really measured with the BE correlation function is the so-called region of homogeneity, i.e., the range over which BE interference takes place. The ratio between the widths of the BE correlation function in the side- and longitudinal-direction of this region is measured and the result is $R_{\text{side}}/R_{\text{L}} = 0.81 \pm 0.02^{+0.03}_{-0.19}$, where the first error is statistical and the second systematic. The systematic error is dominated by the dependence of Monte Carlo models to correct the data for detector effects, as acceptance, resolution and misidentification of particles. The result shows that the source is elongated in the direction of the thrust axis. This result is not reproduced by the presently available Monte Carlo models, because there an assumption of a spherically symmetric source is made. Furthermore, in these models the assumption is made that the region of homogeneity of the source is Gaussian distributed, while the measurements show that the BE correlation function has an enhancement at small $Q$ which is stronger than a Gaussian function. Both the elongation of the source and the non-Gaussian behaviour of the correlation function are, however, theoretically expected in the Lund string model as a consequence of a longitudinal stretching of the string field. In the meantime, the LEP experiments DELPHI and OPAL have also measured the elongation and their results are consistent with this result.

BEC are investigated in the process $e^+e^- \rightarrow W^+W^-$. Especially, correlations between particles originating from different W's (in the same event) are studied. The data that are collected in the years 1998, 1999 and 2000, at $\sqrt{s} \simeq 189 - 209\,\text{GeV}$, corresponding to 89% of the L3 data collected at LEP2, are analysed. In total, approximately 9000 $W^+W^-$ events are selected. Both W's decay hadronically in 58% of these events (fully hadronic channel). In the other events, one W decays hadronically and the other W decays into a lepton and its corresponding (anti-)neutrino (semi-hadronic channel). The difficulty in the selection is that a significant percentage of background events is selected, varying from a few percent in the semi-hadronic channel to approximately 20% in the fully hadronic channel. Apart from the quark flavour composition, one expects hadronic W and Z decays to be similar. Since b quarks are greatly suppressed in W decay, a b-tagging procedure is used to reduce the original $b\bar{b}$ fraction in Z decays from 22% to 3%. The remaining light-quark Z decays give a BE correlation function that is consistent with the correlation function obtained from the semi-hadronic WW events, as expected. Furthermore, the BEC in the fully hadronic WW channel are observed to be less strong than in the semi-hadronic channel. This is in agreement with no or weak inter-W BEC. A direct measurement of inter-W BEC is performed by studying whether the WW data deviate from a relation that is, by construction, only valid when no inter-W correlations are present. The result is that there are no indications for the presence of inter-W BEC. The model dependence of this result is small, since a sample of events is constructed, directly from the data, by mixing different semi-hadronic WW events. This sample looks like a sample of fully hadronic WW events, but with the property that inter-W correlations are absent. A typical variable that is sensitive to inter-W BEC, is $\Lambda$. The result of the measurement of $\Lambda$ is $0.008 \pm 0.018 \pm 0.016$, where the first error is statistical and the second error systematic. This result is consistent with no inter-W BEC. A Monte Carlo model with inter-W BEC gives $\Lambda = 0.126 \pm 0.008$. The data deviate from this model by 4.7 standard deviations. The statistical error includes bin-bin correlations in the $Q$ variable, that are caused by multiplicity fluctuations in the WW events. The most important consequence of the result of the study on inter-W BEC is that the uncertainty on the W mass measurement due to inter-W BEC is small. Before this analysis, uncertainties were estimated from 60 to 100 MeV. For the time being, the uncertainty is estimated to be 20 MeV. Published results of ALEPH and preliminary results of DELPHI are also consistent with no inter-W BEC. Preliminary results of OPAL are inconclusive due to lack of statistics. Ongoing studies and combination of results of the different LEP experiments can, therefore, reduce the uncertainty below 10 MeV (in case no inter-W BEC will be found).

Besides two-particle BEC, also three-particle BEC are studied on the hadronic Z decay data collected in 1994. The kinematical variable that is used, is $Q_3 \equiv (Q_{12}^2 + Q_{13}^2 + Q_{23}^2)^{1/2}$, where $Q_{ij}$ $(i, j = 1, 2, 3)$ is the four-momentum difference between particles $i$ and $j$. In the three-particle BE correlation function, a large part of the correlations originates from two-particle correlations. After removing the contribution from two-particle BEC, the remnant shows the existence of genuine three-particle BEC. A formalism, giving a relation between two- and three-particle BEC, assuming an incoherent production mechanism of bosons, is tested. In this relation, a phase, $\phi$, is defined, that deviates from zero when the mechanism is (partially) coherent. The data show that $\phi$ is consistent with zero, conform to an incoherent production mechanism. The uncertainty on this measurement is mainly due to the Monte Carlo model dependence to correct the data for detector effects. The model dependence is somewhat reduced by a special selection on the momenta of the particles and the opening angle between the particles. However, a partially coherent production mechanism cannot be fully excluded. The LEP experiments DELPHI and OPAL have also measured genuine three-particle BEC. However, they did not measure $\phi$.

# Samenvatting

In dit proefschrift zijn Bose-Einstein correlaties (BEC) bestudeerd tussen identieke bosonen komende van electron-positron botsingen. De botsingen vinden plaats in de $e^+e^-$-versneller LEP, nabij Genève, en de deeltjes in de eindtoestanden van deze botsingen worden gedetecteerd met de L3 detector. BEC zijn bestudeerd in de twee processen $e^+e^- \to Z \to q\bar{q}$ en $e^+e^- \to W^+W^-$, waarbij tenminste één W boson vervalt in een quark-antiquark paar.

Het Bose-Einstein (BE) effect in een systeem van identieke bosonen is een direct gevolg van de symmetrisatie van de golffunctie van dit systeem. Dit kwantummechanische effect wordt experimenteel geobserveerd als een relatieve toename van de productie van identieke bosonen met kleine verschillen in de vier-impuls, $Q$, ten opzichte van de productie die er zou zijn in een wereld zonder BEC. In dit proefschrift zijn er drie motivaties om BEC te analyseren.

- De eerste interesse om BEC te bestuderen ligt in het feit dat ze informatie geven over de structuur van de bron waar de hadronen gevormd worden. Of, om een citaat te gebruiken uit [113]: "Twee-deeltjes correlaties geven de enige bekende manier om, via de gemeten impulsen van deeltjes, direct informatie te ontlenen over de ruimte-tijd structuur van de bron waar deze deeltjes zijn gevormd". In hoofdstuk 3 van dit proefschrift is de vorm en de grootte van de twee-deeltjes BE correlatiefunctie gemeten in drie dimensies. Op deze manier kan informatie verkregen worden over de structuur van de bron in drie dimensies.

- De laatste jaren is de belangstelling voor BEC in de LEP gemeenschap gegroeid. Dit vanwege het feit dat deze correlaties de meting van de W massa, een van de belangrijkste doelstellingen van de tweede fase van LEP (LEP2), kunnen beïnvloeden. Bij de productie van twee W bosonen, die beide hadronisch vervallen, met andere woorden, bij het proces $e^+e^- \to W^+W^- \to q_1\bar{q}_2q_3\bar{q}_4$, kunnen BEC verwacht worden tussen bosonen die van verschillende W's afkomen. Indien deze inter-W BEC worden waargenomen, zal dit de meting van de W massa beïnvloeden. Dit komt omdat de waarnemer dan niet meer eenduidig kan zeggen van welke W een zeker boson in de eindtoestand afkomstig is. In hoofdstuk 4 van dit proefschrift is een analyse gedaan om het bestaan van inter-W BEC te onderzoeken. De analyse is hier gedaan in één dimensie omdat de statistiek voor een multi-dimensionele analyse te beperkt is.

- In zowel hoofdstuk 3 als 4 is gekeken naar twee-deeltjes correlaties. Echter, extra informatie die niet aanwezig is in twee-deeltjes correlaties, kan ontleend worden uit

> hogere-orde BEC. Hogere-orde correlaties zijn gevoelig voor details van verschillende dynamische correlaties en kunnen derhalve dienen om onderscheid te maken tussen modellen voor multi-boson productie. Zo zijn hogere-orde correlaties gevoelig voor asymmetrieën in de bron en geven ze een manier om de mate van coherentie van het boson productiemechanisme te bepalen. In hoofdstuk 5 van dit proefschrift zijn drie-deeltjes BEC bestudeerd met als doel te onderzoeken of er aanwijzingen zijn voor een coherent productiemechanisme.

De $e^+e^-$ processen, relevant voor de bovenstaande studies, zijn verzameld met de L3 detector, die gebouwd is rondom één van de $e^+e^-$ interactiepunten. De geladen deeltjes die gebruikt worden voor de diverse analyses zijn gereconstrueerd in een dradenkamer en in een silicium vertexdetector. De geanalyseerde meetgegevens hebben de volgende voornaamste resultaten opgeleverd.

Uit ongeveer 1 miljoen $e^+e^- \to Z \to q\bar{q}$ processen, geselecteerd uit de meetgegevens van 1994, bij $\sqrt{s} \simeq 91.2\,\text{GeV}$, is een drie-dimensionale BE correlatiefunctie bepaald. Dit is gedaan in het longitudinale massa middelpuntsysteem, waar ieder paar van deeltjes een Lorentz boost ondergaat, zodanig dat de som van de twee impulsen in de richting van de thrust-as – die de richting van de oorspronkelijke quarks benaderd – nul is. De richting langs de thrust-as is gedefinieerd als de longitudinale richting en twee richtingen daar loodrecht op worden de out- en side-richting genoemd. Zowel de longitudinale- als de side-richting geven, in de Fourier getransformeerde ruimte, een geometrische maat voor de bron. De out-richting levert een meting die een menging is van een tijd- en ruimtecomponent. Wat eigenlijk gemeten wordt met de BE correlatiefunctie, is een zogenaamde homogeniteitszone, met andere woorden, het gebied waar BE interferentie plaatsvindt. De verhouding tussen de breedtes van de BE correlatiefunctie in de side- en longitudinale-richting van dit gebied is gemeten en het resultaat is $R_{\text{side}}/R_{\text{L}} = 0.81 \pm 0.02^{+0.03}_{-0.19}$, waar de eerste fout statistisch is en de tweede fout systematisch. De systematische fout wordt gedomineerd door de afhankelijkheid van Monte Carlo modellen om de data te corrigeren voor detector effecten, zoals acceptantie, resolutie en misidentificatie van deeltjes. Het resultaat laat zien dat de bron uitgerekt is in de richting van de thrust-as. Dit resultaat wordt niet gereproduceerd door de huidige beschikbare Monte Carlo modellen omdat daar wordt uitgegaan van een sferisch symmetrische bron. Ook wordt in dergelijke modellen ervan uitgegaan dat de homogeniteitszone van de bron Gaussisch verdeeld is, terwijl de metingen uitwijzen dat de BE correlatiefunctie bij lage $Q$ sterker stijgt dan een Gaussische functie. Zowel de elongatie van de bron als het niet-Gaussische gedrag van de correlatiefunctie worden echter wel theoretisch verwacht in het Lund string model ten gevolge van een longitudinale uitrekking van het stringveld. De LEP experimenten DELPHI en OPAL hebben intussen ook de elongatie gemeten en hun resultaten zijn consistent met dit resultaat.

BEC zijn onderzocht in het proces $e^+e^- \to W^+W^-$. In het bijzonder is gekeken naar correlaties tussen deeltjes die van verschillende W's (in het zelfde proces) afkomen. De data die verkregen zijn in de jaren 1998, 1999 en 2000, bij $\sqrt{s} \simeq 189-209\,\text{GeV}$, wat correspondeerd met 89% van de L3 data verzameld bij LEP2, zijn geanalyseerd. In totaal zijn ongeveer 9000 $W^+W^-$ processen geselecteerd. In 58% van deze processen vervallen beide

W's hadronisch (volledig hadronisch kanaal). In de overige processen vervalt er één W hadronisch en de andere W vervalt in een lepton en het corresponderende (anti-)neutrino (semi-hadronisch kanaal). De moeilijkheid in de selectie is dat een significant percentage achtergrond processen geselecteerd wordt, van enkele procenten in het semi-hadronische kanaal tot ongeveer 20% in het volledig hadronische kanaal. Afgezien van de soort quark, wordt verwacht dat hadronisch W verval en hadronisch Z verval gelijk zijn. Omdat b quark productie sterk onderdrukt is in W verval, zijn in hadronisch Z verval de $b\bar{b}$ processen zoveel mogelijk verwijderd. De oorspronkelijke fractie $b\bar{b}$ gevallen is van 22% tot 3% gereduceerd. Het blijkt dat de resterende lichte-quark Z vervallen een BE correlatiefunctie geven die overeenkomt met de correlatiefunctie berekend uit de semi-hadronische WW processen, zoals verwacht. Verder is geobserveeerd dat de BEC in het volledig hadronische WW kanaal minder sterk zijn dan in het semi-hadronische kanaal. Dit is overeenkomstig met geen of weinig inter-W BEC. Een directe meting van inter-W BEC is gedaan door te bestuderen of de WW data afwijken van een relatie die per constructie alleen waar is indien geen inter-W correlaties bestaan. Het resultaat is dat er geen aanwijzingen gevonden zijn voor het bestaan van inter-W BEC. Dit resultaat komt van een meting waarbij de modelafhankelijkheid beperkt is. Dit komt omdat direct uit de data een verzameling processen geconstrueerd is, door verschillende semi-hadronische WW processen te mengen, die lijkt op een verzameling volledig hadronische WW events, maar met de eigenschap dat er geen inter-W correlaties aanwezig zijn. Een typische variabele die gevoelig is voor inter-W BEC is $\Lambda$. Het resultaat van de meting van $\Lambda$ is $0.008 \pm 0.018 \pm 0.016$, waar de eerste fout statistisch is en de tweede fout systematisch. Dit resultaat is consistent met geen inter-W BEC. Een Monte Carlo model met inter-W BEC geeft $\Lambda = 0.126 \pm 0.008$. De data wijken 4.7 standaard deviaties af van dit model. In de statistische fout zijn bin-bin correlaties in de $Q$ variabele, die veroorzaakt worden door multipliciteitsschommelingen in de WW processen, meegenomen. Het resultaat van de studie aan inter-W BEC heeft als belangrijkste consequentie dat de onzekerheid op de meting van de W massa ten gevolge van inter-W BEC klein is. Vóór deze analyse waren onzekerheden geschat van 60 tot 100 MeV. Voorlopig is de onzekerheid bepaald op 20 MeV. Gepubliceerde resultaten van ALEPH en voorlopige resultaten van DELPHI zijn ook consistent met geen inter-W BEC. Voorlopige resultaten van OPAL zijn niet afdoende door een gebrek aan statistiek. Huidige studies en combinatie van resultaten van de verschillende LEP experimenten kunnen, derhalve, de onzekerheid tot onder de 10 MeV brengen (indien waarnemingen van inter-W BEC uitblijven).

Naast twee-deeltjes BEC, zijn ook drie-deeltjes BEC bestudeerd in hadronisch vervallende Z bosonen, geselecteerd uit de meetgegevens van 1994. De kinematische variabele die gebruikt is, is $Q_3 \equiv (Q_{12}^2 + Q_{13}^2 + Q_{23}^2)^{1/2}$, waar $Q_{ij}$ $(i, j = 1, 2, 3)$ het vier-momentum verschil is tussen deeltjes $i$ en $j$. In de drie-deeltjes BE correlatiefunctie is een groot deel van de correlaties afkomstig van twee-deeltjes correlaties. Deze zijn er uit gefilterd en het restant laat zien dat pure drie-deeltjes BEC bestaan. Een formalisme dat een relatie geeft tussen twee- en drie-deeltjes BEC, in het geval er wordt uitgegaan van een incoherent productiemechanisme van bosonen, is getest. In deze relatie is een fase $\phi$ gedefinieerd die afwijkt van nul indien het mechanisme (gedeeltelijk) coherent van aard is. De data laten zien dat $\phi$ consistent met nul is, hetgeen overeenkomstig is met een incoherent productiemechanisme. De onzekerheid op deze meting is voornamelijk afkomstig van de Monte Carlo modelafhankelijkheid waarmee de data gecorrigeerd worden voor allerlei detector effecten. De modelafhankelijkheid is enigszins gereduceerd door een speciale selectie te maken op de impulsen van de deeltjes en de openingshoek tussen de deeltjes. Echter, een gedeeltelijk coherent productiemechanisme kan niet worden uitgesloten. De LEP experimenten DELPHI en OPAL hebben ook pure drie-deeltjes correlaties gemeten. Ze hebben $\phi$ echter niet gemeten.

# Bibliography

[1] K. Gottfried and V.F. Weisskopf, "Concepts of Particle Physics", Clarendon Press, Oxford (1984).

[2] R. Hanbury Brown and R.Q. Twiss, Phil. Mag. **45** (1954) 663; Nature **177** (1956) 27 and **178** (1956) 1046.

[3] G. Goldhaber, W.B. Fowler, S. Goldhaber, T.F. Hoang, Phys. Rev. Lett. **3** (1959) 181.

[4] G. Goldhaber, S. Goldhaber, W. Lee and A. Pais, Phys. Rev. **120** (1960) 300.

[5] DELPHI Collab., P. Abreu et al., Phys. Lett. **B 286** (1992) 201; Z. Phys. **C 63** (1994) 17.

[6] ALEPH Collab., D. Decamp et al., Z. Phys. **C 54** (1992) 75.

[7] OPAL Collab., G. Alexander et al., Z. Phys. **C 72** (1996) 389.

[8] G.I. Kopylov and M.I. Podgoretskii, Sov. J. Nucl. Phys. **15** (1972) 219; Sov. J. Nucl. Phys. **18** (1974) 336; G.I. Kopylov, Phys. Lett. **50B** (1974) 572.

[9] M. Gyulassy, S. Kaufmann and L. Wilson, Phys. Rev. **C 20** (1979) 2267.

[10] S. Pratt, T. Csörgő and J. Zimányi, Phys. Rev. **C 42** (1990) 2646.

[11] S. Chapman and U. Heinz, Phys. Lett. **B 340** (1994) 250.

[12] S. Chapman, P. Scotto and U. Heinz, Heavy Ion Physics **1** (1995) 1.

[13] D.H. Boal, C.K. Gelbke, B.K. Jennings, Rev. Mod. Phys. **62** (1990) 553.

[14] S. Pratt, Phys. Lett. **B 301** (1993) 159.

[15] W.Q. Chao, C.S. Gao and Q.H. Zhang, J. Phys. **G 21** (1995) 847.

[16] T. Csörgő and J. Zimányi, Phys. Rev. Lett. **80** (1998) 916.

[17] U. Heinz, P. Scotto and Q.H. Zhang, Ann. Phys. bf 288 (2001) 325.

[18] J. Gunion, Phys. Rev. Lett. **37** (1976) 402.

[19] J. Schwinger, Phys. Rev. **128** (1962) 2425; A. Casher, J. Kogut and L. Susskind, Phys. Rev. **D 10** (1974) 732.

[20] M. Deutschmann et al., Nucl. Phys. **B 204** (1982) 333.

[21] S. Nickerson, T. Csörgő and D. Kiang, Phys. Rev. **C 57** (1998) 3251.

[22] Q.H. Zhang, W.Q. Chao and C.S. Gao, Phys. Rev. **C 52** (1995) 2064.

[23] L. Lönnblad and T. Sjöstrand, Phys. Lett. **B 351** (1995) 293.

[24] S.V. Chekanov, E.A. De Wolf and W. Kittel, Eur. Phys. J. **C 6** (1999) 403.

[25] A. Ballestrero et al., in "Physics at LEP2", eds. G. Altarelli, T. Sjöstrand and P. Zwirner, CERN 96-01 (1996) 141.

[26] V. Kartvelishvili, R. Kvatadze and R. Møller, Phys. Lett. **B 408** (1997) 331.

[27] S. Jadach and K. Zalewski, Acta Phys. Pol. **B 28** (1997) 1363.

[28] K. Fialkowski and R. Wit, Acta Phys. Pol. **B 28** (1997) 2039.

[29] K. Fialkowski, R. Wit and J. Wosiek, Phys. Rev. **D 58** (1998) 094013.

[30] Š. Todorova-Nová, Ph.D. thesis, Strasbourg, IReS 98-18 (1998).

[31] L. Lönnblad and T. Sjöstrand, Eur. Phys. J. **C 2** (1998) 165.

[32] M. Biyajima et al., Progr. Theor. Phys. **84** (1990) 931.

[33] H. Heiselberg and A.P. Vischer, NBI-97-32, July 1997.

[34] E.A. De Wolf, I.M. Dremin and W. Kittel, Phys. Reports **270** (1996) 1.

[35] V.L. Lyuboshitz, Sov. J. Nucl. Phys. **53** (1991) 514.

[36] U. Heinz and Q. Zhang, Phys. Rev. **C 56** (1997) 426.

[37] T. Sjöstrand, Comp. Phys. Comm. **82** (1994), 74.

[38] B. Andersson and M. Ringnér, Phys. Lett. **B 421** (1998) 283; Nucl. Phys. **B 513** (1998) 627.

[39] B. Andersson and W. Hofmann, Phys. Lett. **B 164** (1986) 364.

[40] G. Marchesini and B.R. Webber, Nucl. Phys. **B 310** (1988) 461; G. Marchesini et al., Comp. Phys. Comm. **67** (1992) 465.

[41] R. Smits, Tuning of BE Parameters in New BE Algorithms for Z-decay, Master's Thesis, HEN-433, 2000.

[42] K. Fialkowski and R. Wit, Z. Phys. **C 74** (1997) 145.

[43] LEP design report volume I, CERN-LEP/TH/83-29 (1983); LEP design report volume II, CERN-LEP 84-01 (1984); LEP design report volume III, CERN-AC 96-01.

[44] L3 Collab., B. Adeva et al., Nucl. Inst. Meth. **A 289** (1990) 35.

[45] L3 Collab., B. Adeva et al., Nucl. Inst. Meth. **A 289** (1990) 35; J.A. Bakken et al., Nucl. Inst. Meth. **A 275** (1989) 81; O. Adriani et al., Nucl. Inst. Meth. **A 302** (1991) 53; O. Adriani et al., Phys. Reports **236** (1993) 1; B. Adeva et al., Nucl. Inst. Meth. **A 323** (1992) 109; K. Deiters et al., Nucl. Inst. Meth. **A 323** (1992) 162; M. Chemarin et al., Nucl. Inst. Meth. **A 349** (1994) 345; B. Acciarri et al., Nucl. Inst. Meth. **A 351** (1994) 300; I.C. Brock et al., Nucl. Inst. Meth. **A 381** (1996) 23; A. Adam et al., Nucl. Inst. Meth. **A 383** (1996) 342; G. Basti et al., Nucl. Inst. Meth. **A 374** (1996) 293.

[46] W. Blum and L. Rolandi, "Particle Detection with Drift Chambers", Springer Verlag, Berlin, Heidelberg (1993).

[47] A.P. Colijn, Ph.D. Thesis, University of Amsterdam (1999).

[48] A.V. Aho, J.E. Hopcroft and J.D. Ullman, The Design and Analysis of Computer Algorithms, Addison-Wesley (1974).

[49] L3 Collab., B. Adeva et al., Z. Phys. **C 55** (1992) 39.

[50] R. Brun et al., CERN/DD/EE/84-1 (Revised 1987).

[51] L3 Collab., M. Acciarri et al., Phys. Lett. **B 458** (1999) 517.

[52] Opal Collab., G. Abbiendi et al., Eur. Phys. J. **C 16** (2000) 423.

[53] Delphi Collab., P. Abreu et al., Phys. Lett. **B 471** (2000) 460.

[54] T. Csörgő and B. Lörstad, Proc. XXVth Int. Symp. on Multiparticle Dynamics, eds. D. Bruncko et al. (World Scientific, Singapore, 1997) p. 66.

[55] G. Bertsch, M. Gong and M. Tohyama, Phys. Rev. **C 37** (1988) 1896.

[56] T. Csörgő and S. Pratt, Proc. Workshop on Relativistic Heavy-Ion Physics, eds. Csörgő et al. (KFKI-1991-28/A, Budapest, 1991) p. 75.

[57] U. Heinz et al., Phys. Lett. **B 382** (1996) 181.

[58] F. Yano and S. Koonin, Phys. Lett. **B 78** (1978) 556; M. Podgoretskii, Sov. J. Nucl. Phys. **37** (1983) 272.

[59] K. Geiger et al., Bose-Einstein correlations in a phase-space approach to $e^+e^-$ annihilation into hadrons, CERN-TH/98-345.

[60] Š. Todorova-Nová, J. Rameš, Simulation of Bose-Einstein effect using space-time aspects of Lund string fragmentation model, Strasbourg preprint IReS97-29.

[61] The L3 detector simulation is based on GEANT3, see R. Brun et al., CERN report CERN DD/EE/84-1 (revised) 1987, and uses GHEISHA to simulate hadronic interactions, see H. Fesefeldt, RWTH Aachen report PITHA 85/02, 1985.

[62] Sergei Chekanov, Ph.D. Thesis, University of Nijmegen (1997).

[63] E.O. Alt et al., Eur. Phys. J. **C 13** (2000) 663.

[64] S. Chapman, P. Scotto and U. Heinz, Phys. Rev. Lett. **74** (1995) 4400; Heavy Ion Physics **1** (1995) 1; S. Chapman, J.R. Nix and U. Heinz, Phys. Rev. **C 52** (1995) 2694.

[65] T. Csörgő and S. Hegyi, Phys. Lett. **B 489** (2000) 15.

[66] F.Y. Edgeworth, Trans. Cambridge Phil. Soc. **20** (1905) 36. See also, e.g., Harald Cramér, Mathematical Methods of Statistics (Princeton Univ. Press, 1946).

[67] R. Mureşan, O. Smirnova and B. Lörstad, Eur. Phys. J. **C 6** (1999) 629.

[68] K. Geiger et al., Bose-Einstein correlations in a phase-space approach to $e^+e^-$ annihilation into hadrons, CERN-TH/98-345.

[69] K. Fialkowski and R. Wit, Acta Phys. Pol. **B 32** (2001), 1233.

[70] L3 Collab., M. Acciarri et al., Phys. Lett. **B 493** (2000), 233.

[71] J.A. van Dalen, W. Kittel, W. Metzger, Bose-Einstein Correlations in $e^+e^- \to W^+W^-$ Events: an Update Including the Data of 1999, L3 note 2615, 2000.

[72] J.A. van Dalen, W. Kittel, W. Metzger, Bose-Einstein Correlations in $e^+e^- \to W^+W^-$ Events at $\sqrt{s} = 189 - 209\,\mathrm{GeV}$, L3 note 2674, 2001.

[73] G. Gustafson, U. Pettersson and P. Zerwas, Phys. Lett. **B 209** (1988) 90; T. Sjöstrand and V.A. Khoze, Phys. Rev. Lett. **72** (1994) 28.

[74] T. Sjöstrand and V.A. Khoze, Z. Phys. **C 62** (1994) 281.

[75] G. Gustafson and J. Häkkinen, Z. Phys. **C 64** (1994) 659.

[76] L. Lönnblad, Z. Phys. **C 70** (1996), 107; C. Friberg, G. Gustafson and J. Häkkinen, Nucl. Phys. **B 490** (1997) 289; B.R. Webber, J. Phys. **G 24** (1998) 287.

[77] V.A. Khoze and T. Sjöstrand, Eur. Phys. J. **C 6** (1999) 271.

[78] The LEP collaborations ALEPH, DELPHI, L3, OPAL, and the LEP W Working Group, Combined Preliminary Results on the Mass and Width of the W Boson Measured by the LEP Experiments, LEPEWWG/MASS/2001-02, ALEPH 2001-044 PHYSICS 2001-017, DELPHI 2001-122 PHYS 899, L3 Note 2695, OPAL TN-697, 2001.

[79] P.W. Higgs, Phys. Lett. **12** (1964) 132; F. Englert and R. Brout, Phys. Lett. **13** (1964) 321; G.S. Guralnik et al., Phys. Lett. **13** (1964) 585.

[80] L3 Collab., M. Acciarri et al., Phys. Lett. **B 496** (2000) 19.

[81] L3 Collab., P. de Jong, Preliminary Results on the Measurement of W-Pair Cross Sections in $e^+e^-$ Interactions at $\sqrt{s} = 192 - 202\,\mathrm{GeV}$ and W-Decay Branching Fractions, L3 note 2514, 2000.

[82] L3 Collab., Preliminary Results on the Measurement of W-Pair Cross Sections in $e^+e^-$ Interactions at $\sqrt{s} = 205 - 208\,\mathrm{GeV}$ and W-Decay Branching Fractions, L3 note 2638, 2001.

[83] Yu. L. Dokshitzer, J. Phys. **G 17** (1991) 1537.

[84] H. Georgi and M. Machacek, Phys. Rev. Lett. **39** (1977) 1237; Z. Kunszt et al., Z Physics at LEP1, report CERN 89-08 (1989), eds. G. Altarelli, R. Kleiss, C. Verzegnassi, Vol. 1, p. 385.

[85] KORALW version 1.33 is used: M. Skrzypek et al., Comp. Phys. Comm. **94** (1996) 216; M. Skrzypek et al., Phys. Lett. **B 372** (1996) 289.

[86] L3 Collab., M. Acciarri et al., Phys. Lett. **B 411** (1997) 373: A. Dominguez, Ph.D. Thesis, University of California at San Diego (1998), http://hep.ucsd.edu/thesis/aaron.html.

[87] F. Filthaut, D. Bourilkov and V. Briglevic, Comparison 1995 L3 vertex data with LEP BOM and QS0 measurements, L3 note 1943, 1996.

[88] J. Sens and P. Vikas, Reconstruction of the L3 fill vertices, L3 note 1027, 1991.

[89] Mirna van Hoek, Ph.D. Thesis, University of Nijmegen (1999).

[90] G. Hanson et al., Phys. Rev. Lett. **35** (1975) 1609.

[91] ALEPH Collab., R. Barate et al., Phys. Lett. **B 478** (2000) 50.

[92] ALEPH Collab., R. Barate et al., Further Studies on Bose-Einstein correlations in W-pair decays, ALEPH-2000-039 CONF 2000-059 (2000).

[93] ALEPH Collab., R. Barate et al., Further studies on Bose-Einstein correlations in W-pair decays, ALEPH-2001-064 CONF 2001-044 (2001).

[94] OPAL Collab., G. Abbiendi et al., Bose-Einstein Correlations in $e^+e^- \rightarrow W^+W^-$ Events at 172, 183 and 189 GeV, Opal Physics Note PN393 (1999).

[95] DELPHI Collab., Š. Todorova-Nová et al., Particle correlations in $e^+e^- \rightarrow W^+W^-$ events with the DELPHI detector, 2001-107 CONF 534 (2001).

[96] L3 Collab., M. Acciarri et al., Phys. Lett. **B 454** (1999) 386.

[97] L3 Collab., M. Acciarri et al., Preliminary Results on the Measurement of Mass and Width of the W Boson at LEP, L3 note 2575, 2000.

[98] L3 Collab., M. Acciarri et al., Preliminary Results on the Measurement of Mass and Width of the W Boson at LEP, L3 note 2637, 2001.

[99] P. de Jong, Fragmentation Studies for W Mass and Width with a Fast Detector Simulation, L3 note 2628, 2000.

[100] B. Andersson, Proc. of XXXth Int. Symp. on Multiparticle Dynamics, eds. T. Csörgő et al. (World Scientific, Singapore, 2001) p. 364. e-print: hep-ph/0101222.

[101] T. Csörgő, Particle Interferometry from 40 MeV to 40 TeV (KFKI-1999-10/A, Budapest, 1999). Proc. Int. Summer School on Particle Production Spanning MeV and TeV Energies, eds. W. Kittel et al. (Kluwer Academic Publishers, Dordrecht, 2000) p. 203. e-print: hep-ph/0001233.

[102] R. Hanbury Brown et al., Mon. Not. R. Astron. Soc. **167** (1974) 121.

[103] NA22 Collab., N.M. Agababyan et al., Phys. Lett. **B 422** (1998) 359; R. Hakobyan, Proc. of XXXth Int. Symp. on Multiparticle Dynamics, eds. T. Csörgő et al. (World Scientific, Singapore, 2001) p. 331.

[104] T. Csörgő, B. Lörstad, J. Schmid-Sørensen and A. Ster, Eur. Phys. J. **C 9** (1999) 275.

[105] NA22 Collab., N.M. Agababyan et al., Z. Phys. **C 68** (1995) 229.

[106] T. Csörgő, Proc. Torino Workshop on Multiparticle Production, eds. A. Giovannini and R. Ugoccioni, Nucl. Phys. **B 92** (Proc. Suppl.) (2001) 223.

[107] Delphi Collab., P. Abreu et al., Phys. Lett. **B 355** (1995) 415.

[108] Opal Collab, K. Ackerstaff et al., Eur. Phys. J. **C 5** (1998) 239.

[109] NA44 Collab., H. Bøggild et al., Phys. Lett. **B 455** (1999) 77.

[110] NA44 Collab., I.G. Bearden et al., e-print nucl-ex/0102013, to be published in Phys. Lett. **B**.

[111] WA98 Collab., M.M. Aggarwal et al., Phys. Rev. Lett. **85** (2000) 2895.

[112] F. del Moral and C. Pajares, Proc. Torino Workshop on Multiparticle Production, eds. A. Giovannini and R. Ugoccioni, Nucl. Phys. **B 92** (Proc. Suppl.) (2001) 95.

[113] U.A. Wiedemann and U. Heinz, Phys. Rep. **319** (1999) 145.

# Curriculum Vitae

Op 14 mei 1974 werd ik geboren te Herwen en Aerdt. Na in 1993 mijn VWO diploma te hebben gehaald aan het Liemers College te Zevenaar, ging ik natuurkunde studeren aan de Katholieke Universiteit Nijmegen (KUN). In december 1997 legde ik cum laude het doctoraalexamen af in de natuurkunde. Het afstudeeronderzoek in de vakgroep theoretische hoge energie fysica, onder leiding van Prof. Dr. R.H.P. Kleiss, resulteerde in een scriptie getiteld: "Bremsstrahlung Corrections to Polarized Compton Scattering". Gedurende mijn studie was ik ook werkzaam als werkcollege-assistent bij diverse natuurkunde vakken.

In januari 1998 begon ik als onderzoeker in opleiding te werken aan de KUN, in dienst van de Stichting voor Fundamenteel Onderzoek der Materie (FOM). Onder leiding van Prof. Dr. E.W. Kittel heb ik vier jaar gewerkt aan mijn promotieonderzoek op de afdeling experimentele hoge energie fysica. In het kader van dit onderzoek heb ik door regelmatige bezoeken aan het CERN (Genève), alwaar het experiment waar ik onderzoek aan verrichtte (L3) zich bevond, intensief contact gehad met medewerkers aldaar. Een deel van mijn onderzoek is gedaan in samenwerking met de "L3 quantum chromodynamics (QCD) analysis group" en een deel met de "L3 W physics analysis group". Mijn onderzoek heeft tot op heden geleid tot twee publicaties in het tijdschrift "Physics Letters B" en drie zijn er in voorbereiding. Verder zijn er verschillende interne artikelen en bijdragen aan conferentie- en workshoprapporten verschenen.

Tijdens mijn promotieonderzoek bezocht ik tweemaal de "Joint Belgium-Dutch-German Graduate School of Particle Physics", de "NATO Advanced Study Institute on Particle Production Spanning MeV and TeV Energies" en zeven maal de "Topical Lectures" van de onderzoeksschool voor subatomaire fysica. Daarnaast heb ik namens de L3 collaboratie resultaten gepresenteerd op een drietal conferenties en diverse workshops: twee workshops uit de serie "Correlations and Fluctuations" in Mátraháza (Hongarije) en in Turijn (Italië), twee L3 workshops in Lyon (Frankrijk) en in Balatonfüred (Hongarije), de "QCD99" conferentie in Montpellier (Frankrijk), "Les Rencontres de Moriond" in Les Arcs (Frankrijk), de "LEPWW" workshop in Sesimbra (Portugal) en het "International Symposium on Multi-Particle Dynamics" in Datong (China). Verder ben ik vier semesters als werkcollege-assistent werkzaam geweest bij de vakken structuur der materie, kwantummechanica I en kernfysica.

# Acknowledgements

This thesis would not have been possible without the help, guidance, stimulation and support offered by many people in the last four years. Without being able to do justice to them all, I would like to mention the following people explicitly, here.

In the first place, I thank Prof. Dr. Wolfram Kittel for his flexibility and stimulating discussions and his guidance through the labyrinths of correlations and fluctuations in multi-particle dynamics. His critical remarks greatly improved this thesis. Furthermore, I thank Dr. Wesley Metzger for his help and guidance in the data analyses. The manuscript-committee as well as the members of the L3 QCD analysis group and the L3 W analysis group I want to thank for their critical look and their help with respect to the preparations of this thesis and the publications of my results. I also thank various theoreticians and colleagues at CERN for their useful discussions, suggestions and their explanations on the theoretical background in the field of correlations. In particular, I want to mention Prof. Eddi De Wolf, Prof. Bo Andersson, Prof. Tamás Csörgő, Šharka Todorova-Nová, Arno Straessner, Luca Malgeri, Raja Nandakumar, Martin Grunewald, Dominique Duchesneau, John Field, Paul de Jong, Nick van Remortel, Oliver Pooth, Thomas Kress and Bolek Pietrzyk. The students, staff and the secretariat of the department of experimental high energy physics at the KUN, as well as the Chinese colleagues who visited our department, I want to thank for their interest, encouragement and help.

Outside the circle of physicists, my special thanks go to my parents, my sister Jolanda and my beloved Nicole for all their support, patience and their unconditional belief in what I was doing all those years. Without them, this thesis would not exist.